Assembles of Organic Molecules on Insulating Surfaces Investigated by nc-AFM

Inauguraldissertation

zur
Erlangung der Würde eines Doktors der Philosophie
vorgelegt der
Philosophisch-Naturwissenschaftlichen Fakultät
der Universität Basel

von

Lars A. Zimmerli
aus Oftringen AG

UNI
BASEL

Basel, 2007

Genehmigt von der Philosophisch-Naturwissenschaftlichen Fakultät
auf Antrag von
Prof. Dr. E. Meyer
Prof. Dr. H.-J. Güntherodt

Basel, den 11. Dezember 2007

Prof. Dr. Hans-Peter Hauri
Dekan

Abstract

The formation of ordered one- and two-dimensional molecular structures on insulating surfaces has been investigated by means of a room temperature scanning force microscope (SFM). In particular, one dimensional row structures along step edges of alkali halide crystals were obtained as well as two dimensional chain structures on the terraces.

Various molecules have been deposited on different substrates. While most of the combinations didn't show any ordered structures at all, some combinations led to ordered growth.

Porphyrin based molecules have proven to be promising candidates to form self-assembled structures on insulating surfaces. Their close affinity to hemoglobine and chlorophyll makes them also interesting as functional building parts. Porphyrin molecules tend to $\pi - \pi$ stack in crystals, allowing them to work as optical or electrical antennae. While the adsorption on metallic surfaces showed that this particular stacking was prevented by the flat alignment on the substrate, molecules were adsorbed standing upright on alkali-halide(100) surfaces maintaining the intermolecular $\pi - \pi$-stacking.

Alkali-halide surfaces have been structured in different ways to study the molecular arrangements under various conditions. Micrometer long, one dimensional wires along step edges have been observed as well as large two-dimensional assemblies of parallel running wire structures across flat terraces. The orientation of those chains is guided by the underlying substrate and the equilibrium distance between the molecules.

In order to check the feasibilty to contact the wires, experiments on gold cluster decorated insulating surfaces have been performed. Under certain premises of the cluster arrangement it proved to be successful to grow molecular wires between two gold clusters.

At last, molecular assemblies on ultrathin salt films on Cu(111) were studied by means of Kelvin Probe Force Microscopy (KPFM) to obtain details about possible exciton or electron transport in the $\pi - \pi$ stacks. The KPFM did not yet show conclusive results, but the dynamic compensation of the contact potential difference allowed ultrahigh resolution images, which revealed differences in the adsorption structures on layers of different heights.

In summary, the adsorption of cyanoporphyrin molecules on various insulation surfaces has been studied and carefully analyzed.

Contents

List of Abbreviations

Abbreviation	Description	First Appearance
AES	Auger Electron Spectroscopy	page 17
AM-mode	Amplitude Modulation Mode	page 6
AFM	Atomic Force Microscope	page 3
CPD	Contact Potential Difference	page 11
Cu	Copper	page 56
DFM	Dynamic Force Microscopy	page 5
Fe	Iron	page 30
FM-mode	Frequency Modulation Mode	page 6
FFT	Fast Fourier Transformation	page 21
HOMO	Highest Occupied Molecular Orbital	page 56
HOPG	Highly Orientend Pyrolytic Graphite	page 3
KBr	Potassium Bromide	page 17
KPFM	Kelvin Probe Force Microscopy	page 13
LEED	Low Energy Electron Diffraction	page 17
LUMO	Lowest Unoccupied Molecular Orbital	page 56
Mg	Manganese	page 30
ML	Monolayer	page 39
NaCl	Sodium Chloride	page 17
nc-AFM	Non-contact Atomic Force Microscope	page 5
PLL	Phase Locked Loop	page 14
Si	Silicon	page 3
SFM	Scanning Force Microscope	page iii
STM	Scanning Tunneling Microscope	page 3
UHV	Ultra High Vacuum	page 3
VdW	Van der Waals	page 7
XPS	X-ray Photoelectron Scattering	page 17
Zn	Zinc	page 30

Motivation and Outline

When looking at the progress semi-conductor industries made the past decades and the pace technology is approaching the limits of miniaturization [1], new ways in electronics have to be found. Molecular electronic is currently a field of immense interest and research groups all over the world are working in this field. The thought of creating a molecular system performing operations has been the dream of mankind for several decades, as for instance already R. Feynman mentioned it in his famous lecture 'There is plenty of room at the bottom' [2].

The research field dealing with molecular assemblies, properties and new materials is called *nanotechnology*, since the structural length scales of such systems are in the range of $0.1 - 100\ nm$. A requirement for applications in nanotechnology is the possibility to build large arrays of nanostructured materials with sub-nanometer positioning accuracy of the individual functional units. Only this allows reaching the same scalability known from the classical semiconductor microelectronics [3]. The most promising approach is to use self-assembly [4] or even self organization [5]. This so called bottom-up approach is fundamentally different from established top-down methods such as in lithography used for device fabrication until now. Bottom-up approaches aim to build up structures by choosing appropriate individual elements which should build up the new material, while top-down approaches rely on an externally imposed structure. By choosing the right environmental conditions such as temperature, deposition rates, deposition amounts and designing appropriate linker and spacer groups on the substituents finally leads to the desired structures. Furthermore, bottom-up approaches do not require the most often time consuming step of actively building the structure. A key point in potential mono molecular electronic devices is to assure an electrically decoupling from the surface [6]. One way to achieve this is the usage of insulating surfaces as substrates which on the other hand requires the use of force microscopy techniques. With this idea in mind, the goal of this work was the study of molecular assemblies on insulating surfaces.

Insulating surfaces provide a very low diffusion barrier, allowing most of the molecules to diffuse freely over surface terraces thus forming unordered agglomerates at the step edges and impurities. The first part of this study therefore was dedicated to find appropriate surface treatments and molecules which form ordered structures. A second task then was to find possible ways to imply contacting of the structures.

Chapter 1 and chapter 2 of this research give an introduction on the instrumentation used for the study. The results on bulk insulators are presented in chapter 3. Chapter 4 then deals with experiments on molecular assemblies on ultrathin salt films.

1

Introduction to Scanning Probe Microscopy

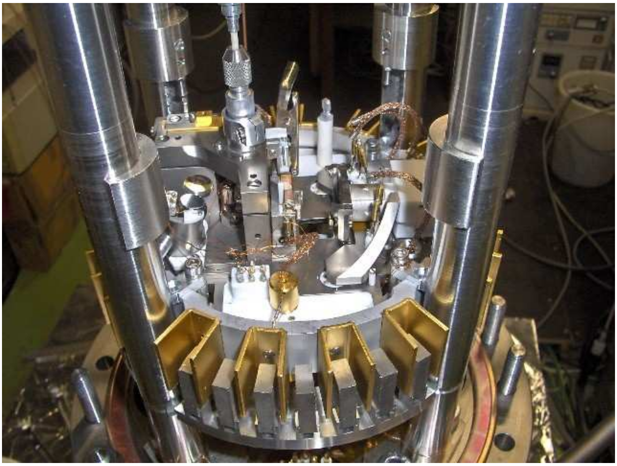

This chapter describes the historical development of the Scanning Force Microscopy, gives a short overview of the theoretical background and introduces the different imaging modes.

1.1 Historical Introduction

The development of the Scanning Force Microscope (SFM)[*], was initiated in 1982 when Binnig and Rohrer invented the Scanning Tunneling

---

[*] In the following referred to as AFM, Atomic Force Microscope

Microscope (STM) [7]. With this device it was possible for the first time to observe single atoms on a flat metallic surface in direct space. Only one year later Binnig *et al.* [8] managed to resolve the atomic structure of the $Si(111)$ reconstruction. With this event the STM was widely accepted and during the following years many spectacular high resolution images of metallic and semi-conducting surfaces were published. Binnig and Rohrer were awarded for their pioneering invention with the Nobel Price in 1986.

Despite all euphoria there are also some restrictions of the STM technique. Since the measurement is dependent on a small tunneling current flowing between a metallic tip and a sample, the application was limited to electrically conductive species. Most of the conductors, except HOPG[†] and few others are not suitable to examine in ambient conditions since they change frequently in time due to adsorption and oxidation. Therefore, the measurements have to be taken in UHV[‡] conditions where the sample-surfaces can be cleaned and kept in a defined state for several hours.

It was also found that in tunneling distance atomic forces started to act [9, 10], which motivated Binnig to think about developing a microscope that uses those forces as detection signal. Together with Quate and Gerber, a functional prototype of a scanning force microscope was built and presented in 1986 [11]. In contrast to the STM, which requires coercively a conductive sample, the AFM allowed for the first time to image insulating samples.

The heart of the AFM is composed of a tip attached to a cantilever which gets slightly bent by the atomic forces appearing at small tip sample separation. In the beginning the bending of the cantilever was measured by a STM tip mounted above the lever. With this procedure the atomic peridocities of graphite were measured for the first time [12] in the so called *contact mode*. Because of the quite strong load forces caused by the capillarity effect, it was not possible for a long time to measure atomic defects. It took over five years until so called true atomic resolution[§] on inert structures was achieved [13, 14]. So the prediction that the AFM is capable of atomic resolution was finally confirmed.

Around one decade after the invention of the AFM the imaging of reactive surfaces with atomic resolution was finally achieved. By using the *dynamic mode*, developed in 1991 [15], Giessibl [16] succeeded in 1995 to resolve the $Si(111) - (7 \times 7)$ reconstruction. In the present work

---

[†] **H**ighly **O**riented **P**yrolytic **G**raphite

[‡] **U**ltra **H**igh **V**acuum

[§] 'True atomic resolution' describes the imaging of atomic structures without tip-sample convolution caused by multiple tips or contacts this so called *non-contact* mode is used by default.

1.2 The Scanning Tunneling Microscope (STM)

The principle of the STM is based on the overlap of wavefunctions. Electrons can tunnel from filled to empty states of a metallic tip and a sample. An applied voltage between those two enables the flow of an electrical tunneling current at small enough distances ($5 - 15$ Å).

In quantum mechanics the state of an electron is given by a wavefunction fulfilling the Schrödinger Equation. Assuming a piece-wise constant barrier the solution of this problem for the classically forbidden area looks as follows:

$$\Psi_z = \Psi_0 \exp^{-kz}, \tag{1.1}$$

with $k = \frac{\sqrt{2m(\Phi - E)}}{\hbar}$. Choosing the applied voltage V_{Bias} small enough compared to the work function Φ of the electron, results in a tunneling barrier of an almost rectangular shape with height Φ and width z. E can therefore be neglected and the tunneling current becomes

$$I_t \propto V_{Bias} \rho_s(E_F) e^{-2kz} \tag{1.2}$$

with $\rho_s(E_F)$ being the density of states at the Fermilevel E_F. Equation 1.2 is leading us to two things. First there is a non-zero probability for an electron to tunnel through the barrier and second this probability is exponentionally dependent of the distance z. Metals usually have work functions of $4 - 6$ eV and therefore the change of the distance by 1 Å affects the tunneling current by one order of magnitude.

Typically an electrochemically edged wire, made of platinum-iridium or tungsten is used as STM tip. As in all scanning probe microscopes the tip or the sample is attached to a xyz- scanner which is capable of performing reproducible positioning of the tip with subatomic accuracy. Those scanners are usually made of piezoelectric ceramics that deform when applying a voltage. Furthermore an excellent decoupling from the environment and a good damping is mandatory to operate such an instrument.

The STM can be operated in two different ways. In the so called *constant height mode* the distance controller can be switched off and the tip is scanned at a constant height across the sample. For this mode a very flat surface, a negligible drift rate and an almost perfect damping of the system in order to prevent the tip from crashing is mandatory. Since this method doesn't require a controller following the atomic corrugation the measurement velocity is only determined by the bandwidth of the current detector.

The more common mode is the so called *constant current mode* where the distance z is kept constant by means of a P-I-controller. The signal which is used to control this distance is the tunneling current.

1.3 The Scanning Force Microscope (SFM)

In contrast to the STM in SFM/AFM forces, instead of currents are detected. The force sensor is commonly a sharp tip attached to a filigran cantilever. The forces between tip and sample are measured through the bending they induce to the lever. Those measurement probes are nowadays mostly microfabricated and commercially available. More details about cantilevers will be described in chapter 2. Scanning force microscopes reach resolutions in the sub-nanometer regime and allow under certain circumstances even atomic resolution. They are able to image conductive and non-conductive samples and are sensitive to forces down to the piconewton regime.

Contact Mode

In the static mode *(contact mode)* the tip is brought into mechanical contact with the sample. Forces cause a bending of the cantilever which is used as feedback signal to keep those forces constant during the scan. The change of the z-signal (= the position of the tip) results in a topographical map of the surface.

This operation mode leads to different images of quasi atomic resolution [17, 18] that show atomic periodicity but no defects of the surface. This effect is caused by a multiple contact of the tip with the sample leading to an averaging effect. After some scan-time the tip apex becomes commensurate with the surface. On layered samples, such as HOPG, it can also pick up a flake from the sample which leads to the same effect. Such tips always show perfect atomic periodicities, but never a single defect. Recently [19], atomic defects on heterostructures using *contact mode* have been observed.

Dynamic Mode

Applying the *dynamic mode* (nc-AFM, DFM[¶]), the cantilever is excited perpendicular to the surface and then approached to the sample. The

---

[¶] DFM: **D**ynamic **F**orce **M**icroscopy amplitude and frequency response yields to a feedback including information about the force between tip and surface. Typically, cantilevers with spring constants from several 10 N/m up to several 100 N/m are used in dynamic mode. Those high values are desired to avoid the 'jump into contact' effect [10]. The minimum detectable force gradient [20, 21] is given by

$$\frac{\partial}{\partial z} F_{min} = \frac{1}{A_{osc}} \sqrt{\frac{2kk_bTB}{2\pi f_0 Q}}, \tag{1.3}$$

where B is the bandwitdh of the detector, f_0 the resonance frequency of the lever, A_{osc} its oscillation amplitude and k its spring constant. Q is the quality factor of the lever, k_b the Boltzmann constant and T the temperature. Hence sensitivity can be improved by going to higher Q-values or frequencies.

In UHV conditions, the Q-factor is in the range of several 10^5 and therefore much higher than in air, where the system is damped to Q-values of around 100. In DFM, there are the following main operation modes: In the amplitude modulation mode[‖] developed by Martin *et al.* [21] the cantiliver is driven at a constant frequency f_{exc} with a fixed driving amplitude A_{exc}. Usually, f_{exc} is chosen to be slightly higher than the resonance frequency f_0 of the cantilever. A change in the force gradient $\partial F/\partial z$ gives rise to a shift $\Delta f = f_0 - f_{exc}$ in the resonance, and a corresponding shift ΔA in the amplitude of the cantilever vibration. The signal in AM-mode is derived by measuring the change of the amplitude. Increasing the Q-value leads to a restriction in the bandwidth of the system. The system needs a certain amount of time to reach a new steady state after a change in the force. This response can be expressed by terms of a time constant $\tau = 2Q/f_0$, which limits the available bandwidth.

In the frequency modulation mode[**], developed by Albrecht *et al.* [15], the cantilever is driven at its resonance frequency ($f_{exc} = f_0$). The phase φ between driving amplitude and oscillation amplitude is kept constant at the optimum value and the excitation A_{exc} is controlled in a way to keep the oscillation amplitude A constant. Changes in the force gradient $\partial F/\partial z$ cause almost instantaneous changes in the oscillator frequency which are detected by a FM demodulator. This resulting frequency shift $\Delta f = f_{osc} - f_0$ is used as the feedback signal to control the distance. Since the Eigenfrequency reacts with the time constant of $\tau = \frac{1}{f_0}$ this method is much faster than the AM- detection and offers higher bandwidths. Additionally, this mode let to the first true atomic resolution [16] in UHV.

[‖] short: AM-mode

[**] short: FM-mode

1.3.1 Interaction Forces

The interacting forces between tip and sample are the base of every Scanning Force Microscope. The sum of all those forces bends the cantilever. The potential energy between probe and sample V_{ts} is causing a force perpendicular to the sample, given by $F_{ts} = -\partial V_{ts}/\partial z$. We also can define a spring constant $k_{ts} = -\partial F_{ts}/\partial z$ describing the interaction force gradient. Depending on the operation mode of the microscope, either F_{ts} or one of the derived variables is used as a feedback signal.

The forces between tip and sample can be divided into long (Van der Waals, electrostatic) and short (chemical) range forces.

Van der Waals forces

Van der Waals forces are dipole-dipole forces. They act between dipoles that arise from fluctuations and dipoles induced in their electric field. The vdW forces between two macroscopic bodies can be calculated by integration over the tip and the sample geometry while assuming that the forces are additive and non-retarded [22]. For a spheric tip with radius R and a plane with distance z the interaction force becomes

$$F_{vdW} = -\frac{HR}{6z^2} \tag{1.4}$$

with H being the Hamaker constant. However, the assumption of the additivity denies the occurance of reflection where the mutual polarisation of two atoms is influenced by the presence of third atoms. The Lifshits theory proclaims a more rigorous approach which treats the bodies as continuum. Nevertheless, the distance dependance has the same form as in equation 1.4. A more detailed analysis of this theory however is not the goal of this work. The vdW force can also be determined by assuming more complex tip geometries as for example a half sphere at the end of a truncated cone. But again the dominant term of the result is the one given above. For a tip radius of $R = 30\ nm$ and a tip-sample distance of of 5 Å the vdW force in vacuum is in the order of $F_{vdW} = 2\ nN$.

Electrostatic forces

Electrostatic forces act between conductive tips and conductive samples when they are at a different potential. The tip sample system can be considered as a capacitor with a distance dependent capacitance C. The Force is given by

$$F_{es} = -\frac{1}{2}\frac{\partial C}{\partial z}(V_{bias} - V_{cpd})^2 \tag{1.5}$$

where V_{bias} is the voltage applied between tip and sample and V_{cpd} is the contact potential difference. A minimum electrostatic force at the non-zero bias voltage has also been found for insulating surfaces. For such materials, the electrostatic force follows changes in in the bias voltage with a delay proportional to the resistivity of the sample [23]. The term $\partial C/\partial z$ depends on the tip geometry which can be modelled as a half sphere on a truncated cone as suggested by Hudlet *et al.* [24]. This model was experimentally tested later by Law *et al.* [25] and found to be in good agreement with the obtained results. For small distances the dominating term is

$$F_{es} = \pi \epsilon_0 \frac{R}{z} (V_{bias} - V_{cpd})^2. \tag{1.6}$$

Assuming a tip radius of $R = 30\ nm$, a tip- sample distance of $z = 5$ Å and a potential difference of $V_{bias} - V_{cpd} = 1\ V$ the electrostatic force is about $F_{es} = 0.5\ nN$. It is worth to notice that electrostatic forces not only contain a long range term. In ionic crystals where the neighbouring atoms have alternating charge signs, the electrostatic field has a short-range exponential dependency [26].

Short range forces

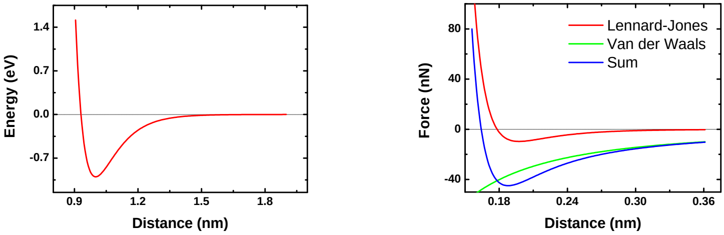

(a) Morse Potential **(b)** Force-Distance-Curves

Figure 1.1: Energy- Distance curve of a Morse potential(1.1a). Parameters used in equation 1.11 to plot the curve see below. Force versus distance curve including the long range Van der Waals force and the short range Lennard-Jones interaction (1.1b). Parameter used to plot the curves according to the equations 1.4 and 1.9: $E_{bond} = 1\ eV$, $r_m = 0.2\ nm$, $R = 30\ nm$, $H = 260 \cdot 10^{-19}\ J$

Short range chemical forces arise from the overlap of electron wave functions and from the repulsion of the ion cores. The range of these forces is comparable to the extension of the electron wave function, which means less than one nanometer. Chemical forces can be attractive or repulsive. The chemical forces can be approximated by model potentials like the Lennard-Jones[27] or the Morse potential.

The Lennard Jones potential is given by [28]

$$V_{LJ}(z) = -4\epsilon \left[\left(\frac{\sigma}{z}\right)^6 - \left(\frac{\sigma}{z}\right)^{12} \right] \tag{1.7}$$

with σ being the collision distance between two atoms and ϵ the depth of the potential well. The equilibrium distance where the potential has a minumum, is given by $r_m = 2^{\frac{1}{6}}\sigma$ and the potential has the form [29]

$$V_{LJ}(z) = -E_{bond} \left[2\left(\frac{r_m}{z}\right)^6 - \left(\frac{r_m}{z}\right)^{12} \right], \tag{1.8}$$

With E_{bond} being the binding energy of the two atoms. The exponent of the attractive term is chosen to be 6 in order to fit the vdW force[27]. The exponent for the repulsive term is set to 12 for analytic simplicity. The exponent for the force is increased by 1 and results in

$$F_{LJ}(z) = -12\frac{E_{bond}}{\sigma} \left[\left(\frac{r_m}{z}\right)^7 - \left(\frac{r_m}{z}\right)^{13} \right]. \tag{1.9}$$

The Morse potential is another empiric model for short range forces and is based on a 2-atomic molecule potential. Solving the Schrödinger equation exactly for a H_2^+ ion is quantum-mechanically possible. By choosing the parameters r_m, E_{Bond} and the decay length κ correctly, the Morse potential is a good fit for the H_2^+ problem [30]. The morse potential describes a chemical bond with the energy E_{Bond}, the equilibrium-distance r_m and κ.

$$V_{Morse}(z) = -E_{Bond}\left(2e^{-\kappa(z-r_m)} - e^{-2\kappa(z-r_m)}\right) \tag{1.10}$$

The force is defined as $F = -\partial V/\partial z$:

$$F_{Morse}(z) = -2\kappa E_{Bond}\left(e^{-\kappa(z-r_m)} - e^{-2\kappa(z-r_m)}\right) \tag{1.11}$$

Both, the Lennard-Jones and the Morse potential are suitable models to approximate the real surface potential acting on the tip.

1.3.2 Energy Dissipation in nc-AFM

The loss of energy in nc-AFM is a complex phenomena and this work does not focus on dissipation problems. Nevertheless, dissipation can also used to determine the quality factor (described in chapter 2) of the cantilever and it can be used as additional information for qualitative analysis.

The amplitude excitation signal A_{exc} in our setup is controlled to keep the amplitude A of the cantilever at a constant value. Any energy dissipation, intrinsic or caused by tip sample interaction, is damping the cantilever oscillation and requires an increase of A_{exc}. Therefore, the excitation signal is often referred to the apparent damping signal. One reason for apparent damping is that the cantilever motion can be slightly non harmonic due to tip-sample interactions. In this case a part of the oscillation energy is stored in overtones of the cantilever frequency, requiring a more increased value of A_{exc} than caused only by damping. This effect is negligibly small for larger amplitudes. Another reason for apparent damping occurs if the phase shift between cantilever oscillation and driving signal is not constantly kept at -90°. Again, a larger signal A_{exc} is needed to keep the amplitude constant. Therefore, a simultaneous recording of the phase-shift has to be done in order to get true dissipation information.

Damping in nc-AFM can be classified into two categories. The velocity dependent and the hysteresis related phenomenas. The latter arises if the tip sample interaction is bistable and has two minima [31]. Then, the cantilever force can be different while approaching and retracting. This hysteresis is caused by a repeated position change of tip apex or surface atoms.

Velocity dependent interactions can be caused by different reasons. First, it can occur if the contact potential is not compensated [32]. The difference then turns the tip-sample system into a capacitor which gets charged and decharged every oscillation cycle. This effect is referred to as Joule dissipation [33]. Brownian dissipation occurs because of coupling of atomic vibrations caused by their short-range interactions as proposed by Gauthier and Tsukada [34, 35, 36].

Controlling the distance by constant frequency shift normally used to record surface images is complicated by the fact that the frequency shift versus distance dependency is not monotoneous. Whenever a Δf_{set} is chosen below the minumum of the force-distance curve (fig. 1.1b), the controller jumps into the wrong branch, immediately leading to a tip crash. It has been suggested [37] to use the dissipation signal as a feedback for distance control due to the monotoneous nature of this signal. However, tThis operation mode leads usually to poorer results on the atomic scale. An extensive comparison between the two modes can be found in [38]

1.3.3 The Kelvin Principle

The Kelvin probe force microscope has its origin in the method developed by Lord Kelvin [39] in 1898 to measure work functions. Both methods are based on measurements with a probe and a sample. The contact potential V_{cpd}[††] between two materials is given by

$$V_{cpd} = \frac{1}{e}\left(\varPhi_1 - \varPhi_2\right) = \frac{\varDelta\varPhi}{e}, \tag{1.12}$$

where $\varPhi_1$ and $\varPhi_2$ are the workfunctions of the two materials.

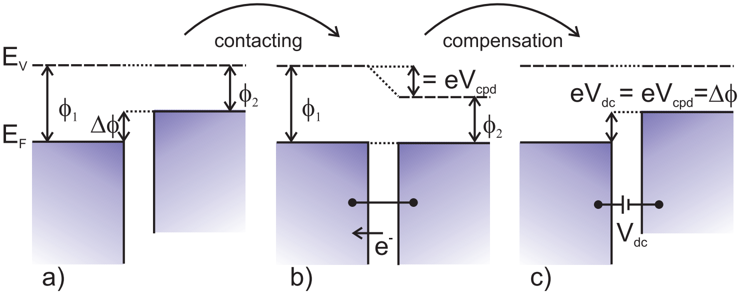

Figure 1.2: Schematic view of two materials with different workfunctions. In (a) the materials are not connected and have the same vacuum energy E_V. In (b) the materials are electrically connected and the Fermi energy levels E_F are equalizing, resulting in the contact potential V_{cpd}. Applying a dc-voltage V_{dc} in (c) compensates this contact potential.

A common method to measure the contact potential is the macroscopic Kelvin probe, where the workfunction relative to a known probe is measured. Fig. 1.2 shows the priciple of the measurement. In fig. 1.2(a) the band diagrams of the two conductive materials are shown. They have different Fermi levels (E_F) but the same vacuum energy (E_V). By electrically connecting those two materials (fig. 1.2(b)), the Fermi energy equalizes by charge transfer from one material to the other, thus inducing a potential difference V_{cpd} in the local vacuum level. In the gap between the two materials an E-field is built up corresponding to a charged capacitor. By applying a voltage $V_{dc} = V_{cpd}$ the potential difference can be compensated and the elctrostatic fields between the materials are nullified fig. 1.2(c).

The original Kelvin method is based on the modulation of a plate capacitor between probe and sample [39]. The two materials were brought

---

[††] Contact Potential Difference

close together, leaving only a very thin gap in between them. With a periodic oscillation at the frequency ω_p the distance d between the two plates is now modulated. This modulation leads to a current given by

$$I(t) = (V_{dc} - V_{cpd})\, \Delta C \cos \omega_p t. \tag{1.13}$$

ΔC is hereby the variation of the capacitance caused by the oscillation. To determine the contact potential the additional voltage V_{dc} is applied to the system. This voltage is adjusted to a value at which the field in the gap becomes zero and therefore also the current. This method has a high accuracy in the determination of potentials but no spatial resolution. Therefore, it is not possible to record local variations in the work functions of materials.

1.3.4 Kelvin Probe Force Microscopy

In Kelvin probe force microscopy (KPFM), the principle of the Kelvin probe is slightly modified and integrated in a scanning force microscope. Instead of a current KPFM measures the electrostatic force between the tip and a sample.

The first approach of atomic force potentiometry goes back to Weaver and Abraham [40] in 1991. The electrostatic force between tip and sample is given by equation 1.5. To separate electrostatic and vdW forces, an additional ac-voltage V_{ac} with the frequency ω is applied between tip and sample. The resulting potential difference

$$V_{bias} = V_0 + V_{ac} sin(\omega t) \tag{1.14}$$

with $V_0 = V_{dc} - V_{cpd}$ can be inserted into equation 1.5 which results in three additive components of the electrostatic force [41]:

$$\begin{aligned}
F_{es} &= -\frac{V_{bias}^2}{2}\frac{\partial C}{\partial z} = F_{dc} + F_{\omega} + F_{2\omega} && (1.15)\\
F_{dc} &= -\frac{\partial C}{\partial z}\left[\frac{1}{2}(V_{dc} - V_{cpd})^2 + \frac{V_{ac}^2}{4}\right] && (1.16)\\
F_{\omega} &= -\frac{\partial C}{\partial z}\left[\frac{1}{2}(V_{dc} - V_{cpd})\, V_{ac}\sin(\omega t)\right] && (1.17)\\
F_{2\omega} &= +\frac{\partial C}{\partial z}\frac{V_{ac}^2}{4}\cos(2\omega t) && (1.18)
\end{aligned}$$

with $\frac{\partial C}{\partial z}$ being the capcitance gradient between tip and sample.

Compensating the contact potential by setting $V_{dc} = V_{cpd}$ leads to a nullified first harmonic F_{ω} of the electrostatic force (equation 1.17).

Then, the dc part of the force F_{dc} becomes proportional to V_{ac}^2 (equation 1.16) causing a minimal static force and a constant bending of the cantilever. The second harmonic equation (1.18) contains the capacitance gradient and can therefore be used to perform capacitance spectroscopy at 2ω.

Calibration

Since Kelvin probe force microscopy (KPFM) only allows to measure contact potential differences, one has to know the absolute work function of either the tip or the sample. In order to get this value, the tip has to be calibrated by measuring the CPD of a well known material (e.g. HOPG) before and after the sample of interest is investigated. Applying this method, one can obtain the absolute work function of the tip and the work function of the sample can be calculated [42].

KPFM AM-Mode

In 1995 Kikukawa *et al.* [43] showed a way to image topography and contact potential difference independently. While doing standard scanning, FM-controlled microscopy on the first resonance, they determined the electrostatic interaction by tuning ω of V_{ac} to the second resonance of the cantilever. Separating the two siganls from each other allows reasonable time constants of the lock-in amplifier and the compensation circuit. Detecting the force on the second resonance is very sensitive and allows the application of very small ac-voltages ($\approx 100\ mV$). Such small voltages are important when imaging semiconducting samples, where voltages exceeding 100 mV may lead to asymmetric bias-induced band bending [44].

This method is mainly limited by the bandwidth of the photodetector. Therefore, it is often not possible to choose high Q cantilevers with resonance frequencies larger than 100 kHz. Another disadvantage of the AM-Mode is the fact that long range forces contribute to F_ω and thus the whole cantilever influences the measurement. Several measurements [45, 42] on semi conductors and junctions (solar cells) have been performed.

KPFM FM-Mode

External long range forces with the gradient $\partial F/\partial z$ changes the resonance frequency f_0 of a cantilever with the effective mass $m^\star$ as follows:

$$f_0' = \frac{1}{2\pi}\sqrt{\frac{k - \partial F/\partial z}{m^\star}} \approx f_0 \left(1 - \frac{1}{2k}\frac{\partial F}{\partial z}\right). \tag{1.19}$$

This shift is approximately proportional to the force gradient in contrast to the AM-Mode, where the force itself is detected. Kitamura *et al.* [46] presented a method employing FM-technique for topography and KPFM in 1998. The force gradient of F_{es} is given by

$$\frac{\partial F_{es}}{\partial z} = -\frac{1}{2} V_{bias}^2 \frac{\partial^2 C}{\partial z^2} \tag{1.20}$$

on the first resonance of the cantilever. The resonance frequency will be changed by the electrostatic force F_{es} according eq. 1.19. The applied ac-voltage modulates F_{es} and with it $\partial F_{es}/\partial z$ according to eqs 1.17-1.18. Following from eq. 1.19, the mechanical resonance frequency of the cantilever is modulated with frequencies f_ω and $f_{2\omega}$[‡‡]. A frequency demodulator (PLL) is used to detect the signal at $f_0 \pm f_\omega$ which then can be nullified by applying an appropriate dc-voltage V_{dc}. When this output is zero, the electrostatic force becomes minimum and V_{dc} equals the contact potential difference between tip and sample. In this way the distribution of the CPD and the topography is obtained simultaneously and the bandwidth of the photodetector does not limit the use of high Q cantilevers.

Detecting the force gradient, which decays fast when increasing probe-sample distance, allows very high spacial resolution and accurate measurements of CDP values. There are, however, also drawbacks in FM-mode. FM-KPFM does not operate on detecting an oscillation amplitude and therefore the resonant enhancement of the first overtone is absent. Therefore, large ac-voltages $(1 - 5\ V)$ have to be applied in order to get a reasonable signal and the CPD is not separated from the topography.

1.3.5 Comparison between AFM and STM

As mentioned above STM and AFM use different physical values for the measurements. While STM is limited to electrically conductive samples, AFM has basically no limits in its application as long as the sample is flat enough. On the other hand, the quality of AFM images is often dissapointing compared to STM measurements. While STM reveals intermolecular details, AFM has already troubles to achieve molecular resolution. The reason for this is the nature of the detected signals. Since the tunneling current decays exponentially, its main contribution comes from the very last atom on the tip apex. Atoms only one Å farther away from the surface contribute one order of magnitude less to the

---

[‡‡] ω has to be larger than the scan speed but lower than the bandwidth of the PLL. Typically frequencies of $\approx 1\ kHz$ are used.

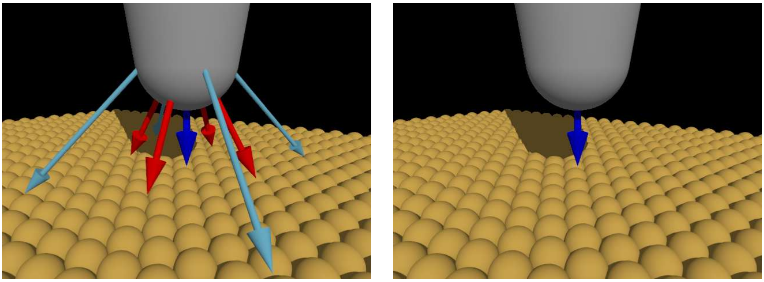

(a) Forces in AFM **(b)** Tunneling current in STM

Figure 1.3: Schematic visualization of the signals contributing to the contrast formation in AFM (1.3a) and STM (1.3b). In STM, only the exponentially decaying tunneling current is detected. Therefore no long range interactions contribute to the image. In AFM short range chemical and long range vdW and electrostatical forces are detected. While the latter can be compensated by applying an appropriate voltage to the system, the two others contribute to the image contrast in any case.

resulting current. In AFM, a mixture of long and short range forces is detected. While it is possible to minimize the contribution of the electrostatic forces, the vdW contribution cannot be reduced. This short and long range contributions put the tip in a much more crucial position. A rather blunt tip will inevitably average the long range forces over a large scale which results in a more blurry image. In order to achieve intermolecular resolution the tip has to be very sharp with a small opening angle.

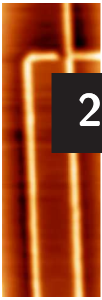

2 Experimental Setup

2.1 The Ultrahigh Vacuum System

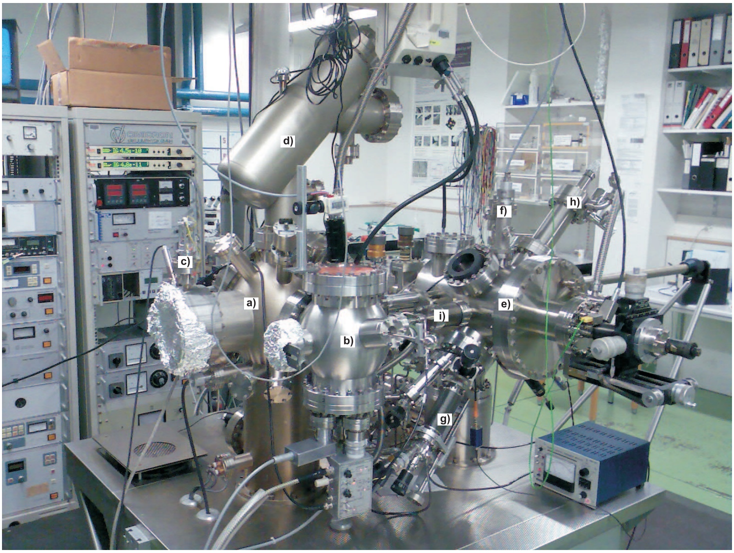

Figure 2.1: UHV system: Located on the left part is the analysis chamber (a) with the AFM/STM(b), the LEED/AES system (c) and the XPS (d). The preparation chamber (e) is located on the right. Visible on the picture are the sputter gun (f), the three cell evaporator (g), the atom source gun (h) and the quartz micro-balance (i).

The home-built AFM is based on a prototype built in 1993 [47]. It is located in an UHV system [48] divided into three different chambers partly shown in figure 2.1.

The lock contains a quick release fastener flange for fast tip and sample introduction. It also contains an oxygen heating stage and is connected to a small turbo pump and individually pumpable/evacuable down to a pressure of $< 8 \times 10^{-8}$ $mbar$.

The preparation chamber(P-chamber) is the part where the main turbomolecular pump is connected to. There are several devices installed to enable advanced sample preparation. A three-cell molecular evaporator is used for molecule and salt (KBr, NaCl) deposition and the home-built transferable evaporator is used for gold deposition. The manipulator has an e-beam heater included for high temperature treatment. Additionally a quartz micro balance is installed to calibrate evaporation rates.

For surface preparation a sputter gun is installed as well as an atom source gun for gas treatment. To obtain clean ionic crystal surfaces the in- situ cleaving knife is used. The preparation chamber is additionally evacuated by a ion- getter and a titanium sublimation pump.

In addition to the AFM/STM, the analysis chamber(A-chamber) contains analysis method instruments such as LEED[*], AES[†] and XPS[‡]. This chamber is evacuated by a ion-getter and a titanium sublimation pump.

To evacuate the system, first the prevacuum and turbomolecular pumps are engaged. The turbopumps alone can reach a pressure of around 10^{-9} $mbar$ after a certain time. The residual gas is mainly water sticking to the chamber walls. After a 12 hour bakeout most of the water is evaporated and pumped out of the system. Engaging ion-getter and titanium sublimation pumps allows a final A-chamber pressure in the low 10^{-11} $mbar$ regime. The pressure in the P-chamber is usually one order of magnitude higher.

Inside the chamber, tips and samples are moved by a system of manipulators and a wobble stick.

2.2 The Atomic Force Microscope

The AFM inside the chamber is mounted on a stage which is suspended by four springs and damped by an eddy current damping system. The parts of this damping system are visible in image 2.2a.

The deflection of the cantilever is measured by a four-quadrant photodetector using the beam deflection method [49] shown in image 2.2b. The light of a superluminescent diode [50] is coupled into a gold coated glass

---

[*] **L**ow **E**nergy **E**lectron **D**iffraction

[†] **A**uger **E**lectron **S**pectroscopy

[‡] **X**-ray **P**hotoelectron **S**pectroscopy

fiber and introduced into UHV via a swage-lock teflon feedthrough [51]. The light beam is then focussed by a lens system at controllable distance and deflected by a motorized mirror to the backside of the cantilever. Reflected by the cantilever, the beam is led to a second mirror and from there to the four-quadrant photodetector. The signal of the detector is directly preamplified in UHV which guarantees a better signal to noise ratio with a bandwitdh of 3 MHz [52].

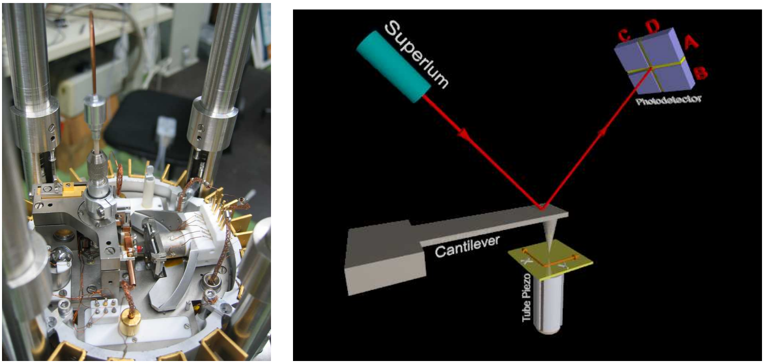

(a) UHV AFM **(b)** Scheme of beam deflection

Figure 2.2: 2.2a: Image of the AFM system during maintenance work. 2.2b: Model of the beam-deflection method. The light reflected by the cantilever is detected by a four-quadrant photodetector which is able to record normal, lateral and torsional displacement of the cantilever.

The sample holder is mounted on a tube piezo which allows x,y movement as well as adjusting the tip-sample distance. This assembly is attached to a sledge which can be moved in two dimensions by three piezo stacks for coarse approach. While imaging the sample is moved and therefore the beam-lever system remains fixed. The cantilever itself is mounted on a piezo crystal in order to allow operation in dynamic AFM mode.

Additionally to AFM operating modes the instrument is designed to be operated as STM. The small tunneling current is pre-amplified in UHV with a switchable resistor of 100 $M\Omega$ or 10 $G\Omega$. The system further is offers the possibility to apply a bias voltage to either the sample or the tip.

2.3 Electronic Detection Circuit

The electronic setup has changed several times during this work. However, the composition of the different controllers has not changed. A schematic view of the circuit is shown in figure 2.3. For the majority of the measurements, the Nanonis [53] electronics and scan software were used. Previously, the electronic setup was composed by home-built electronic parts [54] and software. For a short time, a Nanosurf easy PLL [55] was employed.

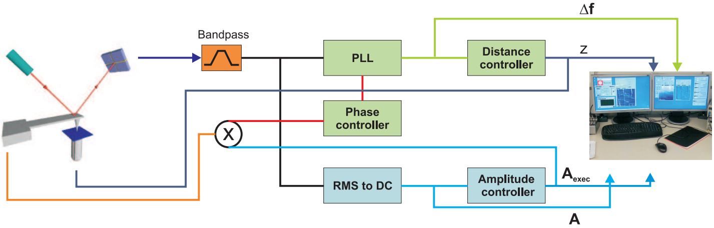

Figure 2.3: Schematic sketch of the feedback loop circuit for dynamic force microscopy. The control circuit is described in the text.

The cantilever with the Eigenfrequency f_0 is located in a feedback loop. As already mentioned, the frequency $f_{exc} = f_0$ and the amplitude A are kept at a constant value. The detected oscillation signal is preamplified in UHV. Afterwards the signal is separated. One line is going into a RMS-to-DC converter in order to obtain the amplitude. This value is fed in the amplitude controller which controls A_{exc} to keep A at a constant level.
The other line is fed into a PLL which is measuring the difference between the frequency f and the frequency setpoint f_{set}. This difference is the error signal of the frequency shift. It is also fed into the distance controller (usually containing a P-I controller) which is adjusting the tip sample separation to minimize the error signal. The reference oscillation of the PLL is shifted by a previously adjusted phase φ and multiplied by the output A_{exc} of the amplitude controller. This signal is driving the piezo which is exiting the cantilever at its resonance frequency, at the optimal phase and with the the adjusted amplitude. The Nanonis system is integrated after the four-quadrant detector and fed by the normal $(A - B)$ and lateral $(C - D)$ oscillation signal, as well as the sum (image 2.2b).

2.4 KPFM Specialities

In order to obtain more accurate height informations on heterogenous surfaces. The electrostatic forces have to be compensated, so that they no longer contribute to the topography [56, 57]. This compensation is either done statically by applying a bias voltage or dynamically by using KPFM.

When operating the microscope in AM-KPFM-mode, a second lock-in is needed as shown in figure 2.4. The normal oscillation signal $(A-B)$ is high-pass-filtered in order to separate f_0 from f_1 and then fed into the lock-in which uses an oscillation, generated by a frequency generator, on the 2nd resonance of the cantilever as reference. The output then is fed into our home built Kelvin controller.

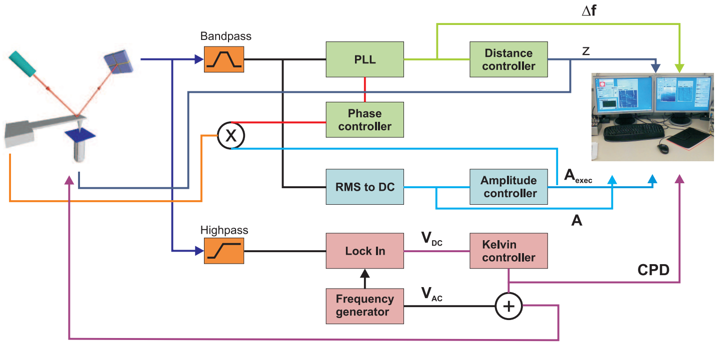

Figure 2.4: Same sketch as in fig.2.3 with the circuit for the KPFM Am-Mode cf. section 1.3.4.

On bulk insulating crystals it is often not easy to run the microscope in KPFM mode because a dynamic compensation of the CPD is not always possible. In those experiments the contact potential difference was compensated by sweeping the bias voltage while keeping the tip at a close distance to the surface. The resulting $V_{bias} - \Delta f$ curve has a parabolic shape with its minimum $V_{bias,0}$ equals V_{cpd} [58]. On heterogenous surfaces it is suggested by Sadewasser [59] to determine V_{cpd} on both materials and then choose $V_{bias} = (V_{cpd,1} + V_{cpd,2})/2$. Sadewasser also claims that on surfaces with more than two different V_{cpd} this solution is no longer valid and height measurements are flawed.

2.4.1 Compensating Capacitive Coupling

Capacitive cross-coupling between the instruments wiring hampers high resolution KPFM imaging [44]. The compensation of the effective contact potential is often shifted by several mV. Therefore, an additional signal input which allows an almost perfect compensation of this coupling signal was developed. To achieve that, a phase stable ac-signal of the same frequency is fed into the system. The phase and the amplitude of this compensation signal is set in a way that the lock-in signal becomes minimal ($< 100\ mV$), when the contact potential is compensated by applying a dc-bias voltage. In order to adjust the phase, the bias voltage afterwards is increased by 500 mV allowing a more accurate adjustment. After this procedure the Kelvin controller can be engaged.

2.5 Calibrations

In order to obtain quantitative, accurate results several things have to be calibrated. The most important parts are the scan-piezo, the oscillation amplitude of the cantilever and its Q-factor. Therefore, a brief overview over the calibration methods is given here.

2.5.1 Calibration of the Piezo

Calibration of the z-piezo

The z-piezo is responsible for the topography measurements. Usually, it is calibrated by measuring step heights on well known materials (e.g. Si(111), NaCl, KBr(001)). Sometimes, it is not easy to determine wether a step is one or more layers high. Accumulating enough data overcomes this problem, as with more steps measured, a quantization of the step heights becomes visible, allowing an exact determination of single-steps. Measuring the height of the single steps and comparing it with theoretical values yields to a calibration factor which allows a readjustment of the z-piezo calibration.

Calibration of the x-y-piezo

To calibrate the x-y-piezo usually an image with atomic resolution is used. Processing a FFT[§] on such an image leads immediately to the atomic periodicity. Comparing this value with literature leads again to a calibration factor which is used for the x-y-calibration. It is important to mention that such a calibration is only accurate for the fast scan

---

[§] Fast Fourier Transformation

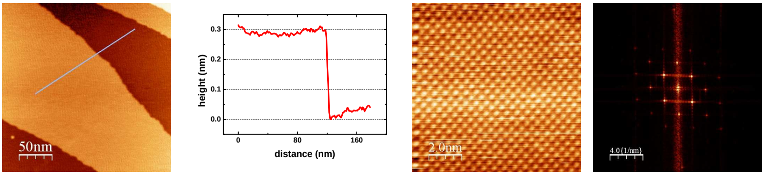

(a) NaCl **(b)** Stepheight **(c)** KBr(001) **(d)** FFT image

Figure 2.5: Topography 2.5a of a NaCl(001) surface with a few steps and the linesection 2.5b along the line. The NaCl step height is 2.825 Å, while we measure an averaged value of 2.85 Å. Atomic resolution on KBr. Topography 2.5c and corresponding FFT 2.5d. The FFT gives a periodicity of 6.69 Å in y and 6.59 Å in x-direction. The y-direction is much more drift affected and in order to obtain accurate values the FFT image has to be taken from a scan under 90°where the fast scan direction is equal to the y-axis.

direction. The slow scan direction is too much drift affected to provide exact information. To calibrate the other axis, one usually repeats the scan with a 90° tilted scan direction.

2.5.2 Calibration of the Amplitude

The oscillation amplitude A can be determined with help of the calibrated[¶] z-piezo. The principle idea is to measure the z-extension for different amplitude values [60] at constant minimum tip sample distance. On insulation surfaces the distance is usually controlled by keeping the frequency shift constant. Because the frequency shift is dependent on the oscillation amplitude $f \propto A^{-3/2}$ [29, 61], it has to be readjusted after every change in the oscillation amplitude.

The procedure is the following: The controller is set to an amplitude A_0. A Δf_0 setpoint is chosen and the tip approached to the sample. After reaching an equilibrium state, the z-signal z_0 is recorded. A change in the amplitude to $A_1 = c \times A_0$ leads to an adjusted frequency shift of $f_1 = f_0 c^{-3/2}$. Again after letting the tip position become stable the signal z_1 is obtained. The difference $z_1 - z_0$ divided by the difference of the oscillation amplitudes $A_{osc,1} - A_{osc,2}$ leads to a conversion factor nm/V which then can be used to calibrate the absolute amplitude.

[¶] Such calibrations are usually done by measuring the step heights on well known materials.

The new Nanonis SPM control system [53] offers the possibility to remote control certain functions via ethernet. To perform the calibration automatically, a LabView [62] application was programmed. The automated procedure now allows to average over several hundred amplitude changes rather than only two to three with the manual method. However, even the automated procedure leads to quite large errors of around 10% A more detailed description of the application can be found in appendix B.

2.5.3 Calibration of the Q- Value

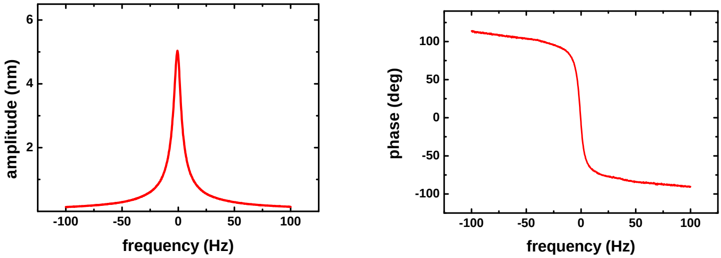

(a) Amplitude vs.Δf **(b)** Phase vs. Δf

Figure 2.6: Amplitude (2.6a) and phase (2.6b) vs. freuqency shift curves. $f_0 = 150\ kHz$, $Q = 31000$

The Q-factor is a measure for the dissipation in nc-AFM. This intrinsic cantilever dissipation is can not be avoided. Since the Q-factor is inverse proportional to the force sensitivity it is desirable to have cantilevers with high Q-values [15]. Operating in air the Q-factor is limited to values of a few hundred because of viscous damping of the environment. In UHV, only internal and surface effects are responsible for the damping and hence much higher Q-factors up to several 10^6 are obtained. There are different ways to determine the Q-factor. One is to sweep the frequency and simultaneously record the amplitude A or the phase ϕ of the cantilever oscillation. The relations between frequency shift and amplitude or phase respectively, are derived from the equations of motion for a free cantilever [63]:

$$
\begin{aligned}
A(f) &= \frac{A_0}{\sqrt{\left(1\,(f/f_0)^2\right)^2 + (f/f_0 \times Q)^2}} && (2.1)\\
\phi(f) &= \arctan\left(\frac{1-(f/f_0)^2}{f/f_0}Q\right) + \phi_0, && (2.2)
\end{aligned}
$$

where f_0 is the resonance frequency of the free cantilever, A_0 the amplitude at f_0 and Q the quality factor.

The quality factor can also be derived without any excitation from the thermal noise spectrum. The analytical curve below is fitted to the resonance peak [64, 65]

$$
S(\omega) = \frac{2k_B T\omega_n^3}{D_n Q\left((\omega^2-\omega_n^2)^2 + \frac{\omega 2_n \omega^2}{Q^2}\right)}, \tag{2.3}
$$

where Q is the quality factor, k_B the Boltzmann constant, D_n the spring constant and ω_n the eigenfrequency of the n-th eigenmode.

High enough Q-factors can also be accurately determined by measuring the decay behaviour of the lever after switching off the excitation. The ring-down follows an exponential decay and can be fitted with the following formula [65]

$$
A(t) = A_0 \exp\left(-\pi\frac{f}{Q}(t-t_0)\right), \tag{2.4}
$$

where A_0 is the excitation amplitude and t_0 the switch-off time of the external oscillation.

2.6 Sample and Tip Preparation

2.6.1 Properties and Treatment of the Cantilevers

We used commercial [66], microfabricated, rectangular cantilevers with integrated tips (fig. 2.7). They are fabricated from highly n-doped silicon to allow combined AFM-STM measurements and to prevent charging. The tips have a pyramidal shape formed by etching processes. In order to obtain atomic resolution the tip apex has to be as sharp as possible. Ideally, only the front atom interacts with the surface. The typical tip-radius of the used levers is below 10 nm. For non-contact measurements stiff cantilevers with spring constants around 60 N/m help to increase stability and reduce noise effects. In order to improve the optical signal, levers with aluminum reflective coating of approximately 30 nm on the

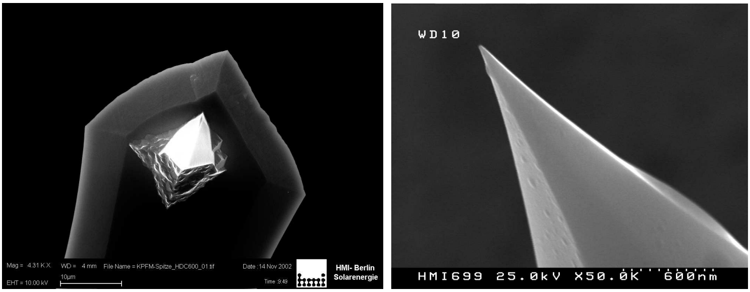

(a) Microfabricated cantilever with. . .

(b) . . . an integrated tip

Figure 2.7: SEM images of a microfabricated cantilever with integrated tip.

thickness t	$7.0 \pm 1\ \mu m$
width w	$38 \pm 8\ \mu m$
length l	$225 \pm 10\ \mu m$
force constant k	$21 - 98\ N/m$
tip height h	$10 - 15\ \mu m$
resonance frequency f_0	$146 - 236\ kHz$

Table 2.1: Properties of a reflective coated cantilever

detector side[‖] were used. This enhances the signal by a factor of roughly 2.5 but decreases the Q-factor from around 30k to around 15k. Table 2.1 shows a list of typical cantilever properties.

The microfabricated cantilevers are glued on a tip holder and adjusted with the help of an adjustment stage, guaranteeing an optimal lightpath in the microscope. After introduction into the vacuum, the holders were heated to 120°C in order to get rid of water and other contaminants[**]. Afterwards, we removed the thin coating layer of silicon oxide by Ar^+ sputtering the tip for about 2 minutes at a beam energy of $E = 1\ kV$. Other possible removal treatments are in-situ annealing at 900°C [67] or HF-etching [68] before introducing into UHV.

[‖] other side than the tip

[**] In the past few months we skipped the annealing process to presumably avoid diffusion from the glue to the tip

	sputtering	**annealing**
Cu(111)	1 keV, 20 μA, 25 min	790 K, 20 min

Table 2.2: Parameters for Ar^+-sputtering- annealing cycles.

2.6.2 Sample Preparation

Under atmospheric conditions all kinds of particles and adsorbates are covering a sample forming an adlayer. The chemical composition and structure of this layer is generally not well defined. Thus, samples exposed to atmospheric pressure are complex structures, with the adlayers preventing a clear analysis of the underlying surface strucure. In ultrahigh vacuum several techniques exist to prepare clean and well defined surfaces.

Brittle materials, such as alkali halides, are prepared by cleaving. Cleaving only works along certain crystallographic directions. For metallic surfaces usually sputter-annealing cycles are used. By bombarding the surface with noble gas ions the residuals in the topmost atomic layer are sputtered away. Subsequent annealing is necessary to remove noble gas adsorbates and heal out the crystallographic structure of the metal. Since this process also segregates bulk impurities to the surface those cycles have to be repeated several times [69]. Typical parameters for copper preparation are listed in table 2.2.

A further possible treatment for alkali halides is electron bombardment. In order to obtain rectangular monoatomic deep pits in the surface, it is held into a electron beam generated by the LEED gun [70]. The electrons form excited color centers inside the top layers of the crystal which diffuse to the surface and leave the sample there [71], forming stochiometric pits. This kind of sample preparation is used to lower the mobility of adsorbates on the surface and has lead to the first molecular resolved images of molecules on an insulating surface [72]. The irradiation process induced by the LEED gun is a more intuitive process (parameters: $E = 1\ kV$, $I_{fil} \approx 1\ A$, $I_{emission} = 65\ \mu A$, $t_{exposure} = 5\ s$ and $T_{sample} = 150°C$).

3

Porphyrin Molecules on Alkali Halide Crystals

The focus of this work was the investigation of organic molecules on insulating surfaces. Generally, the diffusion barrier of molecules is very low compared to the intermolecular forces which generally leads to rather big clusters (diameter $\gtrsim 5\ nm$) on the substrate surface rather than ordered layer structures.

3.1 Motivation

In order to selectively address monoatomic molecular devices, they have to be electrically decoupled from the substrate. One way to achieve this is to use bulk insulating crystals. Alkali halides offer some distinctive advantages compared to other surfaces. Flat surfaces with monoatomic steps and large terraces are easily prepared and the electron bombardment described in chapter 2 leads to a well structured surface. Additionally, those materials have rather large unit cells, which allow to obtain atomic resolution fairly easy [73, 74]. The restriction of those materials are mainly their susceptibility to water and other solvents. In order to keep the surface at a well defined state, those materials have to be kept in UHV.

The adsorption and self assembly of functional organic molecules on surfaces offers fascinating perspectives for nanometer sized electronic and optoelectronic devices. For the construction of such devices, nanowires are essential components to provide an efficient transport of electrons and/or excitons along specific directions. Self-assembled structures provide some distinct advantages compared to engineered devices, such as self healing and a decreased number of defects [4, 75, 76].

For a long time molecular growth studies were limited to metal surfaces, which were then studied by STM experiments (for a few selected examples see [77, 78, 79, 80, 81]). On metals, porphyrin based molecules are adsorbed with their core-plane parallel to the surface, not allowing any kind of $\pi - \pi$ [82] stacking. This stacking is mandatory for porphyrins to allow electronic or optoelectronic exchange among themselves. I will show in this chapter, that nc-AFM is an ideal technique to study molecular assemblies. However, so far nc-AFM studies still have potential for improvement as they generally lack of submolecular resolution [83, 84, 85, 86, 87].

3.2 Binding Mechanisms

Comparing the adsorption behaviour of large molecules on metallic and insulating surfaces revealed some distinct differences. Molecules with an aromatic core parallel to the surface form ordered monolayers if they are big enough [88] or if they are allowed to form hydrogen bonds [89] which cause a bigger intermolecular interaction. In addition to this, localized $\pi-$ bonds can form if the core is close enough to the surface [90]. Alternatively, flexible end-groups can arrange themselves individually, with each of them forming a vdW-bond with the surface.

On ionic crystals the interactions described above are expected to be significantly smaller. The larger energy gap of insulators causes a weaker polarizeability and weaker vdW forces, which are about a factor of two smaller than on metals [22]. On ionic crystals we expect bonds to form between polar endgroups with the surface ions of the crystal. However, the corrugation of this surface potential is so weak, that most molecular species diffuse freely over the surface and rather agglomerate in clusters at step edges than in ordered layers on the terraces.

The corrugation of the electrostatic potential is greatly enhanced at steps, kinks and cornersites. Therefore, those sites become ideal adsorption points for polar molecules. The lateral electric field at step edges can be approximated with $\approx e/a^2 \exp(-2\pi x/a) \cos(2\pi y/a)$, with a being the lattice periodicity. It is adviseful to choose molecules with polar endgroups separated by $d = na$ $(n \in \mathbb{N})$, or even easier only one polar endgroup.

3.3 Porphyrin Molecules

In this work mainly molecules of the porphyrin family were used. In certain experiments also other molecular derivates were involved. The name porphyrin is derived from the greek word for purple;*porphura*. All porphyrins absorb light in the visible range and therefore appear colored [91] for the human eye. The chemical structure of the porphyrin macrocycle is shown in figure 3.1. Four pyrrole-rings are linked cyclic by four methyne groups to build an extended aromatic π-system with 18 π-electrons per core [92]. This part corresponds also to the simplest molecule of the family, the Porphin ($C_{20}H_{14}N_4$).

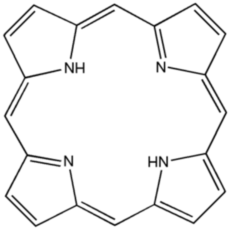

Figure 3.1: Chemical structure of the porphyrin core: Porphin

The core has a four-fold symmetry and in addition the two hydrogen atoms in the middle can be substituted by a metal atom (e.g. Fe, Mg or in this work exclusively Zn). The porphyrin macro cycle can be augmented with functional groups in many ways. In the present work most of the time two opposite sides were occupied by one 3,5-di(tert-butyl) phenyl group each. Preferrably the other two positions were amended with functional groups which improve or ease the adsorption process of the molecules on insulating surfaces. Details will be discussed in the following chapters.

Porphyrin molecules also play different important roles in nature. The most important ones are in photosynthesis and the transport of oxygen [92]. In the metabolism of mammals oxygen is transported by red bloodcells, the hemoglobine. The major part of it is the hem-group, a iron-(II) substituded porphyrin [93]. The photosynthesis taking place in plants uses chlorophylls which are magnesium-(II)-chlorin complexes with chlorin being a porphyrin derivate [94]. To allow photonsynthesis the porphyrins absorb red light which is responsible for the green color of all plants. Details about the synthesis of the used porphyrins can be found in [95].

Fig. 3.2 shows the chemical structure of the two employed molecules. For convenience the molecule in fig. 3.2a will be referred to as tetracyanoporphyrin (symmetric) and 3.2b as monocyanoporphyrin (asymmetric). The two 3,5-di(tert-butyl)phenyl- groups will be referred as sidegroups.

3.4 Tetracyanoporphyrins on KBr

Atomically flat KBr surfaces were prepared by cleavage in air or UHV followed by an annealing step in UHV to get rid of surface charges [96]. The clean surface was irradiated for approximately 5 seconds by a 1keV electron beam ($I_{Emission} = 65\ \mu A$). The obtained pit size and number

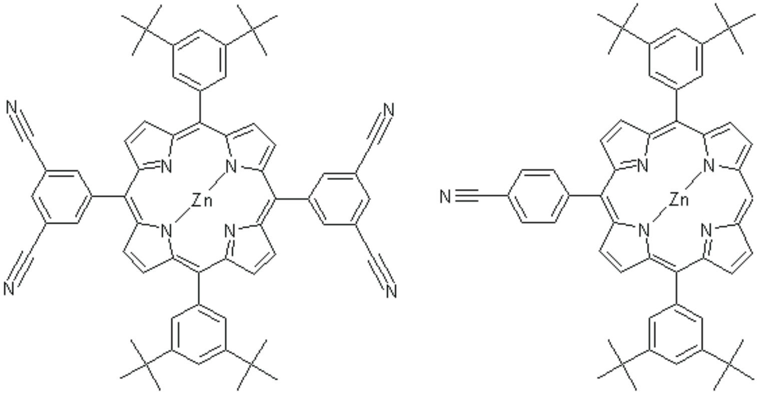

(a) Tetracyanoporphyrin **(b)** Monocyanoporphyrin

Figure 3.2: Chemical structures of the employed molecules. The symmetric shaped tetracyanoporphyrin on the left and the asymmetric monocyanoporphyrin on the right

is dependent on the intensity of the radiation and the duration of the exposure [71, 97].

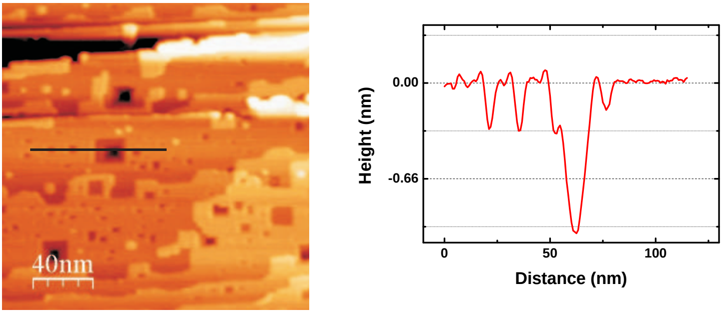

(a) Irradiated KBr **(b)** Cross-section

Figure 3.3: (3.3a): Topographical image of the irradiated KBr(100) surface. Frame edge = 200 nm, $\Delta f = -10\ Hz$. (3.3b): Cross-sectional view over several pits. Most of the cavities are monoatomic deep and have a diameter between $2 - 30\ nm$

The clean irradiated KBr surface is shown in fig. 3.3a. Rectangular pits are regularly distributed all over the surface. The vast majority of the pits is monoatomic deep and about $2-20$ nm big. Those pit structures have been successfully employed to trap different organic molecules [83, 72, 86, 87].

After irradiation tetracyanopophyrin molecules were evaporated thermally. The sublimation temperature was around $180°C$ and the sample was kept at $80°C$. The evaporation rate was calibrated with a quartz micro balance crystal and determined to be $\approx$ 2 Å/min. To obtain surfaces that showed molecular coverage and also clean substrate parts, $\approx 1/2$ monolayer of material was deposited.

Fig. 3.4a shows the surface after the evaporation. Molecular clusters are attached to the small rectangular islands. In the left part of the image one can also see partially filled pits. There are no agglomerates of molecules on flat terraces as expected since the diffusion barrier of those molecules is to small. The longer step and pit edges also show an enhanced contrast. Unfortunately, due to the poor image quality it is not possible to determine, wether this enhanced contrast is caused by a step decoration or simply by the imaging tip. Those step decorations have a height of roughly $1-1.5$ nm and therefore, could indicate the presence of a molecular decoration. However, zooming in and lowering the tip sample separation suppressed those features, resulting presumably from removing the decoration with the tip. While the molecules were prevented from diffusing off the surface, neither the pit nor the islands allowed them to form an organized structure. The height of the clusters varied between 1.5 and 2.0 nm and the round, clustery shape of the agglomerates didn't indicate any order. Sequentially, with those observations, flat, extended areas with molecular order were not observed.

As a consequence of these results the sample was annealed at $130°C$ for a few seconds. This temperature was chosen to be high enough to allow the clusters to break apart and the molecules to diffuse around on the surface but prevent them from evaporating from the surface. Fig. 3.5a shows the sample after the annealing process. The decorations at all the edges are gone. In exchange, molecular carpets with a diameter of ≈ 20 nm and a height of 1.3 nm have been formed. The regular shape of the carpets and the homogenious height indicate an ordered structure of the molecules. Unfortunately, lowering the tip sample separation led to a more blurry contrast which indicated a tip induced movement of individual molecules and even bigger parts of the agglomerates.

To gain more informations about the molecular carpet, two sets of ten force distance curves were performed along the straight line shown in fig. 3.6a. The first three curves were taken on the KBr, followed

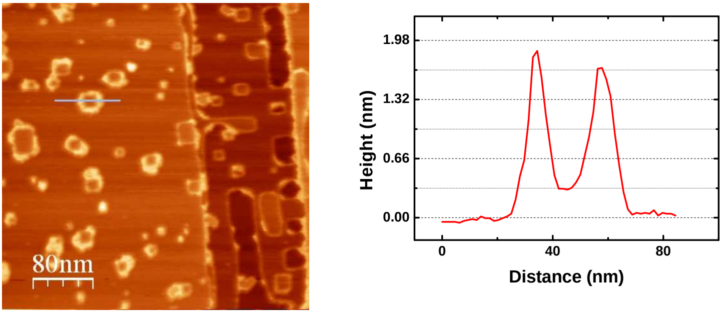

(a) Tetracyanoporphyrine molecules on KBr

(b) Cross-section

Figure 3.4: (3.4a): Topographical image of the structured KBr(100) surface decorated with tetracyanoporphyrins. Frame edge = 400 *nm*, controlled on constant dissipation. Detailed description is found in the text. (3.4b): Cross-sectional view over a decorated island and the surrounding area reveals a non-uniform height of the molecular clusters of about $1.5 - 2\ nm$

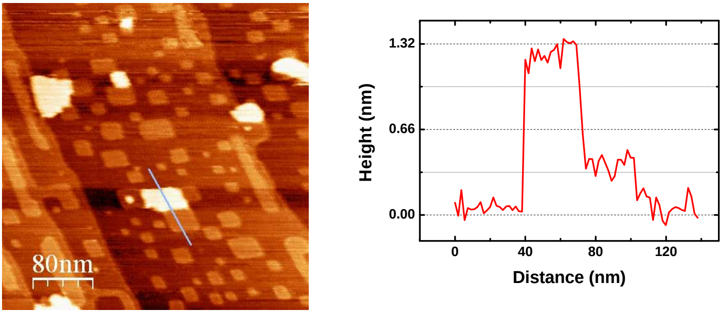

(a) Tetracyanoporphyrine molecules on KBr after flashing the sample.

(b) Cross-section

Figure 3.5: (3.5a):The decorated sample after flashing it to 130°*C*. Detailed description in text. Frame edge = 400 *nm*, controlled on dissipation. (3.5b): Cross-sectional view over a carpet of molecules an island and the underlying substrate. The molecular carpet has a height of roughly 1.3 *nm*.

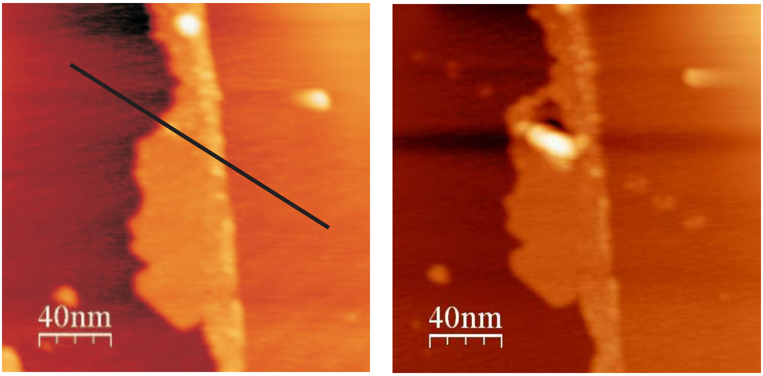

(a) Molecular carpet before...

(b) ...and after performing distance curves.

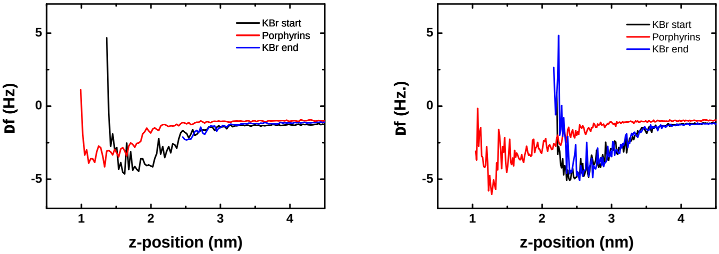

(c) force-distance curves

(d) force-distance curves

Figure 3.6: (3.6a): Topography images (3.6a&3.6b) of a molecular carpet. Ten force distance curves were performed along the black line. (3.6b): The same carpet after the spectroscopy. During the first series of curves the tip picked up material from the agglomerate and subsequently deposited the molecules on the surface during the second series. The placed molecular clusters are well visible and additionally one can see the damage the tip did to the carpet. Figs. 3.6c and 3.6d show three subsequent averaged force distance curves. The black one is recorded on bare KBr. The red curve is taken on the molecular carpet and the blue curve again is taken on the KBr. The z-position is recorded relative to a fictive point and the topography difference between the molecules and the the KBr levels is substracted.

by four curves on the molecules and ended by another three curves on the substrate. During the first series the tip picked up material from the molecular carpet. Fig. 3.6b clearly shows the crash site on the island. Interestingly the molecules then were deposited during the following spectroscopy curves on the KBr surface. The force distance curves have been divided into three groups (KBr-molecules-KBr). Each bundle was then averaged and the result is displayed in fig. 3.6c and 3.6d. The black curve shows the spectroscopy on the upper KBr terrace (right half), the red curve is taken on the molecular carpet and the blue curve on the lower KBr terrace. The topography differences have been substracted so that the start point of each curve has the same tip-sample separation. There was no bias applied to the sample. The shift caused by the molecules is close to 1 nm for the a similar force, indicating a clear difference in the interaction forces between bare KBr and molecular carpet.

The obtained results clearly indicate that small clusters of tetracyanoporphyrin molecules are not completely mobile on the KBr(100) surface. However, if the thermal energy is high enough ($\gtrsim$ room temperature) the clusters tend to diffuse away from the flat surface to higher coordinated sites, such as step edges, pits, islands, defects and other impurities. It is further noticable that annealing the sample at 130$^\circ C$ leads to a complete rearrangement of the molecular structure. The roundish shaped molecular clusters sitting at the island edges were mobilized and had enough thermal energy to rearrange themselves resulting in larger but more flat islands. However, the structure inside those carpets is still unknown as we never observed any regular patterns nor resolved single molecules. Lowering the tip sample distance usually led to a pickup of material or a complete tip crash.

3.5 Monocyanoporphyrins on KBr

The following sections describe the adsorption of [10,20- bis(3,5-di-tert-butylphenyl)- 5- (4-cyanophenyl) porphyrinato(2)- kN21, kN22, kN23, kN24]zinc(II) molecules (shown in fig. 3.2b & 3.7) on various substrates.

3.5.1 Single Wires along Pit Edges

After the irradiation described in section (2.6.2) sub monolayer quantities of porphyrin molecules were thermally evaporated on the substrate. Typical evaporation-rates were between 1 and 3 Å$/min$. During the evaporation process of roughly 60 seconds the sample was kept at 80$^\circ C$ to allow a limited mobility of molecules.

Figure 3.8a shows a nc-AFM image of the KBr(001) surface at a constant frequency shift of $-20\ Hz$, after the evaporation of the monocyanoporphyrin molecules. The structure of the irradiated pattern is still apparent and decorated steps are clearly visible. Atomic resolution was obtained on flat terraces and inside the pits but not close to any molecular structure. The picture shows also that only the straight step edges are decorated with the porphyrins. As soon as the steps are rounded the molecular wire becomes interrupted or the molecules do not aggregate there at all. However, the wire remains intact along kinks as marked in fig. 3.8a.

At those dislocations and at cornersites where two wires converge, we observe a slight augmentation in the wire structure of about 1 Å. This is either explained by a change in the molecular order caused by the offset (or the joint at cornersites) or by the weaker bound molecules at the wire ends. Both of the two reasons could lead to a increase in the topography signal, either caused by overlapping molecules or by a tip induced vertical movement.

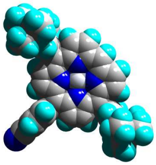

Figure 3.7: Cyanoporphyrin with one 4-cyanophenyl- and two 3,5-di(tert-butyl)phenyl- groups, spacefill model. Dipole moment on the nitrogen atom = $4.37\ D$ [98]

Figure 3.8b is a top down scan and reveals more details about the molecular wire itself. In the lower part of figure 3.8b an instability is observed where part of the molecular wire is removed, revealing the KBr step underneath it.

The cross section in figure 3.9a shows the dimensions of the wire more precisely. The height of the structure ($\approx 1\ nm$) corresponds roughly to the length of the porphyrin, while the different profiles of the wires growing in different directions in fig. 3.8a indicate an asymmetric shape of the tip. The small peak of ≈ 0.5 Å height corresponds to the faint vertical dotted line visible in figure 3.8b. These dots have a distance between each other of $\approx 0.6\ nm$ which corresponds to the distance between porphyrins as shown in figure 3.9b. This distance also concides to the length of two KBr unit cells. This sub-structure first was not observed too often and it cannot be ruled out that the substructure is observed due to an imaging artifact rather than due to the real molecule structure. Further studies and measurements are needed to clarify this question.

Another important observation is that the step decorations were stable over a quite large distance. The reason for them to get broken was never the length of the structure but always series of kinks, corners or other interruptions of the underlying step edge.

If we consider possible arrangements of the molecules along the pit edges it is most likely a similar mechanism as shown in [72] where the strong electrostatic potential at the vertices of the pits trapped the negatively charged chlorine atom of the molecule. In our case the sinusoidal potential along the pit edge may provide an interaction with the nitrogen atom of the molecule, strong enough to prevent the porphyrins from diffusing away. Therefore, it is likely, that the molecules stand on the substrate with the cyano-group pointing downwards and the plane of the porphyrin body perpendicular to the pit edge direction forming the $\pi-\pi$ structure as described in [82, 100] and shown in figure 3.9b. Since the porphyrins do not stack centered, they are most probably tilted towards the substrate plane.

The potential across flat terraces is not strong enough to prevent the molecules from diffusing away. Therefore, no porphyrins were observed on these flat areas. Even more than in [72] the potential enhancement

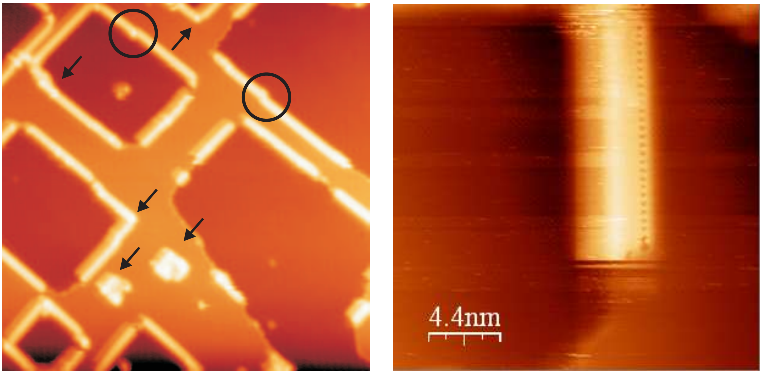

(a) Decorated pit edges **(b)** Zoom of a single wire

Figure 3.8: (3.8a) Topographical overview of the decorated steps on KBr. The arrows mark small protrusions at joint-sites of 2 molecular wires. Those protrusions occur at dislocations and corners and are about 1 Å higher than the wire. The circular marks indicate wire-growth over small dislocations. Frame edge = 100 nm, $\Delta f = -20\ Hz$, $z = 2.5\ nm$. (3.8b) Topography of a decorated step edge. Frame edge = 22 nm, $\Delta f = -20\ Hz$, $z = 2\ nm$.

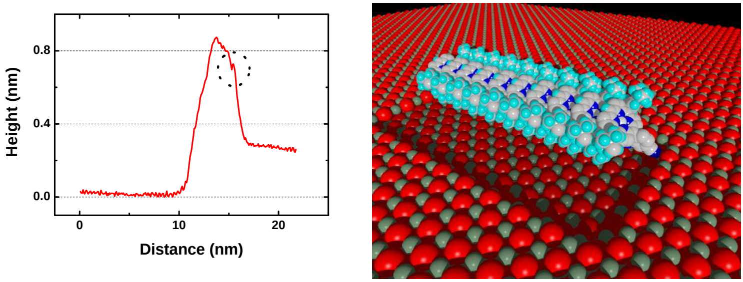

(a) Cross- section over a molecular wire

(b) Possible arrangement

Figure 3.9: (3.9a) Cross sectional view of the image shown in figure 3.8b. The small peak right of the large molecule peak comes from the dark dots visible in the topographical image. (3.9b) Possible arrangement of the cyano- porphyrins along the pit edges. Br^--ions in red, K^+-ions green. Rendered with PovRay [99].

at the step edges seems to be the crucial factor for immobilizing the molecules on place.

As already mentioned, the molecules only aggregate at the straight step edges. This can be explained by considering the relatively weak interaction of the stacking. A round edge bends the wire structure and enlarges the intermolecular distance reducing the interaction even more, which might lead to a breaking of the wire. This also leads to the conclusion that even though the wire is not completely interrupted at kink sites, the $\pi - \pi$ bond must become very weak or even completely interrupted.

3.5.2 Single Wires along Step Edges

Cleavage of a KBr crystal in UHV often leads to large terraces and long ($> 1\ \mu m$) step edges of different heights. Fig. 3.10a shows a $500 \times 500\ nm$ image of an in-situ cleaved KBr(001) surface. The step edges extend over the whole scan range of the microscope and they are flawlessly shaped, showing no defects or adsorbates. It is also remarkable that most of the step edges are oriented in the same direction, namely the [010] one on this area of the sample. The two marked step edges running in the [100]-direction have a length of more than 5 μm estimated from scanning several subsequent images to the right. This well defined surface promised to be an ideal template to produce long, one- dimensional structures along step edges.

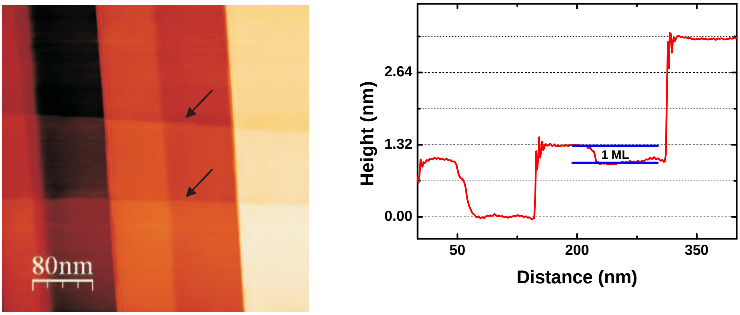

(a) UHV- cleaved KBr surface

(b) Cross section

Figure 3.10: (3.10a): Topography of a KBr surface cleaved in UHV and heated to 150°C for 20 minutes to get rid of surface charges The arrows mark the step edges parallel to the fast scan direction. Frame edge 500 nm, $f_0 = 170991\ Hz$, $Q = 15000$, $\Delta f = -5\ Hz$, $A = 20\ nm$. (3.10b): Linecut along a horizontal line. The step edges have various heigths between one and seven monolayers .

The evaporation of the molecules was similar to past experiments on irradiated KBr. Typical parameters were: $T_{sample} = 80°C$, $T_{molecules} = 160°C$, $t_{evap} = 60\ s$, $rate_{evap} \approx 1\ Å/min$. After the evaporation procedure the heating of the sample was immediately switched off and the crystal was allowed to cool down to room temperature again.

The resulting growth of the monocyanoporphyrins typically obtained along the step edges is shown in fig. 3.11. Decorations on all steps have been observed although the shape and arrangement of the decorations seems to be directly dependent of the step height. Closer analysis reveals that only steps with a height of $\leq$ two ML[*] ($= 0.66\ nm$) show the expected one-dimensional growth (fig. 3.11(1)) already observed on irradiated KBr. Higher steps are decorated as well, but the agglomerates reveal no uniform structure nor a constant height (fig. 3.11(2)) which leads to the conclusion that the molecules are not arranged as proposed in fig. 3.9b. A simple reason for this behaviour seems to be a basic geometric observation. Looking at various images the wires seem to overlap with the upper terrace, meaning that one side-group sits over the upper

---

[*] ML:Monolayer

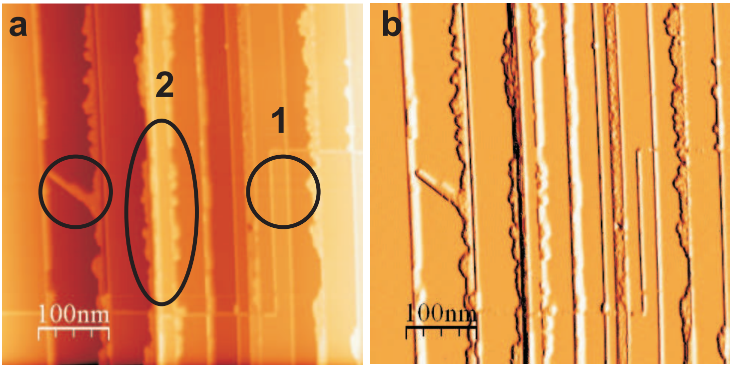

Figure 3.11: Topography (a) and Δf (b) image of the one dimensional structures along the step edges with monowires(1), unordered agglomerates(2) and multiwires(3). A detailed analysis is found in the text. Scan range $= 500\ nm$, $A = 20\ nm$, $\Delta = -8\ Hz$.

terrace. Structure (fig. 3.11(3)) will be discussed extensively in the next section.

Measuring the height of the molecular wires yielded to an interesting result. One dimensional structures are about $1.2-1.3\ nm$ high when assembled at a double step. Assuming that the molecule height is roughly $1.5\ nm$ [†], this would lead to a tilt angle of roughly $57 \pm 5°$ with respect to the substrate assuming the molecules are not laterally tilted. The structures along single steps and inside the pits are only $0.8 - 0.9\ nm$ high, which clearly indicates a different tilt angle towards the substrate. In this case, the angle would be $35 \pm 5°$. Balaban *et al.* showed in [101] that the distance between two molecules in the $\pi - \pi$ plane is roughly 3.6 Å which leads to distance of 5.9 Å parallel to the surface for a tilt angle of 37 $\circ$ between porphyrin core and the $\pi - \pi$ direction. This angle is observed in crystallographic assemblies of those molecules and can be assumed as more or less rigid value. Under these circumstances the calculated angle for a doublestep is probably wrong and a tilt in a second direction has to be responsible for the increased structure height at double steps.

Fig. 3.12 shows possible arrangements of the one-dimensional structures at step edges of different heights. The arrangement along a single (b) and double (c) step is directly derived from the angle calculated

---

[†] the calculated height would be 14.989 Å plus the Van der Waals radii of one hydrogen and one nitrogen atom.

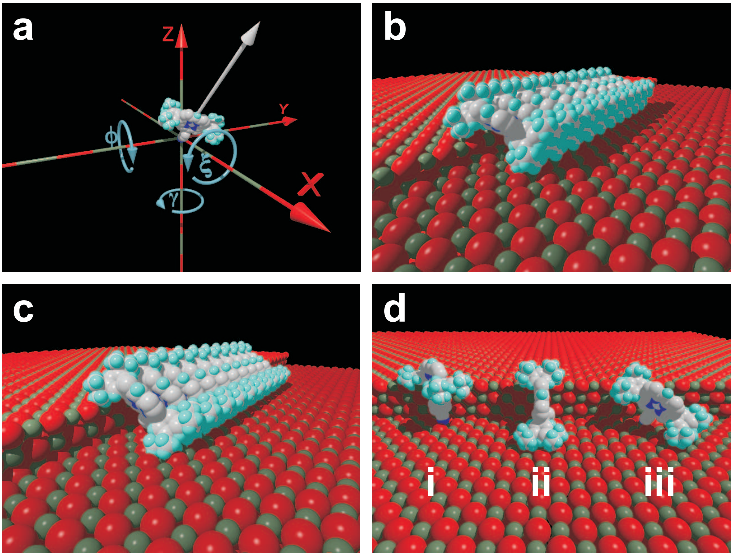

Figure 3.12: The angles used to visualize the arrangements are shown in (a). The rotation axis pass through the nitrogen atom. The KBr(001) surface is parallel to the X-Y-axis. The grey arrow marks the axis of the molecule. ξ is the tilt of the molecule with respect to the X-axis, ϕ the one to the Y-axis and γ to the Z-axis. The arrangement estimated from the height profiles along a single step is shown in (b). ϕ is 37°, ξ is 75°and γ is 0°. Along the doublestep shown in (c) ϕ increases sligthly to 43°. Again γ is 0°but the lateral tilt of the molecule ξ is now 60°. Along a triple step, one- dimensional wires were never observed. (d) Shows three different orientations of molecules at those edges. The most left molecule (i) in (d) is turned by $\gamma = 45°$ so that the core is oriented along the [110] direction. This orientation does not allow $\pi - \pi$ stacking along the direction of the step edges. The molecule in the middle (ii) is tilted by $\xi = 45°$ to the surface, making it fit geometrically to the step. (iii) Combines those two angles and could be considered as possible arrangement for the growth in the $\langle 110 \rangle$ direction.

above. The rotation angle ξ is based on stability reasons to give the wire a more rigid structure. In addition it explaines the increased height at higher steps. The assumption that the molecules are arranged in this way is supported by the fact, that we never succeeded to flip the wire to another position. The only possible manipulation was the partial or complete removal of a structure but never the alteration of its position. The arrangement along triple steps remains unclear so far. While we never observed a single structure along those edges, broader and higher agglomerates have been observed. We assume that different growth versions are possible. Three of them are presented in Fig. 3.12(d). Molecule (i) is rotated towards the terrace, allowing $\pi - \pi$ interactions along the $\langle 110 \rangle$ direction, but not along the step edge. Molecule (ii) is fitting nicely to the step and it is likely that agglomerates based on this orientation form the bigger structures we observed. The tilt of 45°also increases the apparent height of the structure to roughly 1.8 nm which explaines the higher values we observe along higher steps. However, this arrangement does not allow $\pi - \pi$ stacking along the crystallographic direction, since the angle between the porphyrin cores and the stacking direction would be 90°. The molecule (iii) is again tilted by $\xi = 45°$ and additionally turned by $\gamma = 45°$ which could be a starting point for structures growing across terraces, rather than along step edges.

3.5.3 Multiple Wires across Terraces

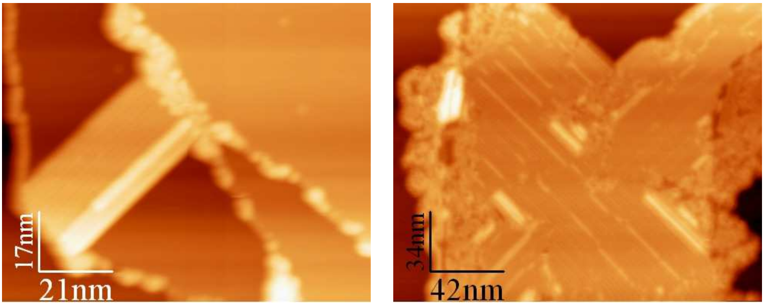

(a) Multistructure across a terrace

(b) Crossing multiwires

Figure 3.13: (3.13a):Multistructure growing across a terrace from step edge to step edge. The lower edge of the wire is higher than the upper part.The upper part is referred as monolayer. $f_0 = 174054\ Hz$, $Q \approx 15000$, $\Delta f = -8\ Hz$, $A = 10\ nm$. (3.13b): Crossing multistructures. The wires are oriented in the $\langle 110 \rangle$-directions. $f_0 = 173886\ Hz$, $Q \approx 15000$, $\Delta f = -52\ Hz$, $A = 5\ nm$

As already visible in fig. 3.11(3) and shown more clearly in fig. 3.13, we do not only observe single structures along step edges but also ordered structures across terraces. The number of these structures is directly dependent on the evaporated amount of molecules. While at low coverages (< 0.5 ML) the porphyrins tend to only decorate step edges, the amount of ordered wires on terraces increases dramatically at a coverage of more than 1 ML. In the first line, steps higher than three monolayers act as starting point for those structures. The porphyrins do not form oriented single structures along those higher steps, but rather clusters of unresolvable order from which the highly oriented structures arise.

To obtain large terraces with long straight step edges on KBr, the crystal is usually cleaved in UHV and heated to $150°C$ without further treatment. As an alternative, it is also possible to anneal the crystal up to $380°C$, allowing the surface to heal out kink sites and to form evaporation spirals at the intersection of dislocations with the surface [102]. Evaporation of monocyanoporphyrins on those surfaces at higher coverage led to an increase of both, the number and size of the multiwires in $\langle 110 \rangle$-direction. At the same time the single structures along the straight edges were overgrown by additional molecules.

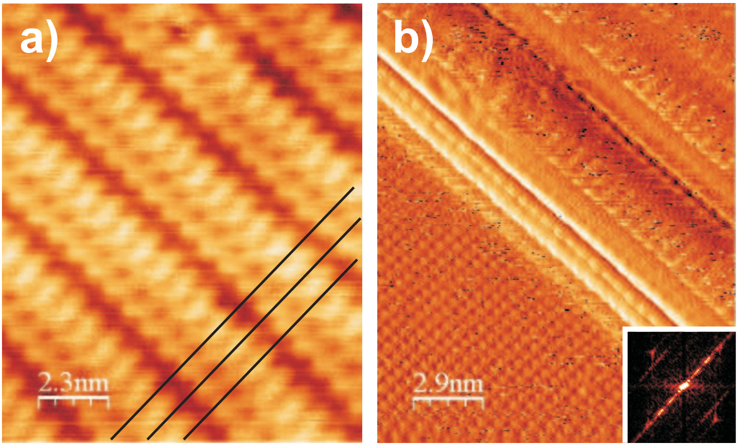

Figure 3.14: (a) High resolution nc-AFM image of a molecular monolayer consisting of several parallel porphyrin wires showing submolecular resolution. The intermolecular distance of the molecules can only be explained by a $\pi - \pi$ stacking of the molecules. (b) Atomic and molecular resolution image of the porphyrin wires and the KBr substrate. A Fourieranalysis (inset) reveals different periodicities for the molecules and the substrate. The contrast was enhanced by adding the derivative to the image.

Fig. 3.14 shows high-resolution nc-AFM images of parallel molecular wires along the [110]-direction separated in width by $2.4 \pm 0.2\ nm$, which corresponds to approximately five lattice spacings of the substrate perpendicular to the stack axes. The molecular rows are shifted against each other in order to optimize a compact arrangement. In Fig 3.14(b) the atomic structure of the substrate and molecular structure of the porphyrins are resolved simultaneously. A FFT-analysis of this measurement reveals that, unlike at the step edges in [100]-direction, the molecule to molecule distance within a wire differs from the KBr lattice spacing. The molecule-molecule separation measures $0.56 \pm 0.01\ nm$, compared to the distance of $0.47\ nm$ between two K^+ ions along the $\langle 110 \rangle$-directions. This indicates that the dimensions of the molecule ask for a larger separation than the K^+ intervals would provide, rather corresponding to the spacings observed in the crystal lattice of Balaban *et al.* [101]. At the steps, along the [100]-direction, K^+ ions are alternating with Br- ions creating attractive and repulsive sites for the partially negative charged cyano-groups and therefore forcing them into position. Diagonally across the lattice, in $\langle 110 \rangle$-direction, the potassium ions are evidently closer together and not interrupted by bromine ions, presumably creating a slightly delocalized positive charge distribution. The stacks are directed along one dimension, but in contrast to the assemblies at the step edges, the single porphyrins are not located each directly above a potassium ion, but rather along the K^+ chain, keeping their thermodynamically preferred intermolecular spacing. The angle between the porphyrin planes and the stack axis is slightly enlarged $(43 - 45^\circ)$ compared with the crystal structure, once more presumably due to the cyanophenyl-group perpendicular to the porphyrin plane. From high resolution images (Fig. 3.14a), it can be concluded that stacks mostly lie inclined on the surface, with the cyano groups pointing downwards and the big sidegroups standing out more on one side. Heights between $1.5 - 2.0\ nm$ were measured for monolayers, depending on the tilt angle of the stacks respective to the surface. Fig. 3.15 shows a proposed stack arrangement in $\langle 110 \rangle$-directions from these geometrical considerations.

Pšencík et al. determined distances between different bacteriochlorophyll stacks of $2.1 - 3\ nm$ in natural chromosomes, the same order of magnitude as observed in our porphyrin stacks $(2.4 \pm 0.2\ nm)$ [103]. This suggests that these wires are suitable for a potential application as light harvesting devices in artificial photosynthesis systems on surfaces, which can transport energy via excitonic excitations over large distances. Such antennae systems are for example of potential interest for hybrid solar cells that could operate under low or moderate light conditions since the photon capture cross-section might be markedly increased and hence leading to higher efficiencies. Moreover, porphyrins span a broader wavelength range compared to silicon solar cells. Fur-

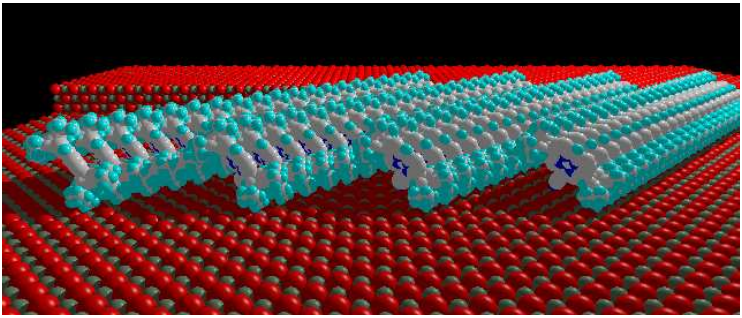

Figure 3.15: Visualization of the proposed molecular arrangement showing that the molecules are $\pi - \pi$ stacked and not lying flat on the surface. Furthermore, the stacks are inclined towards the surface and different tilt angles between the C2 axis of the molecule and the surface were observed, leading to heights of the monolayers from $1.5 - 2.0\ nm$.

thermore, porphyrins are known to be very promising building blocks; they are not only very stable, inexpensive and quickly accessible, but also both the periphery and the central metal are very easy to modify. Therefore, such porphyrin wires can be tuned with a high degree of freedom.

3.6 Monocyanoporphyrins on NaCl

Looking at the spacing of $0.56 \pm 0.01\ nm$ between the stacked molecules leads to the assumption that NaCl with a lattice constant of 5.65 Å is an ideal substrate to grow multiwires on. NaCl is chemically and physically similar to KBr and therefore prepared the same way. For those experiments we did not prepare irradiated surfaces but concentrated on simple cleaved substrates.

Fig. 3.16 shows the crystal after cleavage in UHV and subsequent annealing to $150°C$ in order to get rid of surface charges. It is remarkable, that the cleavage did not lead to steps in crystallographic direction but rather to a random distribution of orientations. However, the sample is very flat with large terraces and should therefore be a suitable template for multiwire growth. The evaporated amount of molecules is comparable to the previous experiments.

Fig. 3.17 shows an overview nc-AFM image of the molecular assemblies on NaCl(100). The step edges with no specific directions show no ordered molecular decorations. However, small rectangular pits and is-

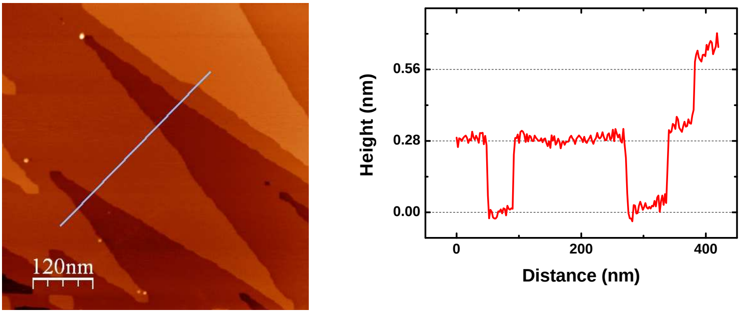

(a) UHV- cleaved NaCl **(b)** cross-section

Figure 3.16: In-situ cleaved NaCl(100) surface. The steps are not directed along the crystallographic axes and therefore probably not suitable to allow single wire growth along the step edges. The linesection shows the monoatomic height of the steps and the large dimensions of the terraces.$f_0 = 170992\ Hz$, $Q = 15136$, $A_{p-p} = 40\ nm$, $\Delta f = -5\ Hz$.

lands show the same single-wire decoration as the KBr(100) surface did. Additionally, we observe a large amount of broader structures growing across the terraces. The width of those structures is between 10 and 20 nm the height varies from $1.5 - 2.5\ nm$ and is therefore comparable to the heights of the ordered structures on KBr. The growth of the structures is initiated at a randomly orientated step edge or by a wire that has overgrown a kink site (circular mark in fig. 3.17).

Attemps to resolve the molecular structure of the broad wires were not successful and therefore it is not possible to extract the exact spacing between the molecules within the stacks. In contrast, several images clearly show the row structure, marked by arrows in fig. 3.17, which confirms the assumed similarities to the growth on KBr. The growth of the wires is most of the time only interrupted by step edges, meaning that no wire crosses such a barrier. In contrast to the assemblies along the step and pit edges on KBr the ones on NaCl have a width of $5-10\ nm$ and therefore consist multiple rows. A phenomenon that was not observed on KBr.

The biggest difference which was observed, is the tendency of the molecules to form crossing carpets or networks of wires at relatively low coverages. Fig. 3.18a shows such a network of several wire- junctions. The angle between the structures is 90°since all wires in this figure are oriented in the crystallographic directions. We also observe wires in the

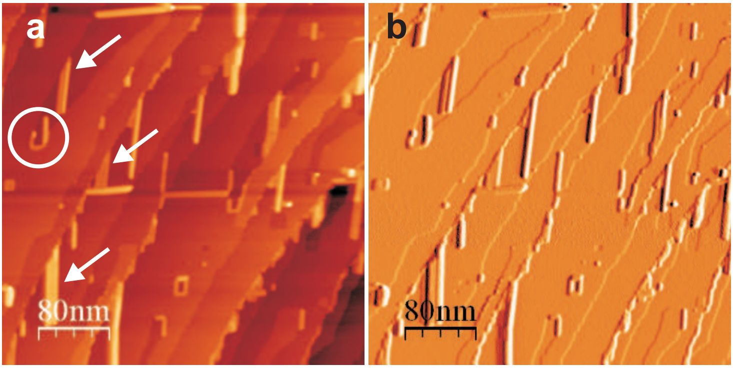

Figure 3.17: Topography (a) and frequency shift (b) of monocyanoporphyrin wires on a NaCl(100) surface. Only step edge parts in crystallographic directions are decorated. Multiwires grow across terraces in [100]- and [010]-directions. The parts where multiwires are visible are marked by arrows. $f_0 = 170992\ Hz$, $Q = 15136$, $A_{p-p} = 40\ nm$, $\Delta f = -9.5\ Hz$.

⟨110⟩-directions. Those structures do not differ in shape or thickness from the ones oriented in the crystallographic direction. The molecular assemblies have different heights and widths. Therefore, we can conclude that the adsorbtion angle between the molecules is not constant and that we possibly observe bi-layer structures.

Changeovers from thin-low wires to high-broad wires are shown in fig. 3.18a suggesting that the shape (width and height) of the wires is strongly dependent of the amount of material deposited on the substrate. The distance between single wires within one multiwire is roughly 1.6 nm and can therefore be assumed to be three lattice constants. This package is closer than on KBr but as shown in the next section the packing density does not influence the height in a noticeable amount. We also observe a depression in the middle of numerous wires running parallel to their orientation. This depression could be caused by a reversed tilt angle from one row to another as shown by the illustration in fig. 3.18b between the two middle rows. The molecules along the [100] are most certainly adsorbed at every sodium atom, leading to a intermolecular distance of 5.65 Å. According to different authors [101, 82], this distance is also valid in molecular crystallites, making the wires along the [100]-direction favourable. However, wires along the ⟨110⟩-directions can grow from kink sites or wire junctions.

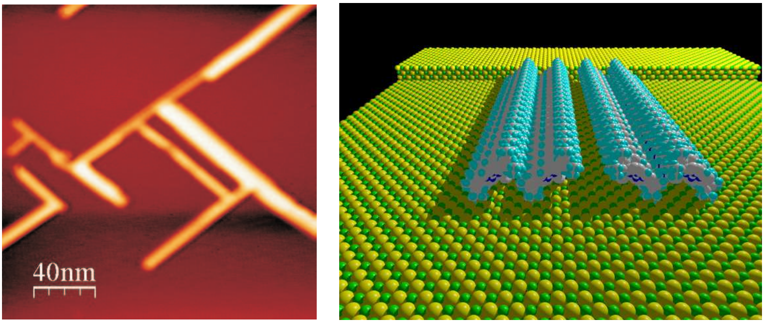

(a) Network structure on NaCl

(b) Illustration of the molecular arrangement within a wire on NaCl

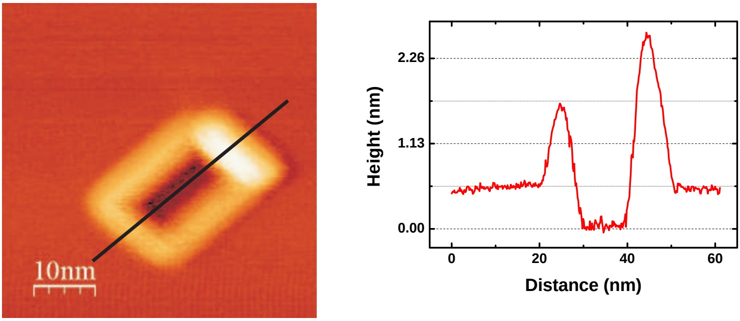

(c) Pit decoration

(d) Linescan over a decorated pit

Figure 3.18: Fig. (3.18a) shows a (200 × 200 nm) frame of a connected network of several wires oriented either in the [100]- or the [010]-direction. The scan angle is tilted by 45°to the crystallographic orientation. An illustration of the possible molecular arrangement in the multiwire is given in fig. 3.18b(Na^+-ions in green, Cl^--ions yellow). Fig. (3.18c) shows a decorated two-ML deep pit. The linescan in 3.18d reveals that the upper edge is decorated by a higher structure than the other three ones (1.7 nm compared to 2.5 nm with respect to the bottom of the pit). Scan parameters:$f_0 = 170992\ Hz$, $Q = 15136$, $A_{p-p} = 40\ nm$, $\Delta f = -11\ Hz$ (a) and $-18\ Hz$ (c).

3.6.1 Comparison between Structures on NaCl and KBr

Histograms of the height distribution of the molecular wires over several images were taken. The accumulated data is shown in fig. 3.19 and the

Peak Nr.	KBr [nm]	NaCl[nm]
1		1.15 ± 0.02
2	1.655 ± 0.001	1.71 ± 0.01
3	2.183 ± 0.005	2.26 ± 0.03

Table 3.1: Structure heights on NaCl and KBr. Data of the Gaussian fits in fig. 3.19. The erros of the gaussian fits are much smaller than the calibration errors (≈ 5%)

fitted data is summarized in table 3.1. All measurements were taken of wires growing on flat terraces without any steps in the analyzed display windows. The background peak of the histograms was brought to the zero position and the plots were recalibrated with the step edge heights obtained from the respective images. Finally, the diagrams were summed up, plotted and fitted by a Gaussian curve with a variable peak number.

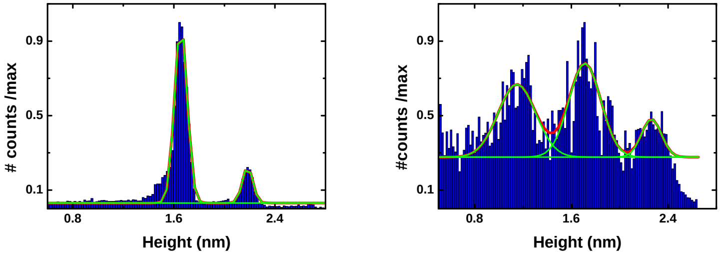

(a) Molecule heights on KBr

(b) Molecule heights on NaCl

Figure 3.19: Fig. (3.19a) shows a histogram of the two most common structure heights on KBr and fig. (3.19b) the three on NaCl. The positions of the peaks are listed in table 3.1.

The KBr histogram shows two clear peaks. The third plateau at ≈ 2.8 nm doesn't have a sufficient signal to noise ratio to be accurately extracted. The NaCl histogram shows the same peaks at ≈ 1.7 and ≈ 2.2 nm plus an additional peak at ≈ 1.15 nm. This peak has its origin from the wires that are growing as prolongation of the step-wires into the terrace. This height can be compared with the height of the single wires at step edges (KBr: ≈ 1.2 nm). The comparably poor peak quality of the NaCl measurements is caused by the relatively low molecular coverage and the thinner (≈ 10 nm) wires resulting in a huge contribution of the wire edges and hence in a relatively large background. The analysis of KBr was taken on broader ($\approx 100\ nm$) wires and therefore lowering the contribution of the wire edges to a negligible amount. This problem was partially overcome by increasing the amount of analyzed wires on NaCl reducing the fit errors down to $1 - 2\%$.

Comparing the fit parameters listed in tab 3.1 supports the assumption that the adsorption on NaCl is the same or at least very similar to the one on KBr. Since the histograms were taken on selected wires, it is important to notice that the heights of the peaks do not reflect the relative distribution of the structure-heights.

3.7 Multiple Wires on Gold-Decorated KBr

The previous chapters showed the possibility to form molecular wires along step edges and also across terraces. The next step on the road to molecular electronics is to contact those wires.

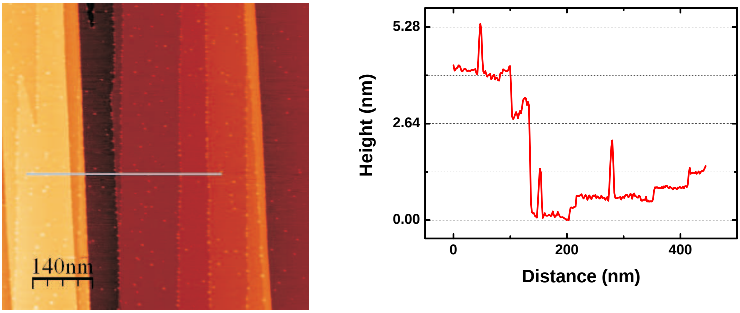

(a) Topography **(b)** Cross-section

Figure 3.20: Fig. (3.20a): Topography image of the Au-cluster decorated KBr surface. The crossection (3.20b) scan along the line, reveals a average clusterheight of $1.5\ nm$. Scan parameters $f_0 = 173013\ Hz$, $Q = 13500$, $A_{p-p} = 20\ nm$, $\Delta f = -5\ Hz$.

Evaporated gold forms small clusters on KBr with a visible diameter of $2-10\ nm$ and a height of roughly $1.5\ nm$ which is comparable to [104]. Deposition of submonolayer amounts of Au have been performed from a home- built evaporation cell. The flux was estimated by comparing the changes in pressure. The evaporation time was roughly 20 seconds at a pressure of $2 \times 10^{-9}\ mbar$ (normally $< 5 \times 10^{-10}\ mbar$) in the preparation chamber. The sample was held at room temperature to minimize the diffusion of the gold clusters.

A wide area of such a gold patterned area is shown in fig. 3.20. The clusters are distributed well over the surface with an increased density at step edges, which is a well known phenomenon on alkali halides [102, 105]. According to Pakarinen *et al.* [106] gold clusters are deposited by an atom-by-atom desorption. Gold atoms are adsorbed above and below step- edges and at anion vacancies[‡] in the surface and at step edges. The adsorption energies they obtained vary between 0.77 eV up to 3.70 eV.

Cluster at step-edges were observed on the upper terrace as well as on the lower one. Goryl *et al.* [107] claim that the majority of the clusters diffuse upwards on the higher terrace leading to a ratio of a 73:17:10 (upper:lower:undetermined) distribution. The observations done in our experiments do neither confirm nor disagree those results, since insufficient data statistics is available. Nearly all cluster at step edges are close enough to the edge itself, so that an influence of the step shape or potential was expected.

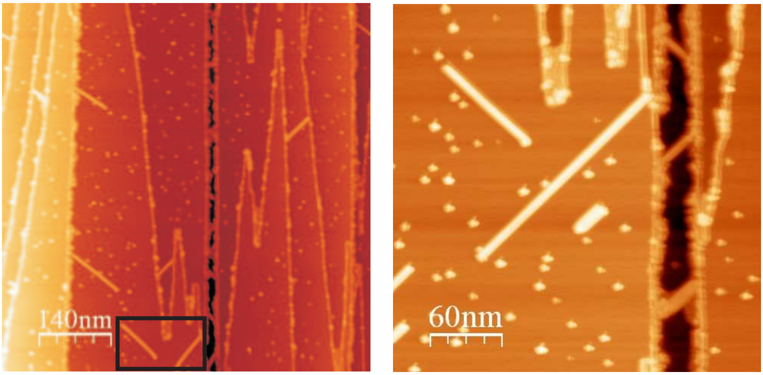

(a) Topographical overview **(b)** Zoom of the marked area

Figure 3.21: Topography images of monocyanoporphyrin wires on gold decorated KBr. Fig. (3.21a) shows a 700 × 700 nm scan with various wires along the $\langle 110 \rangle$- directions. Fig. (3.20b) gives a closer look at the bottom region of the left image marked by a black frame. Parameters for both images: $f_0 = 173013\ Hz$, $Q = 13500$, $A_{p-p} = 20\ nm$, $\Delta f = -5\ Hz$.

The evaporation of the monocyanoporphyrin molecules took place in an analogous manner as the previous evaporations ($T_{molecules} = 160°C$,

---

[‡] F-center F^0: vacancy with electron, F-center F^0_{gold}:F^0 filled with a gold atom

$T_{sample} = 80°C$, $t_{evap} = 60\ s$). Fig. 3.21 shows two topography images of the obtained decorated surface. Fig. 3.21a in particular shows numerous multiwires along the $\langle 110 \rangle$-directions growing from step edges as we already obtained on clean KBr surfaces. Various multiwires on the substrate seem to be terminated by a gold cluster. However, the various image channels do not lead to a final conclusion. In the middle lower part of the image, we also observe a free standing wire which is not touching a step at all. Fig. 3.21b shows this structure at an enlarged scale. Taking a careful look at the lower right end of the wire it becomes obvious that it ends in a gold cluster as the shape is clearly different from the rest of the structure. Yet, it remains unclear if the top left end of the wire is terminated by a cluster aswell. The rounded shape of the wire, aswell as the faint shadow indicate a gold agglomerate here aswell.

The gold clusters on fig. 3.21b have a visible diameter of $8 - 12\ nm$ and an average height of $1 - 1.5\ nm$. They share several distinct features in their appearance, leading to the conclusion that rather the tip-shape than the cluster is imaged here [104]. Therefore, the real size of the clusters can assumed to be smaller than visible on the images and it also is not possible to extract the exact size of the Au- clusters due to unknown tip size. Barth *et al.* suggest [104] that the gold clusters have a different charge than the surface, which is preventing high resolution on the clusters. Our KPFM- setup with dynamic CPD compensation is a first step in order to obtain high resolution on the clusters and the surface at the same time. In addition to the dynamic compensation of surface potential differences, the tip shape and especially the tip apex builds the crucial criteria for the image quality.

A closer look on the gold-wire-gold structure is shown in Fig. 3.22. The topography image 3.22a shows several gold cluster distributed randomly on the surface. The gold cluster attached to the lower end exhibits a slightly larger diameter than the wire itself. The cluster at the upper end seems to have a reduced height and is also significantly smaller than the average cluster size. The influence of the tip convolution with the structures, the small dot respectively faint line above the agglomerates, is more visible on higher clusters and the molecular wire. The wire contains several rows and despite the uppermost one, all seem to be attached to both clusters. The mentioned row seems only to grow from the lower cluster to stop then briefly before the structure joins the second gold-agglomerate. The Δf image 3.22b reveals some more details about the gold molecular interface. The lower crossing is hereby much smoother than the upper one which can be based on the comparable height of the two strucures or the tilt angle of the molecules being directed to the lower right side.

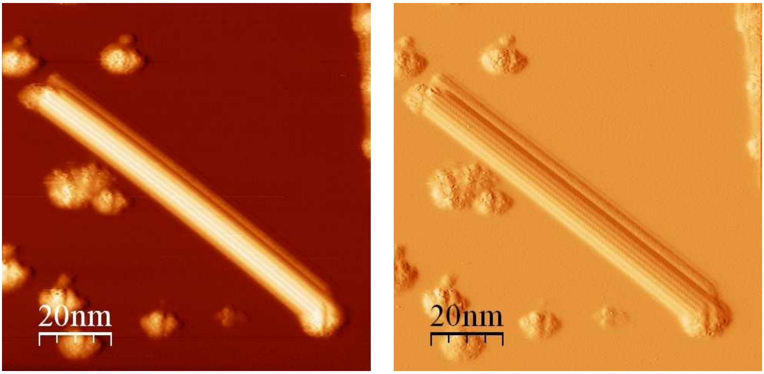

(a) Topography **(b)** Frequency shift

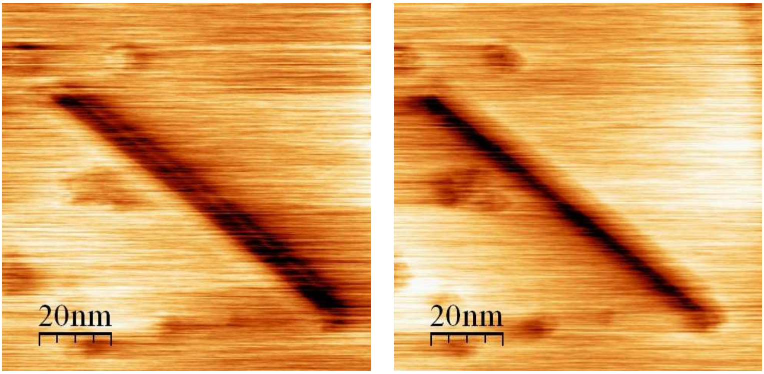

(c) CPD (forward scan) **(d)** CPD (backward scan)

Figure 3.22: Topography (a), Δf (b) and CPD (c,d) images of the multiwire formed between two gold clusters. Scan parameters: $f_0 = 173013\ Hz$, $f_1 = 173013\ Hz$, $V_{ac} = 0.5\ V$, $Q = 13500$, $A_{p-p} = 20\ nm$, $\Delta f = -11\ Hz$, voltage range in (c,d): $360 \pm 65\ mV$. For contrast enhancement the derivative of the topography was added to (a). Images (c & d) reveal also that the KPFM controller was set too slow which results in a blurry contrast on the right/left side of the structure.

The CPD image reveals a distinction between clusters, molecules and the underlying substrate. The molecular wire as well as the goldcluster show an increase of the contact potential difference. Additionally, the compensation proved to be really difficult on insulation substrates and various changes in the electrical structure of the tip caused the contact potential to be unstable. Those facts led to the result that the interconnected clusters could not be resolved anymore by means of KPFM measurements yet.

With the results, we obtained a first possible contacting of the molecular wires and although this is not a real electrical contact yet it indicates a possible way to measure conductances. One way could be to contact the gold clusters with a forked tip including two contacts. Another way is KPFM on thin films, which is more extensively done in the next chapter.

3.8 Conclusions

In the past years, many attempts to observe molecular self assembly on insulating surfaces have been performed. It has been discovered that the high mobility of organic molecules on non-metallic surfaces can be lowered by inducing radiation defects. The electrostatic surface potential of ionic crystals is highly enhanced at step and corner sites and therefore, is an ideal anchor point for highly polar molecules. In this chapter, it has been shown that polar molecules show a significantly larger tendency to self-assemble on alkali-halides than unpolar ones. It has also been shown that monocyanoporphyrin molecules do not adsorb parallel to the surface, but rather stand more upright binding with their polar legs to the substrate. The monocyanoporphyrins further maintain their $\pi - \pi$ stacking on the surface. It has also been shown that those molecules maintain their crystallographic distance across terraces where the $\langle 110 \rangle$-directions have a reduced corrugation of the potential. Along step edges, where this potential is significantly more corrugated, the molecules adapt their spacing to match the underlying substrate. The mechanism which starts the growth across the terraces is not yet fully understood. Most probably the higher steps force the molecules into a position which favours growth across terraces.

At last, it has been proven that molecular wire growth also takes place from and to deposited gold nanoclusters. It can be imagined that growth between two clusters can be used as a contacting prototype, providing possibilities to study molecular conductance.

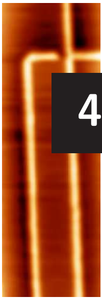

4 Porphyrin Molecules on Thin Insulating Films

The investigation of optoelectronic or electronic properties of molecular arrangements has proven to be difficult on bulk insulators. Local charge variations and the material often hamper the capability to compensate the contact potential difference. Thin salt layers on metal substrates provide an electrically decoupled surface which additionally allows the application of KPFM measurements.

In STM studies, salt layers are often used to electrically decouple the molecules from the metallic substrate. The overlap of the orbitals with the metal becomes negligible and therefore the STM becomes capable to image HOMO[*] and LUMO[†] states of the molecule by tuning the bias voltage [108]. The application of KPFM on the other hand can provide further informations and is also applicable on thicker films ($\gtrsim 1\ nm$).

4.1 Growth of Ultrathin Salt Films on Metals

Ultrathin films of NaCl and KBr were grown on Cu(111). While experiments on KBr thin films are not so common [109], NaCl thin films are well studied [110, 111, 112] and often used as templates for organic molecules [85, 113]. In most cases reported, NaCl and KBr growth are achieved by means of practical and simple techniques. Both alkali halides reach comparably high vapour pressures at quite low temperatures (i.e. $10^{-4}\ mbar$ at about $800\ K$ for NaCl). Therefore, they can easily be sublimed at a relatively low temperatures of about $650\ K$. Upon sublimation of NaCl and KBr dimers are formed, thus guaranteeing the conservation of the stochiometry in the film growth [114, 115, 116].

---

[*] Highest occupied molecular orbital

[†] Lowest unoccupied molecular orbital

The growth of the salt layer is barely influenced by the copper surface. The salt grows in the same rectangular structure as in its crystallographic form. The underlying surface however influences the growth direction, leading to three different orientations of the salt islands shown in fig. 4.1.

Another interesting feature is the so called *carpet growth*. The lattice constant is stretched over several periods in order to allow the layer to grow over adjacent terraces of the substrate. Furthermore those areas seem to be a preferencial starting point for the second layer islands to grow. This second layer is usually built by several small islands which tend to have a rectangular shape in order to minimize their energy.

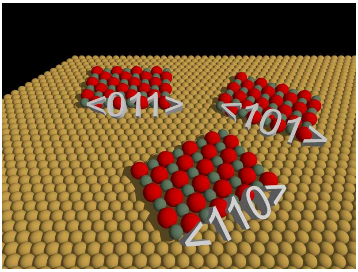

Figure 4.1: POV-Ray [99] visualization of the three growth orientations of salt islands.

Concerning the growth, it is interesting to note that several authors report that the first NaCl layer is always a double layer. This has been reported for different substrates such as Ge(001) [117, 118], Al(111) [119] and Cu(111) [120, 121]. However, the discrimination is not trivial and our measurements lead to the conclusion that the first NaCl layer is a double layer while the first KBr layer seems to be a single one.

The investigation of the structural properties described above has been pursued with different experimental techniques. A lot of studies have been carried out with LEED to gain information about the orientation of the NaCl lattice with respect to the underlying surface [117, 122, 123, 110]. Scanning probe microscopy, namely STM [118, 119, 120] and AFM [111, 112] proved to be useful to improve the understanding on these salt structures.

In our experiments we used a Cu(111) surface. The substrate is a single crystal (Mateck GmbH- Jülich, Germany) cut along the specific crystallographic direction and polished with an accuracy of $< 0.4°$. The crystal was prepared *in situ* according to common surface science techniques by several cycles of Ar^+ bombardment[‡] and subsequent annealing to $520°C$. Between two experiments the sample was cleaned by two Ar^+ sputtering- annealing cycles using the parameters specified in table 2.2.

The above described treatment results in atomically flat and clean substrates. The quality of the surface has periodically been checked

---

[‡] sputtering

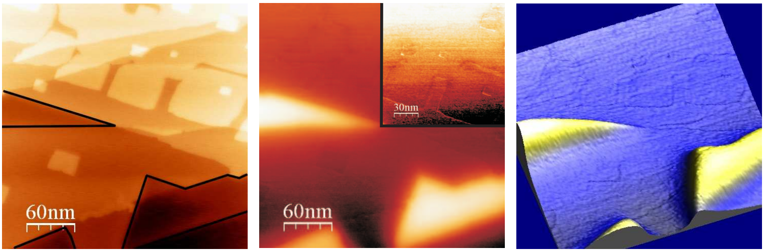

(a) NaCl on Cu(111) topography…

(b) …and CPD image

(c) 3d-view of the CPD

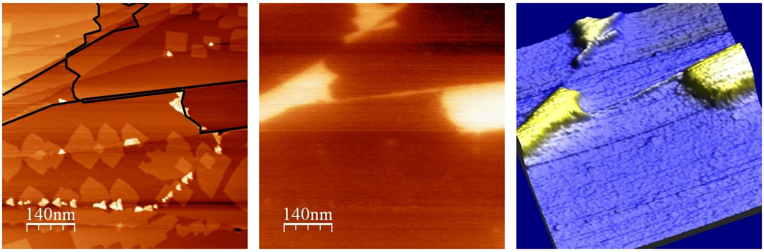

(d) KBr on Cu(111) topography…

(e) …and CPD image

(f) 3d-view of the CPD

Figure 4.2: Ultrathin NaCl layers on Cu(111) shown as topographical (4.2a) and CPD (4.2b,4.2c) image (300 × 300 nm). The borders between bare Cu and NaCl are marked by black lines. The inset in fig. 4.2b shows the contrast between different salt layers. Scan parameters $f_0 = 161105\ Hz$, $f_1 = 1004810\ Hz$, $Q_0 = 12000$, $A_{p-p} = 20\ nm$, $V_{ac} = 0.5\ V$, $\Delta\ f_0 = -26\ Hz$, $CDP_{NaCl-Cu} \approx 500mV$. The lower row shows the same type of images for KBr thin films (700 × 700nm). Again the borders between bare Cu and KBr are marked by black lines. Scan parameters $f_0 = 170496\ Hz$, $f_1 = 1054230\ Hz$, $Q_0 = 14500$, $A_{p-p} = 20\text{nm}$, $V_{ac} = 0.5\ V$, $\Delta f_0 = -7\ Hz$, $CDP_{KBr-Cu} \approx 400\ mV$.

by means of AFM, AES and LEED. AFM images show atomically flat terraces with a typical size of about hundred nanometers. Nearly no contamination was visible over a large scale on the crystal. Due to the difficulty to resolve the crystal structure with atomic resolution by means of AFM the periodicity was checked with LEED which showed a well defined pattern. LEED also proved, that the substrate was formed by a single crystallographic domain. AES measurements were used to

	T_{evap} $[^\circ C]$	T_{subs} $[^\circ C]$	t_{evap} $[min]$	$rate$ $[\text{Å}/min]$
NaCl	340	80	20	0.2
KBr	340	80	20	0.2
Molecules	160	80	1	10

Table 4.1: Evaporation parameters

obtain qualitative contamination information.

NaCl or KBr have been deposited on the clean metallic substrates by sublimation, using the three-cell evaporator with temperature controller described in chapter 2. As a source material, crushed salt powder obtained from alkali- halide single crystals has been used. All evaporation parameters are listed in table 4.1. Although the 3-cell evaporator is supposed to be built symmetrically, evaporation temperatures for the same rate are not constant for different cells. It is estimated that the error in temperature measurements is around ±5%. However, subsequent evaporations from the same cell proved to be of constant rate at constant temperature. In order to obtain thin layers of salts it proved to be successful choosing a very low evaporation rate of ≈ 0.2 $\text{Å}/min$. The sample temperature during the evaporation was kept constant at $80^\circ C$.

The investigation of the obtained ultrathin salt layers has been carried out exclusively by AM-KPFM. Typical results obtained are shown in fig. 4.2. An especially nice feature of the KPFM measurements is the contrast between clean metal substrate and the salt layers on it. While the step edges on the salt produce almost no contrast in the CPD image at all, the Cu- salt step is clearly visible. From these images (and the damping contrast described in chapter 2) it can be concluded that indeed this surface is composed by two different materials. Based on the comparison of the island shapes with literature [118, 119, 120, 111, 112] it can be concluded that the islands are formed by alkali halides. Whether it is KBr or NaCl, cannot be determined by the island shapes but rather by the step heights from the first to the second or the second to the third layer. Height measurements of the fist NaCl layer step tendencially confirmed the statement that it's always a double layer height. However, the measured heights varied from $4 - 5$ Å, which does not give absolute confirmation. In contrast, the first layer step on KBr was measured $3 - 4$ Å leading to the conclusion that the first KBr layer is a monolayer.

Another remarkable observation should be mentioned here. In fig. 4.2d higher triangular or trapezoidal shaped structures are visible. Observations of similar structures formed by NaCl on Al(111) by Hebenstreit *et al.* [124] and for NaCl on Cu(111) by Ramoino [114] have been reported. Hebenstreit *et al.* explain their observations with the formation of a polar (111) surface which contradicts stochiometric growth described above. They suggest a three layer system (Na-Cl-Na) terminated like the NaCl(111) surface. This model relies on the non-equilibrated stochiometry between Na and Cl, namely an excess of Na on the Al(111) surface. They obtained their structures by depositing Na on Al(111), while dosing the surface with Cl_2.

The formation of a KBr(111) surface on our samples seems a bit unlikely since the evaporation of the salt was made from bulk material with an equal amount of K+ and Br^- ions. Ramoino pointed out that LEED induced color centers could act as desorption sites for chlorine and consequently also for bromine. However, no deposition experiments were done directly after LEED measurements and no alternative reason for chlorine desorption could be identified. So far we haven't found any explanation how those structures were formed.

4.2 Dipole Fields of Molecular Assemblies

The monocyanoporphyrin molecules used in this work exhibit a strong dipole caused by the cyano-phenyl group attached on one side. KPFM images the dipole fields, build by the molecules. The molecular structures have a finite extension on the surface and therefore, they are suspected to show a strong distance dependance of their field. This section gives a simple consideration about the qualitative informations one can gain from KPFM on molecular assemblies.

A dipole close to a surface and oriented perpendicular to it induces a local change in the electrostatic potential of the substrate. The potential of a single dipole is given by [125]

$$\Phi(\vec{r}) = \frac{\vec{p}}{4\pi\epsilon_0} \frac{\vec{r}}{r^3}, \tag{4.1}$$

where $\vec{p}$ is the dipole moment and $\vec{r}$ describes a point far away compared to the dipole length. The electric field on the axis of a circular disc with radius R is given by [125]

$$E(x) = \frac{1}{2\epsilon_0}\sigma\left(1 - \frac{x}{\sqrt{x^2 + R^2}}\right), \tag{4.2}$$

with the corresponding potential of

$$\Phi(x) = \int_l E \cdot dl = \frac{\sigma}{2\epsilon_0}\left[\left(x^2 + R^2\right)^{1/2} - x\right]. \tag{4.3}$$

Fig. 4.3a shows the electrostatic potential in function of the distance for a single dipole, two circular discs of opposite charge with

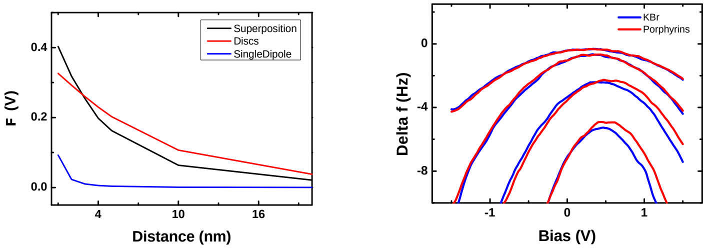

(a) Electrostatic potentials **(b)** Bias - Δf curves

Figure 4.3: (4.3a): Three numerically calculated potentials in function of the distance. Calculation parameters: dipole moment $\vec{p} = 4.37\ D$, disc radius $r = 10\ nm$, separation $d = 1\ nm$. (4.3b): Measured bias - Δf curves for different tip-sample distances. Separations from bottom to top: $1, 5, 10, 20\ nm$.

$r = 10\ nm$ separated by $d \approx 1\ nm$ and numerical calculated and superimposed dipole fields. For the interpolation curve an averaging distance of $r_{int} = 4nm$ in a square form was assumed. As a first approximation the single dipole and the interpolated layer were assumed to be standing perpendicular to the surface, which lead to higher numeric values than for the disc substraction. Assuming a tilt angle of roughly 45°leads to a smaller contribution. The dipoles in fig. 4.3a are all calculated with $\theta = \pi/4$. It turns out that the potential Φ at a distance of 1 nm is roughly $300 - 400\ mV$. As already mentioned, eq. 4.1 is only valid for places x with $|\vec{r}(x)| << d$, where d is the distance between σ^+ and σ^- within the dipole and $|\vec{r}(x)|$ the distance from x to the dipole center. This is one explanation why the resulting potential of the dipole superposition shown in fig. 4.3a is larger than the potential for the discs.

The measured contrast between molecular islands and the KBr substrate is only in the regime of $60 - 80\ mV$ at the same separation. In order to reconcile those two values one has to consider that the cantilever is oscillating and therefore the mean sample- tip distance is $d = 1\ nm + A_{osc}$. The electrostatic potential felt by the tip therefore is an averaging over $\Phi(1nm) - \Phi(2A_{osc} + 1\ nm)$.

Another observation made in the measurements is, that the contribution of the molecular islands becomes negligible small at larger distances ($\gtrsim 20\ nm$) which is explained by the formulaes. As shown in fig. 4.3a one way to calculate the potential of a finite layer of dipoles is to assume two parallel discs separated by the dipole distance d with a charge density of σ in $[C/m^2]$. The resulting potential as a function of a point in space $\vec{x}$ then is given by the sum of the two potentials of the discs:

$$\Phi(x) = \frac{1}{4\pi\epsilon_0}\int_S \frac{\sigma}{|\vec{x}-\vec{x'}|}da' - \frac{1}{4\pi\epsilon_0}\int_S \frac{\sigma}{|\vec{x}-\vec{x'}+\vec{n}d|}da''. \tag{4.4}$$

In contrast to that, the potential of an infinite charged plane oriented in the $y-z$ plane as a function of x is given by

$$\Phi(x) = \frac{\sigma}{2\epsilon_0}x. \tag{4.5}$$

Comparing equations 4.4 and 4.5 with each other reveals a much faster decay of the dipole layer potential, which is in agreement with the experimental data.

Fig. 4.4a shows calculated electrostatic potentials across a molecular wire. The wire width was assumed to be 5 nm, with the corresponding charge distribution σ. The curves were calculated with a superposition of equation 4.1 at every point. The obtained curves show a strong distance dependence in the strength of the potential. It therefore can be concluded, that at a certain tip- sample distance, the contrast in the CPD-image produced by the molecular wire becomes too small in order to produce a reasonable signal to noise ratio.

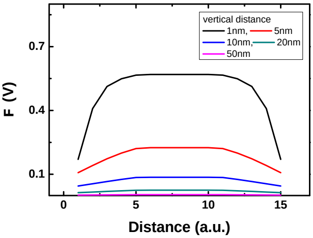

(a) Potentials over a wire

Figure 4.4: Simulated electrostatic potential curves across a 5 nm broad wire (from position 6-10 on the x-axis) for different vertical distances. The curves were calculated with the superposition method [125] as described in the text.

4.3 Monocyanoporphyrins on Ultrathin KBr-Films

Porphyrin molecules shown in fig. 3.7 were deposited on ultrathin KBr films on Cu(111) (evaporation parameters listed in table 4.1). After deposition the sample was allowed to cool down to room temperature before starting the AFM measurements. During all measurements KPFM mode was switched on with the capacitive coupling compensation enagaged (c.f. chapter 1.3.4).

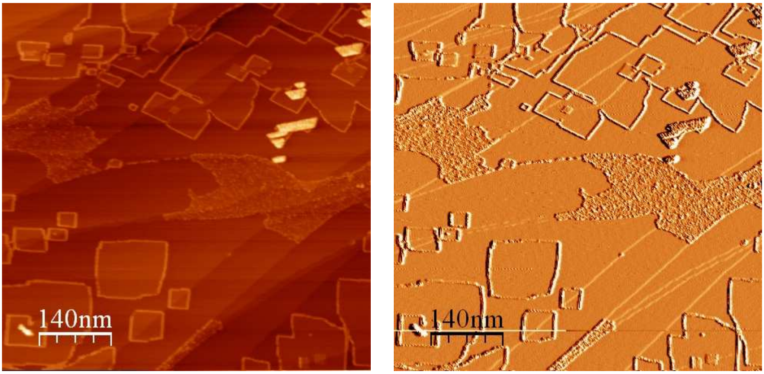

(a) KBr on Cu(111) topography. . .

(b) . . . and $\Delta\ f$ image

Figure 4.5: Topography (4.5a) and $\Delta\ f$ (4.5b) image of a ($700 \times 700\ nm$) scan. The molecules are decorating the KBr-island edges and are probably covering the rough Cu areas completely. $f_0 = 170496\ Hz$, $f_1 = 1054230\ Hz$, $Q_0 = 14500$, $A_{p-p} = 20\ nm$, $\Delta f_0 = -7\ Hz$.

Fig. 4.5 shows a topographical (4.5a) and Δf (4.5b) overview of the prepared surface. Different features can be noted. First the porphyrin molecules decorate the steps of the KBr islands. More precisely, the decoration is well ordered at step edges from the first to the second and from the second to the third layer. The decorated Cu-KBr steps however show no ordered structure. Having a look at the former pure Cu spots reveals a very rough surface, which is even better visible in the Δf image. At the first glance this seems surprising, since similar molecules tend to self organize on Cu(111) [126]. However, desorption of the molecules on Cu(111) and measuring at RT by STM didn't result in highly resolved images of self- organized layers but rather in very mobile agglomerates. In our observations, the arrangement on the Cu(111) was highly disordered but stable at a large scale. It is interesting to note that almost no molecules are visible on the flat KBr terraces. Interestingly, no multiwire structures are observed. On bulk material a low coverage of molecules usually leads to very few multistructures but on these samples we didn't observe a single one. It is expected that the molecules have a higher affinity to the metal surface than to the insulator and therefore agglomerate in higher layers on the copper. Furthermore, the molecules are not influenced by the Cu step edges under the KBr layers, where no agglomerates were observed along those edges. Having a careful look at the porphyrin agglomerates on pure Cu show no significant increase of the molecular concentration, as well leading to the conclusion that Cu steps do not act as adsorption site in the same way as KBr steps do.

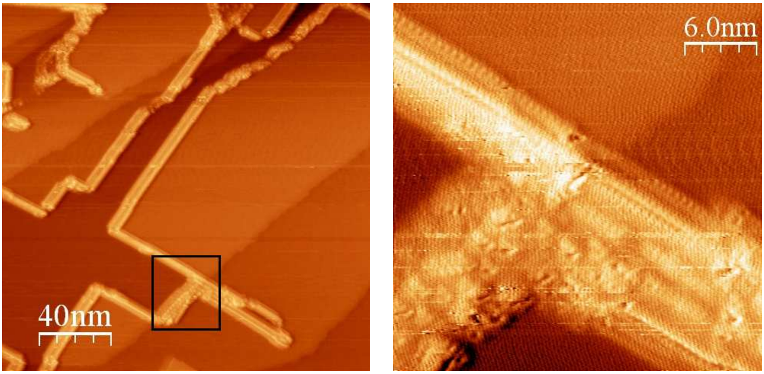

(a) 2- Phase structure **(b)** …more detailed

Figure 4.6: Topography (4.6a) image of a ($200 \times 200\ nm$) KBr thin film on Cu area featuring different phases of the molecular assembly. A closer look is shown in fig. 4.6b. $f_0 = 170496\ Hz$, $f_1 = 1054230\ Hz$, $Q = 14500$, $A_{p-p} = 20\ nm$, $\Delta f = -10$ and $-13\ Hz$. For contrast enhancement the derivative of the topography have been added to the pictures.

Fig. 4.6a shows an overview of an interesting section on the sample. The KBr step going from bottom- left to top-right is from the first to the second KBr layer. An interesting detail here is that the wire widths are significantly increased compared to pure KBr and as seen in fig. 4.6a, they are formed by a double row. The molecular resolution in fig. 4.6b reveals an even more fascinating detail. While the structure from bottom-right to top-left reduces from a four row wire to a double[§] wire, the structure joining from bottom-left shows a totally different alignment. The molecules show no order and have a round shape instead of the usual elongated ellipsoidal form. This difference was never observed on others than the first KBr layer. In addition, this structure was never observed on bulk KBr nor NaCl. This suggests that the copper substrate influences the growth of the molecular arrangement by a

---

[§] We only observe molecular details in the upper wire. Judging from the width ($\approx 8\ nm$) of the structure though, suggests that it is indeed a double wire.

non negligible amount, but only if Cu- and KBr-steps are close to each other. It is important to note that this additional molecular phase was only observed above Cu steps or more precisely they seem to be favoured by those underlying steps.

Fig. 4.7 shows a sequence of ultra high resolution images of an area with ordered molecules of this newly found arrangement. Fig. 4.7a is a $(200 \times 200\ nm)$ scan and shows some details of the region of interest. The structure is originated at an underlying Cu step and grows towards the lower image edge. It is then interrupted by a conventional wire along a KBr island. Fig. 4.7b shows a $(30 \times 30\ nm)$ topography image of the assembly, already revealing intramolecular details as well as atomic resolution of the underlying KBr. This image also shows the relatively weak binding energy of the molecules to the substrate: while changing the scan range and adjusting the position we already removed parts of the layer on the right upper side.

Fig. 4.7c-4.7f shows topography and Δf of two subsequent $(30 \times 30\ nm)$-scans. The first image is scanned downwards, the second one upwards. The first few lines of 4.7c were scanned with an increased frequency shift of $\Delta f = -11\ Hz$. After the removal of the first molecules, the setpoint was lowered to $-10\ Hz$ again. Regardless of that, the tip continued to remove molecules, thinning the structure to 50% of its original size. It is remarkable that even though the tip is removing molecules the scan remained absolutely stable and maintained the high resolution ability during all the performed manipulations.

4.3.1 Discussion about a Proposed Arrangement

The amount of removed molecules and the shape of the resulting structure suggest that the molecules arrange in a superstructure of about $6 - 8\ nm$ width. This superstructure is also visible in 4.7a where the area at the top of the image is covered by molecules arranged in this form. Initially three columns are growing downwards. While zooming in to a better resolution in fig. 4.7b the right column was partially removed. The residual molecules were swept away in the subsequent scans. The two columns growing to the lower step edge exhibited a slightly increased sticking behaviour, but as soon as a small damage in the left column was inflicted, this additional stability was lost and half this side was removed as well.

Suggesting an appropriate model of the molecular arrangement has proven to be difficult. Both columns visible in 4.7c- 4.7f show periodic and distinc features proving that they are real intramolecular features. The rows are inclined by $\approx 10°$ to the [010]- direction. The first attempt in extracting the molecular arrangment is to lay a lattice over the

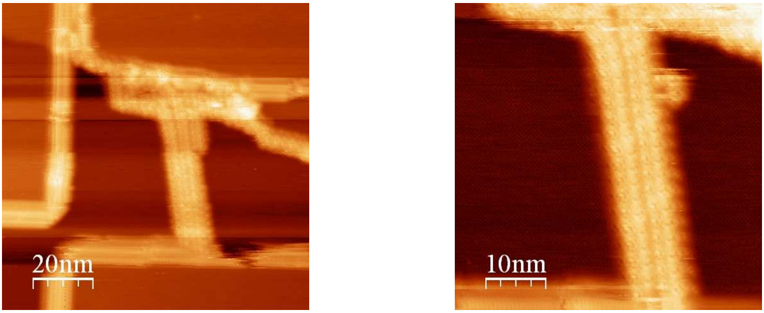

(a) Topo (100 × 100 *nm*) **(b)** Topo (50 × 50 *nm*)

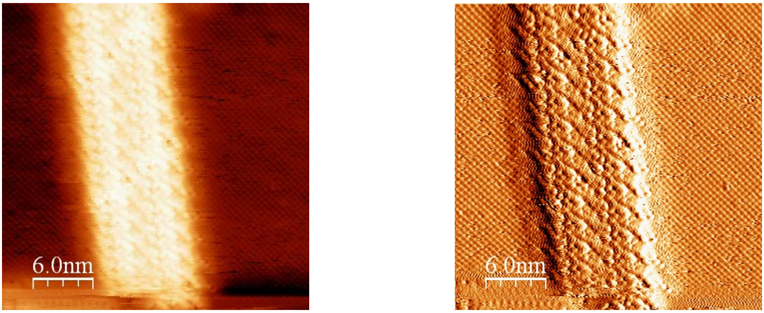

(c) Topo (30 × 30 *nm*) **(d)** $\varDelta\ f$ (30 × 30 *nm*)

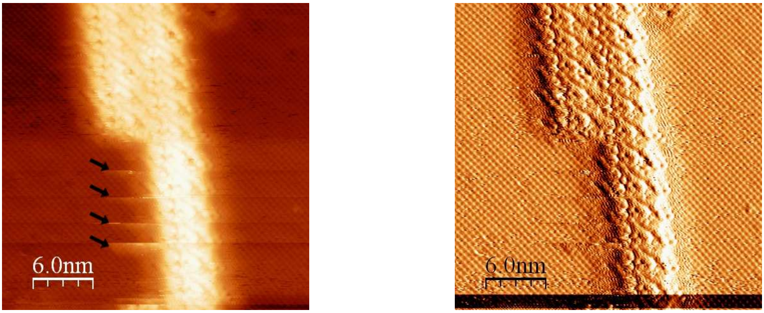

(e) Topo (30 × 30 *nm*) **(f)** $\varDelta\ f$ (30 × 30 *nm*)

Figure 4.7: Ultrahigh resolution images of a molecular structure grown on an ultrathin KBr layer on Cu(111). Scan parameters: $f_0 = 164731\ Hz$, $f_1 = 1026890\ Hz$, $Q_0 = 12000$, $A_{p-p} = 20\ nm$, $\varDelta f_0 = -8\ (a) - (d), -10\ (e), (f)\ Hz$. Detailed description in the text.

structure.

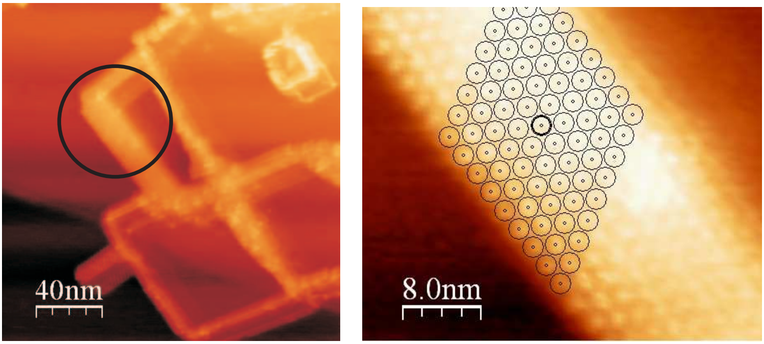

(a) Overview ($300 \times 300 nm$)...

(b) ...and zoom

Figure 4.8: Fig. 4.8a shows a large scale scan over an area with both, wirelike and carpetlike porphyrin structures. The marked area in the image is shown again in fig. 4.8b. Here, the structure is overlayed by a hexagonal lattice ($a = 2.3\ nm$). $f_0 = 164731\ Hz$, $f_1 = 1026890\ Hz$, $Q = 12000$, $A_{p-p} = 20\ nm$, $\Delta f = -17\ Hz$.

Extracted from fig. 4.7 propose a 4 × 3-lattice tilted 45° to the crystallographic directions of the KBr. The resulting unit cell then has a size of $1.4 \times 1.87\ nm$ which is slightly smaller than the molecular dimensions and therefore this model would lead to a overlap of molecules, a non trivial tilt or a non-filled lattice. Another possibility was derived from a different image shown in fig. 4.8. Despite the obvious double tip image, the nature of the structure marked by the circle is again similar to the one in fig. 4.7. The molecules seem circular and regularly distributed. Looking at the growth direction of the structure compared to the KBr island edge right of it, indicates the same tilt angle of roughly 10°. However, in this image we can overlay the carpet with a hexagonal lattice with a intermolecular distance of $2.25\ nm$, corresponding nicely to the porphyrin dimensions itself. This lattice would correspond to a 15° tilt angle with respect to the crystallographic directions of the KBr layer. This angle is sligthly higher than observed before but due to drift it is within the error estimation.

We further assume that the molecules lay rather flat on the surface because the whole structure is only $0.9 - 1.0\ nm$ high. Additionally, we expect the structure in 4.7c to be the same in both columns. As evidence, we point out the removal in fig. 4.7e which cuts off exactly one column.

However, the overlayed lattice is not evidently commensurate with the image, which does not allow us to directly determine the direction or the configuration the molecules are arranged.

4.4 Monocyanoporphyrins on Ultrathin NaCl-films

The same experiments as in the previous section were performed on NaCl thin films. The Cu(111) surface was prepared by several sputtering-annealing cycles before the deposition of NaCl according the parameters listed in table 4.1. After checking the coverage of the Cu surface by means of AFM, porphyrin molecules (fig. 3.7) were deposited. The first salt layer covered roughly 90% of the surface. Remarkably we found areas with a clear border between salt coverage and bare copper, which was caused by a missalignment of the sample during the salt evaporation. This missalignement did not expose the whole sample to the NaCl deposition, leading to this interesting result.

Fig. 4.9 shows a topographical (4.9a) overview with the corresponding CPD image (4.9b). The CPD image reveals several qualitative details. The first layer of NaCl is imaged slightly darker than the islands of the second and third layer. The molecules show a brighter contrast than the KBr steps. And finally the bare copper area covered with molecules, visible in the lower left, is imaged brighter as well. We also notice, that the underlying copper steps produce no CPD contrast at all. The whole range in the CPD image is 150 mV, which is relatively low but explained by the large amplitude of 20 nm.

As already mentioned, we also managed to image the border area between NaCl layers and pure copper. A topography image of this area is shown in fig. 4.9c. The lower part shows the expected step decoration of the rectangular NaCl islands from the first to the second layer. The upper part of the image shows a completely different situation. Instead of rectangular shaped and decorated salt structures, we observe polygonal shaped islands. Looking at the CPD image shown in fig. 4.9d gives some clarification. The upper part of the image shows a clear difference in the contact potential with a difference of roughly 500 mV. The molecules on the NaCl show a contrast of slightly below 100 mV compared to the salt layer. The bigger islands on copper have an increased contrast of approximately 150 mV compared to the metal. This higher contrast can also be explained by the larger extension of the molecular formations.

Having a closer look at the very border of the NaCl structure reveals that the salt is situated lower than the copper. This is caused by NaCl growing exactly to a higher (> 6 Å) copper step. It is also interesting to note that several NaCl islands close to the border show no decoration at

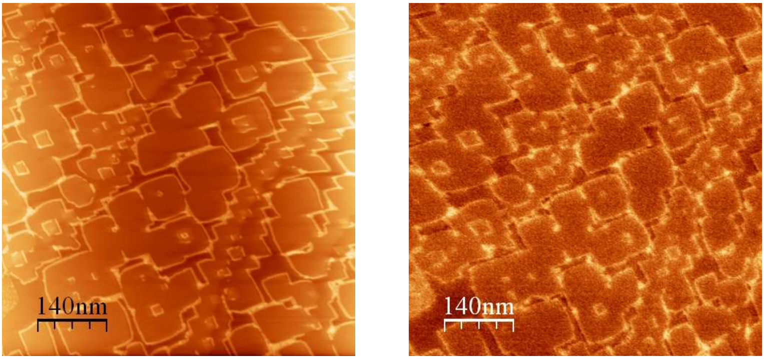

(a) Topography **(b)** CPD

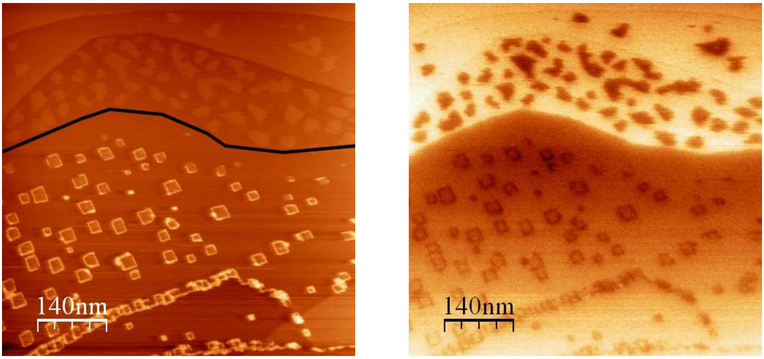

(c) Topography **(d)** CPD

Figure 4.9: Porphyrin molecules evaporated on a Cu sample partially covered with a NaCl thin film structure. Fig. 4.9a shows the topgraphy of an area fully covered with NaCl. The CPD image of this area (4.9b) reveals a distinct difference between molecules and NaCl aswell as between decorated and non-decorated steps. Fig. 4.9c shows the topography of an area partially covered with NaCl. The molecules arrange at the step of the NaCl islands aswell as on the bare copper substrate. This arrangement is better visible in the CPD image shown in fig. 4.9d. Frame edges 700 × 700 nm. Scan parameters: $f_0 = 170317\ Hz$, $f_1 = 1004810\ Hz$, $Q = 15000$, $A_{p-p} = 20\ nm$, $\Delta f = -7\ Hz$, $CPD_{range} = 150\ mV\ (b), 530\ mV\ (d)$, $V_{ac} = 500\ mV$.

all. This effect is probably caused by the higher affinity of the molecules to the metal substrate, which lets them diffuse onto the copper.

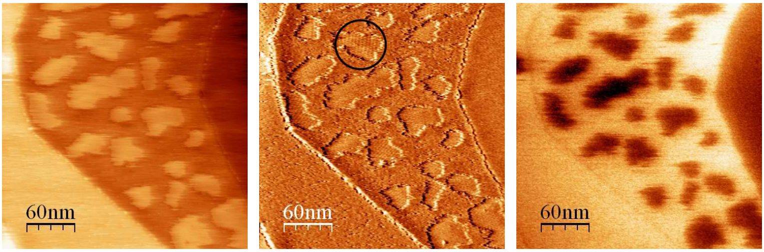

(a) Topography **(b)** Δf **(c)** CPD ($700 \times 700 nm$)

Figure 4.10: Topography (4.10a), Δf (4.10b) and CPD (4.10c) image of porphyrin assemblies on Cu(111). The topography shows no contrast within the islands. However the Δf image reveals a clear hexagonal peridocity of the molecular arrangement. In contrast to the fairly stable wires along alkal-halide edges the island borders seem to be highly mobile, explaining the blurry contrast. Scan parameters: $f_0 = 170317\ Hz$, $f_1 = 1004810\ Hz$, $Q = 15000$, $A_{p-p} = 20\ nm$, $\Delta f = -7\ Hz$, $CPD_{range} = 530\ mV$, $V_{ac} = 500\ mV$.

Fig. 4.10 shows topography, Δf and CPD image on the molecular islands on the copper. While topography and CPD image show no molecular contrast on top of the islands, the Δf image reveals a regular pattern on the islands which leads to the conclusion that these agglomerates are highly ordered in a hexagonal structure and therefore identical with the pattern estimated in fig. 4.8b. The slightly mobile border molecules are responsible for the fuzzy appearance of the islands in general. The CPD image shows a island size dependance of the contrast which is plotted in fig. 4.11a. Bigger islands seem brighter than the smaller ones. A significant part of the electrostatic forces detected in the CPD image are of long range nature (equation 1.5). The averaging effect caused by long range forces puts the tip into a crucial role concerning the resolution. Fig. 4.11b and 4.11c illustrate this averaging effect and reveal that only islands that have a larger diameter than a certain treshold ($> 35\ nm$) show a saturation effect. Above smaller structures the tip images always a part of the uncovered substrate next to the molecules. It is difficult to extrapolate a curve in fig. 4.11a down to the dimensions of single wires, especially because they can't be treated as a two dimensional structure since the determing factor of the averageing process is always the width of the wires. However, a tendency to the measured value of 80 mV

is given. Additionally the NaCl steps underneath the molecular single wires also contribute to CPD. Even though the measurements shown in fig. 4.10 do not allow a detailed quantitative explanation they qualitatively fit our expectations.

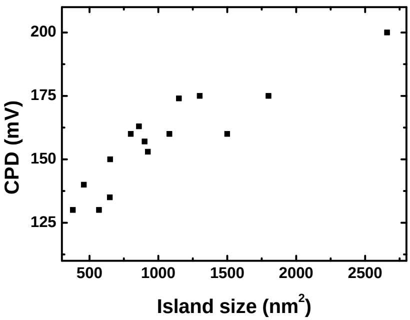

(a) CPD- Island size dependance

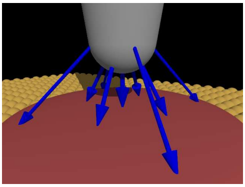

(b) CPD- Island size dependance

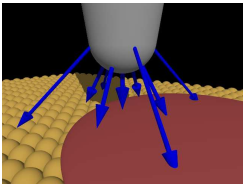

(c) CPD- Island size dependance

Figure 4.11: Fig. 4.11a points out the dependance of the measured CPD depending on the island size. Islands with a diameter of about 35 *nm* show a saturation in the CPD image. The sketches in fig. 4.11b and 4.11c visualize the averaging mechanism.

The molecules along the NaCl steps show no differences compared to the arrangements along the KBr steps. However, one special configuration was so far not observed on KBr. If the second layer NaCl-islands have a relatively small ($\approx 10\ nm$) distance between each other, the space in between is filled completely with multiwire ordered molecules. This happens even if the islands are not perfectly rectangularly shaped.

4.5 Monocyanoporphyrins and Gold-Nanoclusters on thin KBr-films

As a last series of experiments, we also evaporated gold onto the KBr films before the molecule deposition. The Cu crystal was prepared by two sputter-annealing cycles. The KBr then was deposited while the sample cooled down at roughly $110°C$. After the deposition the crystal was briefly checked for a sufficient coverage before the gold was evaporated. After this deposition the sample was introduced into the AFM for another check. At last monocyanoporphyrin molecules were evaporated onto the sample. The evaporation parameters are listed in table 4.1.

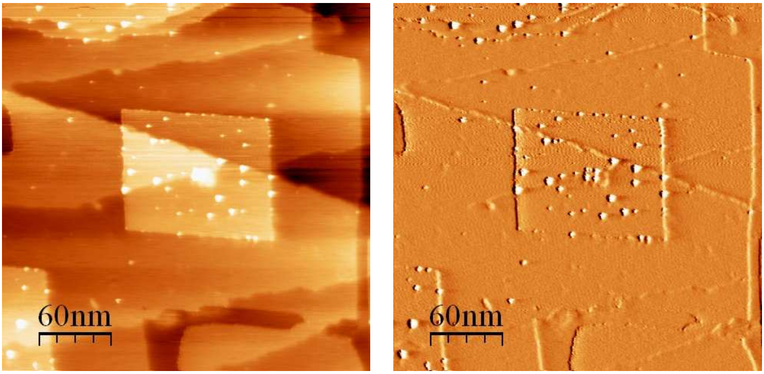

(a) Topography **(b)** Δf

Figure 4.12: Gold nanoclusters on KBr thin films on Cu(111). The majority of the clusters is sitting on the highly oriented rectangular islands. The remarkably better image contrast on the highest islands is probably caused by electrostatic forces. Frame edge: 300 × 300 nm. Scan parameters: $f_0 = 164731\ Hz$, $f_1 = 1026890\ Hz$, $Q_0 = 12000$, $A_{p-p} = 20\ nm$, $\Delta f_0 = -9\ Hz$.

Fig. 4.12 shows a topography and Δf image of the sample before the molecule deposition. Au nanoclusters are visible all over the sample but show an increased density on step edges and ontop of the highest layers of KBr. We also observe clusters on the first KBr layer but they show a weaker contrast. The Δf image (4.12b) is pointing this out in an even more explicit manner. The clusters have an apparent size of $5 - 15\ nm$ which is comparable to the sizes obtained on bulk KBr.

The poor resolution of the gold nanoclusters on the lower terraces is not easily explained. Usually this contrast difference is caused by electrostatic forces. However, during all measurements, the Kelvin controller was engaged, minimizing all electrostatic forces, which should suppress any contrast difference. A possible explanation could be that the clusters are charged by an amount, dependent on which layer they are situated. The ones sitting on the highest layer then would be differently charged than the lower ones where a partial charging or discharging through the thin insulating layer underneath might be possible. The charging of the culster can either result from the evaporation process or more likely from the KPFM measurements itself, where an ac-voltage of 500 mV was applied.

The imaging process after evaporation of the molecules was often hampered by the fast changing tip which often did not allow to record under stable conditions over more than one image. While we often scanned with a double tip and obtained rather poor images, we also observed ultra-high resolution for several hours. Those images are shown in the previous sections and do not reveal any details about the influence of the nanoclusters on the molecular growth.

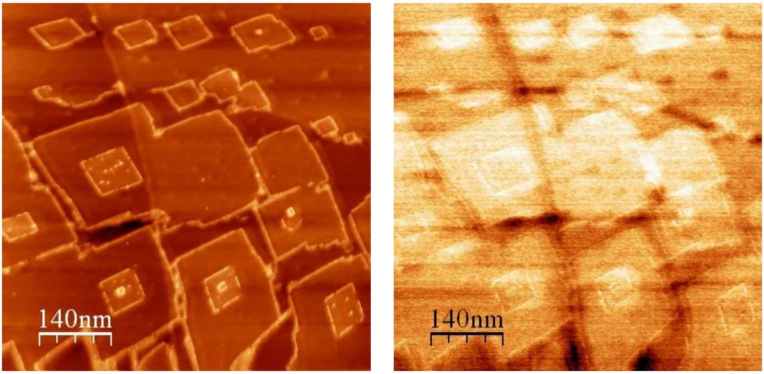

(a) Topography **(b)** CPD

Figure 4.13: Molecular assemblies on Au decorated KBr thin films on copper. Molecular wires are decorating the island and step edges of KBr as shown in various images before. The difference here is, that the growth along the steps is interrupted several times probably caused by Au clusters sitting at the steps. The CDP image (4.13b) shows different work-functions for the first and the second KBr layer. Additionally the underlying Cu steps and the molecules along the steps show a contrast. Frame edge: 700 × 700 nm. Scan parameters: $f_0 = 164731\ Hz$, $f_1 = 1026890\ Hz$, $Q_0 = 12000$, $A_{p-p} = 20\ nm$, $\Delta\ f_0 = -9\ Hz$, $CPD = 150\ mV$, $V_{ac} = 500\ mV$

Fig. 4.13 shows a typical image obtained on the fully prepared sample. Gold clusters are clearly visible on top of the highest islands. Molecular wires are decorating rectangular islands and KBr step edges. The main difference observed is that the wires decorating the islands are interrupted at several places. This indicates, that the nanoclusters can act as break-, start- or stoppoint. However, the resolution obtained on those images does not allow us to be fully conclusive at this point. Nevertheless, observations done on structures without gold decorations have never shown such a large amount of interruptions which clearly indicates an influence of the clusters. In the same image (4.13) we observe also wires which were not clearly interrupted or disturbed by clusters sitting at step edges. The molecular structures show bright spots which indicate the presence of nanoclusters. In brief, the influence of nanoclusters on the molecular growth is not completely understood but it is probably dependent on the location of the clusters[¶].

One explanation for this phenomenon could be the different locations of the clusters sitting at the step edges described by Goryl *et al.* [107]. Clusters sitting on the upper terrace are likely to influence the growth of the molecular wires less than clusters sitting at the lower terrace, right at the anchor site of the molecule. Another probable explanation can simply be to take the cluster size into account. Bigger clusters might interrupt the wires, while rather small ones are over grown. However, the resolution of our images did not allow us to do any statistics about the clustersize at step edges.

Although formations of wires between two nanoclusters as shown in fig. 3.22 have not been observed on other places[‖] than along island edges, the molecular growth seems to be influenced by the presence of clusters. Gold sitting on the step edges can interrupt the growth, forming dashed lines of molecular wires along island borders. One can imagine that a manipulated placement of nanoclusters at steps can lead to wires of a defined length. A more defined arrangement of Au-clusters can be achieved by deposing only a fraction of the amount of material. A gold tip can act as a source of gold clusters which can be deposited by applying voltage pulses [127].

4.6 Work Function Variations of the Salt Layers on Cu(111)

The CPD images of ultrathin salt films on copper all show a distinct difference between the first and the second layer. In order to gain information about reproducibility and also some quantitative numbers about the measured differences, several images were analyzed and the results displayed in tables 4.2 and 4.3. In the first three columns the average measured values over each surface are displayed. The forth and the fifth column then display the differences between the copper and the first

---

[¶] Apparently, the influence of gold clusters is more enhanced on single crystalline KBr compared to thin films.

[‖] Only valid on the thin film system. On bulk KBr also cluster-cluster growth on terraces was observed.

layer respectively the first and the second layer. The last column then indicates if a saturation on the copper has been found. Only copper areas of $\gtrsim 200\ nm$ diameter have shown saturation effects.[**]

The saturated difference between copper and KBr is about 200 mV and the difference between the first two KBr layers is about 40 mV. On NaCl this difference wasn't measured this often but the value of about 60 mV seems to be comparable. However, the 380 mV measured between a saturated copper area and the first NaCl layer is significantly larger than the value measured on the Cu-KBr system. Possible explanations for this phenomena are easily found. First the KPFM measurements have a strong distance dependancy on small structures, such as salt islands on metals [128, 129]. This fact alone and the limited spatial resolution of AM-KPFM doesn't allow to interprete the results displayed in tables 4.2, 4.3 quantitatively. Further reasons for the difference between the results obtained on KBr and NaCl islands is the fact that the first NaCl layer grows as a double layer while KBr is forming a single layer. To obtain quantitave results about the work functions of thin salt films on metals, either one has to produce fairly larger salt carpets or one has to employ FM-KPFM techniques.

Another drawback in this measurements is the influence of the tip shape. Repeating the measurements shown in table 4.2 led to a CPD of approximately 800 mV, which is roughly 4 times higher than the values obtained in the fisrt measurement series. We believe that this difference is cause by a much blunter tip. The frequency shift in the first series of images was around $-8\ Hz$ and the image quality was generally good indicating a sharp tip. The second series of images was taken with a frequency shift of $-25\ Hz$ and the overall contrast was more blurry indicating a rather blunt tip. This leads to the conclusion that the tip sample distance in the second series was significantly smaller than in the first one. In conclusion, the measurements of local work function variations on heterogenous surfaces in a quantitave way has to be carried out extremely carefully. Especially the distance dependance of the measurements have to be fully calibrated.

4.7 Conclusions

The investigation of conductance properties of molecular wires is of great importance in the field of molecular electronics. The goal of the measurements described in this chapter was to find indications of possible optical activity and to measure those by means of KPFM. So far the

---

[**] The saturation effect is explained in section 4.4.

Cu (mV)	1st layer (mV)	2nd layer (mV)	$CDP_{CU-1st\ layer}$ (mV)	$CDP_{1st-2nd\ layer}$ (mV)	Saturation
-615	-820	-876	205	56	yes
-626	-807	-843	181	36	yes
-599	-764	-796	165	32	no
-570	-771		201		yes

Table 4.2: CPD differences on KBr thin films on copper

Cu (mV)	1st layer (mV)	2nd layer (mV)	$CDP_{CU-1st\ layer}$ (mV)	$CDP_{1st-2nd\ layer}$ (mV)	Saturation
280	-110	-170	390	60	yes
545	280		265		no
545	160		385		yes
590	220		370		yes

Table 4.3: CPD differences on NaCl thin films on copper

experimental setup has not proven to be sophisticated enough to perform illumination and measurements with the required accuracy. The illumination performed with white light led to a increase of the sample temperature which influenced the measurement more than the expected change in the CPD of the molecules. A better approach might be to use chopped light at a more defined wavelength in order to prevent an increase of the system temperature.

Despite this small drawback, the measurements on thin salt films proved to be extremely successful. On the first layer of KBr, which is probably a single layer we observed a different adsorption order than on the other layers or on bulk material. This new structure is probably induced by the underlying substrate. On NaCl on the other hand this structure is never observed, which is probably caused by the fact that the first layer is assumed to be a double layer. We have also shown that molecular carpets arrange on bare copper forming islands similar to the structures observed on the first KBr layer.

The deposition of molecules on thin KBr films with gold nanoclusters on top did not reveal significant differences compared to the measurements done on bulk KBr. The most remarkable feature is that the growth along the step edges is influenced by Au-clusters, leading to the interruption of themolecular wires.

5 Conclusions and Outlook

This work focused on the investigation by means of nc-AFM of porphyrin assemblies on bulk insulating crystals and on ultrathin insulating layers. The adsorption of monocyanoporphyrin molecules was studied for the first time and resulted in various reproducible assemblies on the surfaces.

Steps, islands and pit edges of alkali-halide crystals act as trapping points for polar molecules, preventing them from diffusing freely over the surface. Simultaneously, intermolecular interactions force the monocyanoporphyrins to form $\pi-\pi$-stacks. These stacks grow along the edges, forming long molecular wires. This growth is affected by the potential corrugation at the step edge which forces the negatively charged nitrogen atom of the porphyrin to sit on top of a positively charge potassium ion, resulting in a intermolecular distance corresponding to the lattice constant of the underlying substrate.

At increased coverages of molecules, two-dimensional arrays start to grow away from the steps across the terraces. The preferred growth orientation is the $\langle 110 \rangle$-direction on KBr and the $\langle 100 \rangle$-direction on NaCl. While maintaining their stacking, intermolecular distances and tilt angles are slightly different than along steps. The lower corrugation of the surface potential across the terraces is no longer the dominant term but rather the equilibrium distance of the $\pi - \pi$-stack.

Investigations about possible electrical contacting of the wires have been performed. The deposition of gold nanoclusters on KBr has shown promising results, as they seem to influence the growth of the molecular assemblies. Along step edges, gold nanoclusters can interrupt the wire growth. As a result, we obtained wires growing from cluster to cluster along step edges. A controlled deposition of such nanoclusters can lead to a control over the length of the single wires. Au-clusters sitting on terraces can either act as starting or endpoint for multiwires. We have shown that two clusters sitting on a line in the $\langle 110 \rangle$-direction lead to a wire growth in between them. A first step to step independent growth of molecular wires on insulating surfaces with attached nanocontacts.

The adsorption behaviour of the cyanoporphyrins was also studied on ultrathin insulating films on Cu(111) in order to allow an easier application of KPFM. We have shown that KBr thin films allow the molecules to grow in a two phase system. The first layer of KBr is thin enough (one layer, 0.33 nm), to still allow the copper to influence the molecular growth. Along KBr steps the molecular growth is identical to the formations on bulk material. Opposite to that on areas close to an underlying copper step porphyrins grow in a hexagonal lattice structure and are probably adsorbet with their core more parallel to the surface loosing their $\pi - \pi$-stacking.

The application of KPFM was helpful to distinguish different areas of the sample. Contrast changes between metal substrate, different salt layers and molecules were observed, allowing a qualitative analysis. However, due to various reasons quantitative results were not obtained.

The next step in this ongoing project is now to gain more understanding of the molecular arrangement. With this knowledge one can fine tune the substrate configuration even better to obtain more predictible results. Another topic of interest is to test conductivity and optical properties of the molecular wires. For that, a more sophisticated setup is needed, which allows illumination of the sample without heating it up.

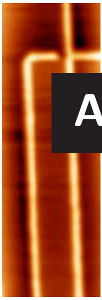

A

Bromium Substituted Sub-PC Molecules on KBr.

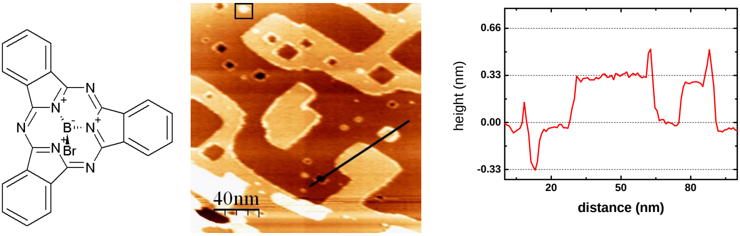

(a) Sub-Pc **(b)** Topography ($200 \times 200\ nm$) **(c)** Linesection

Figure A.1: Topography (A.1b) and crosssection (A.1c) of Sub-Pc molecules deposited on nanostructured KBr. The molecules decorate steps but also fill the smaller pits in the surface.

The focus on this work was mainly laid on the investigation of porphyrin molecules. However, various other molecules were deposited on nanostructured KBr. Most of them didn't adsorb stable enough to be investigated by nc-AFM. With the results from this thesis in mind, some candidates showed promising results on the second sight.

Nony *et al.* investigated the assembly of chlorine substituted Sub-PC in nanometer sized pits on KBr[72]. As a consequence the same experiments were repeated with bromine substituted Sub-Pc molecules. The obtained result after deposing 0.5 ML on the nanostructured substrate is shown in fig. A.1. Fig. A.1b shows a topography image of a (200×200 *nm*)- area. The line section along the line is shown in fig. A.1c.

What was first under suspicion to be a scanning artifact was later identified as fairly regular step decoration along pit- and island-edges. The linesection shows a clear difference between decorated and undecorated pits. At the upper framedge of fig. A.1b, marked by the black frame, we further observe a bright rectangular island. Height analysis of this structure rules out a single layer high island. However, the measured 0.6 *nm* can indicate a double layer or a single layer pit, filled with molecules. The measurement is not conclusive at this point.

The dipole moment of the bromine substituted Sub-PC is slightly lower than the one of the chlorine substituted one. The molecules used by Nony *et al.* only assembled in small ($\lesssim 15$ *nm*) pits. Larger pits only showed edge decorations and on the terraces no molecules were visible. From this point of view we assume, that the bromine Sub-PC have a similar behaviour, but are slightly weaker bonded to the surface which probably leads to the need of even smaller pits in order to observe ordered assemblies.

B

The Amplitude Calibration Program.

The SPM control software NANONIS[53] is based on LabView[62]. The company therefore provides the users with interface tools to allow limited control over the software via LabView over ethernet. The tools package allows basic functions to read out channels and to set different setpoints.

The self written amplitude calibration programm is based on calculations on the calibration methods presented in section 2.5, namely it employes the variation of the amplitude with a simultaneous adjustment of the frequency shift.

The program interface allows the user to set some parameters, while other parameters are directly read out from the scan software. Especially, the calibration factors, the center amplitude and the frequency setpoint cannot be manipulated by the application in order to prevent user generated tip crashes. On the other hand, the user may set the amplitude range to be swept and the number of sweeps. Adjustments in the amplitude or the frequency setpoint can be done before the start button was pressed. After pressing the start button the program performs the requested number of sweeps and calculates the calibration factor for the amplitude.

In detail the amplitude is swept from the setpoint A_{set} to $A_{set} + \Delta A$ to $A_{set} - \Delta A$ and back to A_{set}. Each ΔA step is divided in 100 substeps leading to 400 amplitude changes per sweep. The program first calculates $\Delta A_{step} = \frac{\Delta A}{100}$ and then augments the current amplitude A_0 by this value to A_1. At the same time the frequency setpoint is adjusted according to $f_1 = f_0 c^{-3/2}$ with $c = \frac{A_1}{A_0}$ in order to guarantee the same tip sample separation at the turning point of the oscillation. The difference in the z-signal $\Delta z = z_0 - z_1$ then equals the change of the amplitude.

To improve the accuracy of the calibration, several improvements have been implemented. After each cycle the program pauses for several milliseconds to let the z-controller become stable. The read-out of the z-signal is done multiple times and then averaged in order to rule out fluctuation values and reduce noise.

After performing the sweeploops the program calculates the amplitude calibration and suggest to submit it to the scan software. The user then can decide to agree or the cancel the action. Upon cancelling, the calibration can also be entered manually. If the programm performs the entry, the z-piezo is lifted prior to the calibration adjustmenbt in order to prevent possible tip crashes.

To obtain maximal accuracy for the calibration, it is adviseful to let the z-controller become stable and free of drift. I suggest also to choose frequency and amplitude setpoints at scan-stable values, so the safe-tip condition of the scan software is fulfilled during the calibration. If the system is drifting more than 1 nm/min it's suggested to engage the drift correction of NANONIS or to let the system find its thermal equilibrium by waiting several minutes whilie the z-controller is engaged. $\mathit{\Delta} A$ should not be chosen larger than 25% of A_{set} in order to operate the amplitude controller of the scan software in the optimal regime. However, choosing $\mathit{\Delta} A$ too small may lead to inaccurate results. Therefore we suggest to set the sweep range to $15 - 20\%$ of the amplitude setpoint.

C KPFM Simulations on NaCl Thin Films on Cu(111)

Carl and Glatzel [130] developed a program to simulate KPFM experiments. By solving the poisson equations in two dimensions, the code is using square finite elements described in [131, 132, 133] and employs methods described in [134]. Previously, Sadewasser *et al.* [135] used a one dimensional method to simulate heights on C60 molecules on HOPG.

The nonlinear poisson equation for a semiconductor is given by [131]

$$\frac{\partial^2 \phi}{\partial x^2} + \frac{\partial^2 \phi}{\partial y^2} - \frac{q n_i}{\epsilon_s}\left(e^{\phi/V_T} - e^{-\phi/V_T}\right) = -\frac{qD}{\epsilon_s} \tag{C.1}$$

with ϕ the electrostatic potential, q the elementary electron charge, D the concentration of impurities, ϵ_s the permittivity of the semiconductor, $n_i e^{\phi/V_T} = n$ and $n_i e^{-\phi/V_T} = p$ the doping concentrations. n_i is the intrinsic carrier concentration and V_T the thermal voltage given by $V_T = q/kT$.

Poisson's equations may be discretized and rewritten as [133]

$$\mathcal{F}(\phi) = 0, \tag{C.2}$$

with ϕ the vector of M unknow grid potentials, and $\mathcal{F} : R^M \to R^M$ an M-dimensional, nonlinear mapping. Such a set of nonlinear equations is usually solved iteratively as

$$\phi^{k+1} = \phi^k - J^{-1}(\phi^k)\mathcal{F}(\phi^k), \tag{C.3}$$

where k is the iteration index and J the Jacobian matrix of $\mathcal{F}$ at $\phi = \phi^k$. The Newton scheme (eq. C.3) can be rewritten as the repeated solution of the linear system.

$$J(\phi^k)\phi^{k+1} = J(\phi^k)\phi^k - \mathcal{F}(\phi^k). \tag{C.4}$$

Ouwerling [133] further points out, that the specific case of the Poissons's equations, iteration methods are useful to solve the system.

Mayergoyz used the ideas described above to formulate the full-step Jacobi-Newton method [131, 133], using Jacobi relaxation for the linear outer loop and Newton iterations for the inner one. This scheme was first proposed by Lieberstein [136] in 1959.

Eq. C.2 then can be rewritten as

$$A\phi + \chi(\phi) = 0, \tag{C.5}$$

with A a discretization matrix and χ a diagonal nonlinear mapping. Since $\chi(\phi)$ is diagonal, the Jacobian matrix J is also diagonal with the elements

$$J_{ii} = a_{ii} + \frac{\partial \chi_i}{\partial \phi_i} \; (i \in [1, M]), \tag{C.6}$$

and therefore eq. C.3 can be written as

$$\phi_i^{k+1} = \phi_i^k - \frac{\mathcal{F}_i(\phi^k)}{J_{ii}} = \phi_i^k - \frac{A_{(i)} \cdot \phi^k + \chi_i(\phi_i^k)}{a_{ii} + (\partial \chi_i / \partial \phi_i^k)}, \tag{C.7}$$

with ϕ_i the potential of the grid element and $A_{(i)}$ the ith row of the discretization matrix A of eq. C.5. Eq. C.7 is the base equation for our code. Keller [132] and Ouwerling [133] introduced several simplifications* with the goal to make numerical calculations faster.

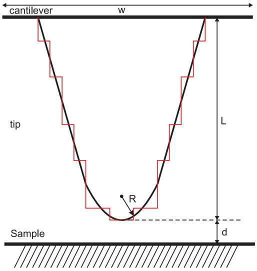

Figure C.1: Geometry of the tip for the simluation.

Practically, the code uses two matrixes. The sample matrix has to be generated prior to the simulations and is then fed into the program as an input file. The tip matrix is calculated by the code based on given parameters, such as radius, size and opening angle. The tip matrix file consists the capacitance gradient as a function of the parameters mentioned above. For that, the tip shape is turned to a staircase shape (cf. the red line in fig. C.1), discretizing the tip sample system to N parallel plate capacitors. Finally, the tip matrix is then scanned over the sample by two double loops. The first double loop scans the tip over the samplematrix, the second one calculates the CPD at every sample point. The number of iterations for each point is determined

---

[*] The simplifications constisted the introduction of scaled variables and reducing the numbers of iterations.

dynamically. The break condition is set to $|\phi_i^{k+1} - \phi_i^k| < \varepsilon$, with ε being the convergation criteria.

In our simulations we used a earlier version of the program. This version only calculated the capacitance gradient between tip and sample and doesn't emply the poisson equations yet. Therefore, the obtained data contains only qualitative information.

To gain informations about the tip apex size during our scans, several simulations were performed. As a template, the NaCl thin films on Cu(111) image shown in fig. 4.2 was taken. The image was scaled up to 1024 × 1024 points and the bare Cu areas were set to orange color and the salt covered parts to a uniform white background color (fig. C.2c). A self written c-program then converts this image into a potential matrix

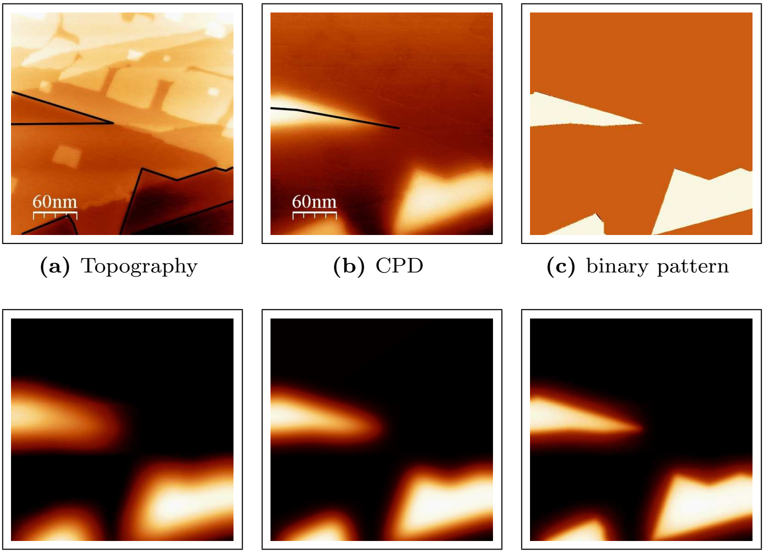

(a) Topography **(b)** CPD **(c)** binary pattern

(d) 15 *nm* tip **(e)** 7 *nm* tip **(f)** 2 *nm* tip

Figure C.2: KPFM simulations on NaCl thin films on Cu(111). Fig. C.2a shows topgraphy and fig. C.2b the corresponding CPD image. From those images a binary file shown in fig. C.2c was created. After turning this pattern into a ascii formatted matrix, several images with different tip radii were calculated. Tip apex radii of 15 *nm* C.2d, 7 *nm* C.2e and 2 *nm* C.2f are shown above. Comparing the simulations with the measurement in fig. C.2b suggests a tip radius of ≈ 7 *nm*.

acting as input file for the simulation program.

We performed several simulations with various parameters. Fig. C.2d-C.2f show three simulated images with different tip radii (15, 5 and 2 nm). All other parameters were constant. Each image is averaged over a complete oscillation cycle with a sinusoidal weight function. The amplitude was set to $A_{osc} = 24\ nm$ and simulations were done at a tip sample distances of 1, 5, 9, 13, 17, 21 and 25 nm resulting in seven images per tip radius. Each of those images took roughly five minutes yielding in a total simulation time of slightly above 35 minutes for one oscillation cycle.

The influence of the tip radius is quite distinctive, as the simulations in fig. C.2 reveal. A more careful comparison can be made by investigating crossections across the structures (cf. the black line in fig. C.2b) shown in fig. C.3.

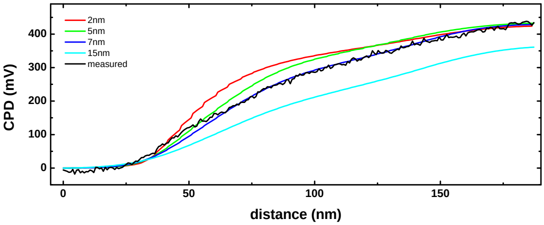

Figure C.3: Linesections of the simulated images. The simulation values have been recalibrated to match the maximum of the measured result. This was necessary, since the tip condition is unknown. The results therefore contain no quantitative information. The measured curve shows a good match with the 7 nm tip radius simulation except in the area where the Cu structure is very pointy. In this area even the smalles tip radius yields in simulation values which are too small. This effect might be caused by a nanotip sitting at the apex of the regular tip.

At the pointy end of the copper structure the simulation suggest a tip radius of about 2 nm judging from the shape of the curve. In contrast, the simulation suggests a tip radius of about 7 nm for the rest of the structure. This effect can be caused either by a nanotip, providing a sharper short range signal.

So far, only binary image files have been processed for convencience but the obtained results look promising. A next step in this project now is to run the simulations with the full program that employs the poisson equations to obtain qantitative data. Therefore the input files will have to be adjusted. Therefore the c-program has to be extended with an user interface allowing more customized operations. After this is done, simulations of more complex systems can be started.

List of Figures

List of Tables

Bibliography

[1] M. Schulz. The end of the road for silicon. *Nature*, 399:729, 1999. [cited at p. vi]

[2] R. Feynman. "there's plenty of room at the bottom", 1959. This talk given at the annual meeting of the American Physical Society at the California Institute of Technology was first published in the February 1960 issue of Caltech's *Engineering and Science*, which owns the copyright. It has been made available on the web at http://www.zyvex.com/ nanotech/ feynman.html with their kind permission. [cited at p. vi]

[3] ITRS. International technology roadmap for semiconductors. Technical report, ITRS, 2005. [cited at p. vi]

[4] G. M. Whitesides, J. P. Mathias, and C. T. Seto. *Science*, 254:1312–1319, 1991. [cited at p. vi, 28]

[5] J.V. Barth, G. Constantini, and K. Kern. Engineering atomic and molecular nanostructures at surfaces. *Nature*, 437:671–679, 2005. [cited at p. vi]

[6] C. Joachim, J.K. Gimzewski, and A. Aviram. Electronics using hybrid-molecular and mono-molecular devices. *Nature*, 408:541, 2000. [cited at p. vi]

[7] G. Binnig and H. Rohrer. Scanning tunneling microscopy. *Helv. Phys. Acta*, 55:726–735, 1982. [cited at p. 3]

[8] G. Binnig, H. Rohrer, Ch. Gerber, and E. Weibel. 7x7 reconstruction on Si(111) resolved in real space. *Phys. Rev. Lett.*, 50(2):120–123, 1983. [cited at p. 3]

[9] J. Wintterlin, J. Wiechers, H. Brune, T. Gritsch, H. Höfer, and R.J. Behm. Atomic resolution of close-packed metal surfaces by scanning tunneling microscopy. *Phys. Rev. Lett.*, 62:59, 1989. [cited at p. 3]

[10] F.J. Giessibl. Advances in atomic force microscopy. *Rev. Mod. Phys.*, 75(3):949–983, 2003. [cited at p. 3, 6]

[11] G. Binnig, C.F. Quate, and Ch. Gerber. Atomic force microscopy. *Phys. Rev. Lett.*, 56(9):930–933, 1986. [cited at p. 3]

[12] G. Binnig, Ch. Gerber, E. Stoll, T.R. Albrecht, and C.F. Quate. Atomic resolution with atomic force microscopy. *Europhys. Lett.*, 3(12):1281–1286, 1987. [cited at p. 3]

[13] F. Ohnesorge and G. Binnig. True atomic resolution by atomic force microscopy through repulsive and attractive forces. *Science*, 260:1451–1456, 1993. [cited at p. 3]

[14] F.J. Giessibl and G. Binnig. True atomic resolution on KBr with a low-temperature atomic force microscope in ultrahigh vacuum. *Ultramicroscopy*, 42-44:281–286, 1992. [cited at p. 3]

[15] T.R. Albrecht, P. Grütter, D. Horne, and D. Rugar. Frequency modulation detection using high-Q cantilevers for enhanced force microscope sensitivity. *J. Appl. Phys.*, 69:668, 1991. [cited at p. 3, 6, 23]

[16] F.J. Giessibl. Atomic resolution of silicon(111)7x7 by atomic force microscopy through repulsive and attractive forces. *Science*, 267(68):1451–1455, 1995. [cited at p. 3, 6]

[17] G. Meyer and N. Amer. Simultaneous measurement of lateral and normal forces with an optical beam deflection atomic force microscope. *Appl. Phys. Lett.*, 57:2089, 1990. [cited at p. 5]

[18] E. Meyer, H. Heinzelmann, H. Rudin, and H.-J. Güntherodt. Atomic resolution on LiF(001) by atomic force microscopy. *Z. Phys. B - Condensed Matter*, 79:3–4, 1990. [cited at p. 5]

[19] S. Maier, O. Pfeiffer, Th. Glatzel, E. Meyer, T. Filleter, and R. Bennewitz. Asymmetry in the reciprocal epitaxy of NaCl and KBr. *Phys. Rev. B*, 75:195408, 2007. [cited at p. 5]

[20] G.M. McClelland, R. Erlandsson, and S. Chiang. *Atomic force microscopy: general principles and a new implementation, in Review Progress in Quantitative Non-Destructrive Evaluation, edited by D.O. Thompson and D.E. Chimenti*, volume 6B, page 1307. Plenum, New York, 1987. [cited at p. 6]

[21] Y. Martin, C.C. Williams, and H.K. Wickramasinghe. Atomic force microscope-force mapping and profiling on a sub 100-Å scale. *J. Appl. Phys.*, 61(10):4723–4729, 1987. [cited at p. 6]

[22] J.N. Israelachvili. *Intermolecular and Surface Forces.* Academic Press, London, 1985. [cited at p. 7, 29]

[23] R. Bennewitz, M. Reichling, and E. Matthias. Force microscopy of cleaved and electron-irradiated CaF_2 (111) surfaces in ultra-high vacuum. *Surface Science*, 387:69, 1997. [cited at p. 8]

[24] M. Saint Jean, S. Hudlet, C. Guthmann, and J. Berger. Van der waals and capacitive forces in atomic force microscopes. *J. Appl. Phys.*, 86(9):5245, 1999. [cited at p. 8]

[25] B.M. Law and F. Rieutord. Electrostatic forces in atomic force microscopy. *Phys. Rev. B*, 66:35402, 2002. [cited at p. 8]

[26] F.J. Giessibl. Theory for an electrostatic imaging mechanism allowing atomic resolution of ionic crystals by atomic force microscopy. *Phys. Rev. B*, 45(23):13815–13818, 1992. [cited at p. 8]

[27] J. E. Lennard-Jones. Cohesion. *The Proceedings of the Physical Society*, 43:461, 1931. [cited at p. 9]

[28] Neil W. Ashcroft and N. David Mermin. *Solid State Physics.* Harcourt Brace College Publishers, 1976. [cited at p. 9]

[29] F.J. Giessibl. Forces and frequency shifts in atomic-resolution dynamic-force microscopy. *Phys. Rev. B*, 56(24):16010–16015, 1997. [cited at p. 9, 22]

[30] C.L. Pekeris. The rotation-vibration coupling in diatomic molecules. *Phys Rev.*, 45:98, 1934. [cited at p. 9]

[31] N. Sasaki and M. Tsukada. Effect of microscopic nonconservative process on noncontact atomic force microscopy. *Jap. J. Appl. Phys.*, 39:L1334, 2000. [cited at p. 10]

[32] H. Hug and A. Baratoff. *Measurement of Dissipation Induced by Tip Sample Interactions*, pages 395–432. NanoScience And Technology. Springer, Berlin, 2002. [cited at p. 10]

[33] W. Denk and D. Pohl. Local electrical dissipation imaged by scanning force microscopy. *Appl. Phys. Lett.*, 59(17):2171–2173, 1991. [cited at p. 10]

[34] M. Gauthier and M. Tsukada. Theory of noncontact dissipation force microscopy. *Phys. Rev. B*, 60(16):11716, 1999. [cited at p. 10]

[35] M. Gauthier and M. Tsukada. Damping mechanism in dynamic force microscopy. *Phys. Rev. Lett.*, 85(25):5348, 2000. [cited at p. 10]

[36] L.N. Kantorovich. A simple non-equilibrium theory of non-contact dissipation force microscopy. *J. Phys.: Condens. Matter*, 13(5):945, 2001. [cited at p. 10]

[37] S.P. Jarvis, H. Yamada, K. Kobayashi, A. Toda, and H. Tokumoto. Normal and lateral force investigation using magnetically activated force sensors. *Appl. Surf. Sci.*, 157:314, 2000. [cited at p. 10]

[38] O. Pfeiffer. *Quantitative dynamische Kraft- und Dissipationsmikroskopie auf molekularer Skala.* PhD thesis, Universität Basel, 2004. [cited at p. 10]

[39] L. Kelvin. Contact electricity of metals. *Phil. Mag.*, 46:82, 1898. [cited at p. 11]

[40] J.M.R. Weaver and D.W. Abraham. *J. Vac. Sci. Technol. B*, 9:1559, 1991. [cited at p. 12]

[41] S. Hudlet, M. Saint-Jean, C. Guthmann, and J. Berger. Evaluation of the capacitive force between an atomic force microscopy tip and a metallic surface. *Eur. Phys. J. B*, 2(1):5, 1998. [cited at p. 12]

[42] Ch. Sommerhalter, Th. Matthes, Th. Glatzel, A. Jäger-Waldau, and M. Ch. Lux-Steiner. High-sensitivity quantitative kelvin probe microscopy by non-contact ultrahigh vacuum atomic force microscopy. *Appl. Phys. Lett.*, 75:286, 1999. [cited at p. 13]

[43] A. Kikukawa, S. Hosaka, and R. Imura. Silicon pn junction imaging and characterizations using sensitivity enhanced Kelvin probe force microscopy. *Appl. Phys. Lett.*, 66(25):3510–3512, 1995. [cited at p. 13]

[44] Ch. Sommerhalter, Th. Glatzel, Th. W. Matthes, A. Jäger-Waldau, and M. Ch. Lux-Steiner. High-sensitivity quantitative Kelvin probe microscopy by noncontact ultra-high-vacuum atomic force microscopy. *Appl. Surf. Sci.*, 157:263, 2000. [cited at p. 13, 21]

[45] Th. Glatzel, S. Sadewasser, R. Shikler, Y. Rosenwaks, and M.Ch. Lux-Steiner. Kelvin probe force microscopy on III-V semiconductors: the effect of surface defects on the local work function. *Mat. Sci Eng. B*, 102:138, 2003. [cited at p. 13]

[46] S. Kitamura and M. Iwatsuki. High-resolution imaging of contact potential difference with ultrahigh vacuum noncontact atomic force microscope. *Appl. Phys. Lett.*, 72(24):3154–3156, 1998. [cited at p. 14]

[47] L. Howald, E. Meyer, R. Lüthi, H. Haefke, R. Overney, H. Rudin, and H.-J. Güntherodt. Multifunctional force microscope for facile operation in ultrahigh vacuum. *Appl. Phys. Lett.*, 63:117, 1993. [cited at p. 16]

[48] Omicron GmbH. http://www.omicron.de. [cited at p. 17]

[49] G. Meyer and N.M. Amer. Novel optical approach to atomic force microscopy. *Appl. Phys. Lett.*, 12:1045–1047, 53. [cited at p. 17]

[50] SuperlumDiodes Ltd. *http://www.superlumdiodes.com.* [cited at p. 17]

[51] E.R.I. Abraham and E.A. Cornell. Teflon feedthrough for coupling optical fibers into ultrahigh vacuum systems. *Applied Optics*, 37(10):1762–1763, 1998. [cited at p. 18]

[52] M.Bammerlin, S.Messmer, and A. Tonin. Kompletter neubau des uhv-afm (1998). Blueprints. [cited at p. 18]

[53] NANONIS. *http://www.nanonis.com.* [cited at p. 19, 23, 82]

[54] Christian Loppacher. *Nichtkontakt-Rasterkraftmikroskopie mit digitalem Phasenregelkreis.* PhD Thesis, Universität Basel, 2000. [cited at p. 19]

[55] Nanosurf AG. http://www.nanosurf.ch. Liestal, Switzerland. [cited at p. 19]

[56] R. Bennewitz. *Kraftmikroskopie an CaF_2(111): Charakterisierung der reinen und der elektronenstrahlmodifizierten Oberfläche.* Verlag Dr. Köster , Wissenschaftliche Schriftenreihe Physik Band 59 (ISBN 3-89574-274-3), Berlin, 1997. [cited at p. 20]

[57] M. Guggisberg, M. Bammerlin, Ch. Loppacher, O. Pfeiffer, A. Abdurixit, V. Barwich, R. Bennewitz,

A. Baratoff, E. Meyer, and H.-J. Güntherodt. Separation of interactions by non-contact force microscopy. *Phys. Rev. B*, 61:11151, 2000. [cited at p. 20]

[58] J. Lü, L. Eng, R. Bennewitz, E. Meyer, H.-J. Güntherodt, E. Delamarche, and L. Scandella. Surface potential studies of self-assembling monolayers using kelvin probe force microscopy. *Surf. Interface Anal.*, 27:368, 1999. [cited at p. 20]

[59] S. Sadewasser and M. Ch. Lux-Steiner. Correct height measurement in noncontact atomic force microscopy. *Phys. Rev. Lett.*, 91(26):266101, 2003. [cited at p. 20]

[60] Martin Guggisberg. *Lokale Messung von atomaren Kräften*. PhD Thesis, Universität Basel, 2000. [cited at p. 22]

[61] F.J. Giessibl and H. Bielefeldt. Physical interpretation of frequency-modulation atomic force microscopy. *Phys. Rev. B*, 61(15):9968, 2000. [cited at p. 22]

[62] National Instruments. *http://www.ni.com*. [cited at p. 23, 82]

[63] E. Meyer, H.J. Hug, and R. Bennewitz. *Scanning Probe Microscopy: The Lab on a Tip*. Springer-Verlag, Berlin, 2004. [cited at p. 23]

[64] S. Rast, Ch. Watttinger, U. Gysin, and E. Meyer. The noise of cantilevers. *Nanotechnology*, 11:169–172, 2000. [cited at p. 24]

[65] O. Pfeiffer, C. Loppacher, C. Wattinger, M. Bammerlin, U. Gysin, M. Guggisberg, R. Bennewitz, E. Meyer, and H.-J. Güntherodt. Using higher flexural modes in non-contact force microscopy. *Appl. Surf. Sci.*, 157:337, 2000. [cited at p. 24]

[66] NANOSENSORS. *http://www.nanosensors.com*. [cited at p. 24]

[67] T. Eguchi and Y. Hasegawa. High resolution atomic force microscopic imaging of the Si(111)-(7x7) surface: Contribution of short-range force to the images. *Phys. Rev. Lett.*, 89(26):266105, 2002. [cited at p. 25]

[68] M. Tomitori and T. Arai. Tip cleaning and sharpening processes for non-contact atomic force microscope in ultrahigh vacuum. *Appl. Surf. Sci.*, 140:432–438, 1999. [cited at p. 25]

[69] H. Lüth. *Solid surfaces, Interfaces and Thin Films*. Springer-Verlag, Berlin, Heidelberg, NY, Barcelona, Hong Kong, London, Milan, Paris, Tokyo, 2001. [cited at p. 26]

[70] R. Bennewitz, S. Schär, V. Barwich, O. Pfeiffer, E. Meyer, F. Krok, B. Such, J. Kolodzej, and M. Szymonski. Atomic resolution images of radiation damage in KBr. *Surface Science*, 474:L197, 2001. [cited at p. 26]

[71] B. Such, J. Kolodziej, P. Czuba, P. Piatkowski, P. Struski, F. Krok, and M. Szymonski. Surface topography dependent desorption of alkali halides. *Phys. Rev. Lett.*, 85:2621, 2000. [cited at p. 26, 31]

[72] L. Nony, E. Gnecco, A. Baratoff, A. Alkauskas, R. Bennewitz, O. Pfeiffer, S. Maier, A. Wetzel, E. Meyer, and Ch. Gerber. Observation of individual molecules trapped on a nanostructured insulator. *Nano Letters*, 11:2185–2189, 2004. [cited at p. 26, 32, 37, 80]

[73] M. Bammerlin, R. Lüthi, E. Meyer, A. Baratoff, J. Lü, M. Guggisberg, Ch. Gerber, L. Howald, and H.-J. Güntherodt. True atomic resolution on the surface of an insulator via ultrahigh vacuum dynamic force microscopy. *Probe Microscopy*, 1:3, 1997. [cited at p. 28]

[74] M. Bammerlin, R. Lüthi, E. Meyer, A. Baratoff, J. Lü, M. Guggisberg, C. Loppacher, C. Gerber, and H.-J. Güntherodt. Dynamic sfm with true atomic resolution on alkali halide surfaces. *Appl. Phys. A*, 66:293, 1998. [cited at p. 28]

[75] F. Zerbetto E. R. Kay, D. A. Leigh. Synthetic molecular motors and mechanical machines. *Angew. Chem.*, 47:72, 2007. [cited at p. 28]

[76] J.-M. Lehn. *Supramolecular Chemistry: Concepts and Perspectives*. VCH, New York, 1995. [cited at p. 28]

[77] T. Jung, R.R. Schlittler, and J.K. Gimzewski. Conformational identification of individual adsorbed molecules with STM. *Nature*, 386:696, 1997. [cited at p. 29]

[78] D. Bonifazi, H. Spillmann, A. Kiebele, M. de Wild, P. Seiler, F. Cheng, H.-J. Güntherodt, T. Jung, and F. Diederich. *Angew. Chem.*, 43:4759–4763, 2004. [cited at p. 29]

[79] F. Schreiber. Structure and growth of self-assemblying monolayers. *Prog. Surf. Sci.*, 65:151–256, 2000. [cited at p. 29]

[80] S. De Feyter and F.C. De Schryver. Two-dimensional supramolecular self-assembly probed by scanning tunneling microscopy. *Chem. Soc. Rev.*, 32:139–150, 2003. [cited at p. 29]

[81] F. Rosei, M. Schunack, Y. Naitoh, P. Jiang, A. Gourdon, E. Laegsgaard, I. Stensgaard, C. Joachim, and F. Besenbacher. Properties of large organic molecules on metal surfaces. *Prog. Surf. Sci.*, 71:95, 2003. [cited at p. 29]

[82] Sanders K M *et al. J. Am. Chem. Soc.*, 112:5525–5534, 1990. [cited at p. 29, 37, 47]

[83] L. Nony, R. Bennewitz, O. Pfeiffer, E. Gnecco, A. Baratoff, E. Meyer, T. Eguchi, A. Gourdon, and C. Joachim. Cu-TBPP and PTCDA molecules on insulating surfaces studied by ultra-high-vacuum non-contact AFM. *Nanotechnology*, 15:91–96, 2004. [cited at p. 29, 32]

[84] S.A. Burke, J.M. Mativetsky, R. Hoffmann, and P. Grütter. Nucleation and submonolayer growth of C_{60} on KBr. *Phys. Rev. Lett.*, 94(9):096102 – 1, 2005. [cited at p. 29]

[85] T. Kunstmann, A. Schlarb, M. Fendrich, T. Wagner, R. Moller, and R. Hoffmann. Dynamic force microscopy study of 3,4,9,10-perylenetetracarboxylic dianhydride on KBr(001). *Phys. Rev. B*, 71(12):121403 – 1, 2005. [cited at p. 29, 56]

[86] J. M. Mativetsky, S. A. Burke, S. Foster, and P. Grütter. Templated growth of 3,4,9,10-perylenetetracarboxylic dianhydride molecules on a nanostructured insulator. *Nanotechnology*, 18:105303, 2007. [cited at p. 29, 32]

[87] J. M. Mativetsky, S. A. Burke, S. Foster, and P. Grütter. Nanoscale pits as templates for building a molecular device. *Small*, 3:818–821, 2007. [cited at p. 29, 32]

[88] T.A. Jung, R.R. Schlittler, J.K. Gimzewski, H. Tamg, and C. Joachim. Controlled room-temperature positioning of individual molecules: Molecular flexure and motion. *Science*, 271:181, 1996. [cited at p. 29]

[89] J. Weckesser, A. De Vita, J.V. Barth, C. Cai, and K. Kern. Mesoscopic correlation of supramolecular chirality in one-dimensional hydrogen-bonded assemjlies. *Phys. Rev. Lett.*, 87(9):096103, 2201. [cited at p. 29]

[90] M. Eremtchenko, J.A. Schaefer, and F.S. Tautz. Understanding and tuning the epitaxy of large aromatic adsorbates by molecular design. *Nature*, 425:602–605, 2003. [cited at p. 29]

[91] L. R. Milgrom. The colours of life: an introduction to the chemistry of porphyrins and related compounds. *Oxford University Press*, 1997. [cited at p. 30]

[92] D. Bonifazi. *From solution to surfaces: synthesis, physical properties, and materials applications of novel fullerene and porphyrin derivatives.* PhD thesis, ETH Zürich, 2004. [cited at p. 30]

[93] M. F. Perutz. Hemoglobin structure and respiratory transport. *Scientific American*, 6:92–125, 1978. [cited at p. 30]

[94] R. B. Woodward, W. A. Ayer, J. M. Beaton, F. Bickelhaupt, R. Bonnett, P. Buchschacher, G. L. Closs, H. Dutler, J. Hannah, F. P. Hauck, S. Itô, A. Langemann, E. Le Goff, W. Leimgruber, W. Lwowski, J. Sauer, Z. Valenta, and H. Volz. The total synthesis of chlorophyll. *J. Am. Chem. Soc.*, 82:3800–3802, 1960. [cited at p. 30]

[95] F. Cheng, S. Zhang, A. Adronov, L. Echegoyen, and F. Diederich. Triply fused Zn-II–porphyrin oligomers: Synthesis, properties, and supramolecular interactions with single-walled carbon nanotubes (SWNTs). *Chem. Eur. J.*, 12:6062–6070, 2006. [cited at p. 30]

[96] C. Barth and C. Henry. Kelvin probe force microscopy on surfaces of UHV cleaved ionic crystals. *Nanotechnology*, 7:S155, 2006. [cited at p. 30]

[97] J.J. Kolodziej, B. Such, P. Czuba, F. Krok, P. Piatkowski, P. Struski, M. Szymonski, R. Bennewitz, S. Schär, and E. Meyer. Frenkel defect interactions at surfaces of irradiated alkali halides studied by non-contact atomic force microscopy. *Surface Science*, 482-485:902–909, 2001. [cited at p. 31]

[98] Spartan '06,, 2006. Wavefunction Inc., Irvine, CA (USA). [cited at p. 36]

[99] http://www.povray.org. [cited at p. 38, 57]

[100] E. A. Meyer, R. K. Castellano, and F. Diederich. *Angew. Chem., Int. Ed. Engl.*, 42:1210– 1250, 2003. [cited at p. 37]

[101] T. S. Balaban *et al.* Structural characterization of artificial self-assembling porphyrins that mimic the natural chlorosomal bacteriochlorophylls c,d and e. *Chem. Eur. J*, 11:2267–2275, 2005. [cited at p. 40, 44, 47]

[102] K. Yamamoto, T. Iijima, T. Kunishi, K. Fuwa, and T. Osaka. The growth forms of small Au particles grown on KBr and NaCl substrates having monatomic steps. *Journal of Crystal Growth*, 94(3):629, 1989. [cited at p. 43, 51]

[103] J. Pšenèík, J. B. Arellano, T. P. Ikonen, C. M. Borrego, P. A. Laurinmäki, S. J. Butcher, R. E. Serimaa, and R. Tuma. Internal structure of chlorosomes from brown-colored chlorobium species and the role of carotenoids in their assembly. *Biophys. J.*, 91:1433–1440, 2006. [cited at p. 44]

[104] C. Barth and C.R. Henry. High resolution imaging of gold clusters on KBr(100) surfaces investigated by dynamic force microscopy. *Nanotechnology*, 15:1264, 2004. [cited at p. 50, 52]

[105] H. Bethge. Electron microscopic studies of surface structures and some relations to surface phenomena. *Surface Science*, 3:33, 1964. [cited at p. 51]

[106] O. H. Pakarinen, C. Barth, A. S. Foster, R. M. Nieminen, and C. R. Henry. High-resolution scanning force microscopy of gold nanoclusters on the KBr (001) surface. *Phys. Rev. B*, 73:235428, 2006. [cited at p. 51]

[107] M. Goryl, F. Buatier de Mongeot, F. Krok, A. Vevecka-Priftaj, and M. Szymonski. Leaky atomic traps: Upwards diffusion of au from nanoscale pits on ionic-crystal surfaces. *Phys. Rev. B*, 76:75423, 2007. [cited at p. 51, 74]

[108] J. Repp, G. Meyer, S. M. Stojkovic, A. Gourdon, and Ch. Joachim. Scanning tunneling microscopy imaging of individual molecular orbitals. *Phys. Rev. Lett.*, 94:026803, 2005. [cited at p. 56]

[109] Ch. Loppacher, U. Zerweck, L.M. Eng, S. Gemming, G. Seifert, C. Olbrich, K. Morawetz, and M. Schreiber. Adsorption of 3,4,9,10-perylene-tetracarboxylic-dianhydride on ultrathin potassium bromide films. *Nanotechnology*, pages 1586–1573, 2006. [cited at p. 56]

[110] R. Bennewitz, V. Barwich, M. Bammerlin, M. Guggisberg, C. Loppacher, A. Baratoff, E. Meyer, and H.-J. Güntherodt. Ultrathin films of NaCl on Cu(111): a LEED and dynamic force microscopy study. *Surface Science*, 438:289, 1999. [cited at p. 56, 57]

[111] Ch. Loppacher, M. Bammerlin, M. Guggisberg, F. Battiston, R. Bennewitz, S. Rast, A. Baratoff, E. Meyer, and H.-J. Güntherodt. Phase variation experiments in non-contact dynamic force microscopy using phase locked loop techniques. *Appl. Surf. Sci.*, 140:287–292, 1999. [cited at p. 56, 57, 59]

[112] R. Bennewitz, A.S. Foster, L.N. Kantorovich, M. Bammerlin, Ch. Loppacher, S. Schär, M. Guggisberg, E. Meyer, H.-J. Güntherodt, and A.L. Shluger. Atomically resolved steps and kinks on NaCl islands on Cu(111): Experiment and theory. *Phys. Rev. B*, 62:2074, 2000. [cited at p. 56, 57, 59]

[113] L. Ramoino, M. von Arx, S. Schintke, A. Baratoff, H.-J. Güntherodt, and T.A. Jung. Layer-selective epitaxial self-assembly of porphyrins on ultrathin insulators. *Chem. Phys. Lett.*, 417:22–27, 2005. [cited at p. 56]

[114] L. Ramoino. *Adsorption and Self-Organization of CuOEP on Heterogenous Surfaces: Tuning the Molecule-Substrate Interaction.* PhD thesis, University of Basel, 2005. [cited at p. 56, 59]

[115] J. G. Roberts, S. Hoffer, M. A. Van Hove, and G. A. Somorjai. Tensor low-energy electron diffraction analysis of the surface structure of NaCl(100) thin films grown on Pd(100) and Pt(111). *Surface Science*, 437:75, 1999. [cited at p. 56]

[116] G. M. Rothberg, M. Eisenstadt, and P. Kusch. Free evaporation of alkali halide crystals. *J. Chem. Phys.*, 30:517, 1959. [cited at p. 56]

[117] U. Barjenbruch, S. Fölsch, and M. Henzler. Surface states on epitaxial thin films of NaCl and KCl. *Surface Science*, 749:211–212, 1989. [cited at p. 57]

[118] K. Gloeckler, M. Sokolowski, A. Soukopp, and E. Umbach. Initial growth of insulating overlayers of NaCl on Ge(100) observed by scanning tunneling microscopy with atomic resolution. *Phys. Rev. B*, 54:7705, 1996. [cited at p. 57, 59]

[119] W. Hebenstreit, J. Redinger, Z. Horozova, M. Schmid, R. Podloucky, and P. Varga. Atomic resolution by STM on ultra-thin films of alkali halides: experiment and local density calculations. *Surface Science*, 424:L321, 1999. [cited at p. 57, 59]

[120] J. Repp. *Rastertunnelmikroskopie und -spektroskopie an Adsorbaten auf Metall- und Isolatoroberflächen.* PhD thesis, Freie Universität Berlin, 2002. [cited at p. 57, 59]

[121] J. Repp, G. Meyer, and K.-H. Rieder. Snell's law for surface electrons: Refraction of an electron gas imaged in real space. *Phys. Rev. Lett.*, 92(3):036803, 2004. [cited at p. 57]

[122] S. Fölsch, U. Barjenbruch, and M. Henzler. Atomically thin epitaxial films of NaCl on germanium. *Thin Solid Films*, 172:123, 1989. [cited at p. 57]

[123] C. Schwennicke, J. Schimmelpfennig, and H. Pfnür. *Surface Science*, 293:57, 1993. [cited at p. 57]

[124] W. Hebenstreit, M. Schmidt, J. Redinger, R. Podloucky, and P. Varga. Bulk terminated NaCl(111) on aluminum: a polar surface of an ionic crystal? *Phys. Rev. Lett.*, 85:5376, 2000. [cited at p. 59]

[125] J.D. Jackson. *Classical Electrodynamics.* J. Wiley and Sons, New York, 2nd edition edition, 1975. [cited at p. 60, 62]

[126] H. Spillmann, A. Kiebele, M. Stöhr, T. A. Jung, D. Bonifazi, F. Cheng, and F. Diederich. A two-dimensional porphyrin-based porous network featuring communicating cavities for the templated complexation of fullerenes. *Advanced Materials*, 18(3):275, 2006. [cited at p. 63]

[127] D. Fujita, H-Y. Sheng, Z.-C. Dong, and H. Nejoh. Nanostructure fabrication with a point contact formation between a gold tip and a Si(111)-(7x7) surface with an ultrahigh vacuum scanning tunneling microscope. *Appl. Phys. A*, 66:S753, 2004. [cited at p. 74]

[128] Th. Glatzel, S. Sadewasser, and M. Ch. Lux-Steiner. Amplitude or frequency modulation-detection in Kelvin probe force microscopy. *Appl. Phys. Lett.*, 210:84–89, 2003. [cited at p. 75]

[129] U. Zerweck, Ch. Loppacher, T. Otto, S. Grafström, and L.M. Eng. Accuracy and resolution limits of Kelvin probe force microscopy. *Phys. Rev. B*, 71:125424, 2005. [cited at p. 75]

[130] Th. Glatzel and Ph. Carl. Private conversation. [cited at p. 84]

[131] I.D. Mayergoyz. Solution of the nonlinear equation of semiconductoer device theory. *J. Appl. Phys.*, 59:195, 1986. [cited at p. 84, 85]

[132] W. W. Keller. Fast algorithm for iteratively solving the nonlinear static poisson equation in semiconductors. *J. Appl. Phys.*, 61:5189, 1987. [cited at p. 84, 85]

[133] G. J. L. Ouwerling. Further improved algorithm for the solution of the nonlinear poisson equation in semiconductor devices. *J. Appl. Phys.*, 66:6144, 1989. [cited at p. 84, 85]

[134] S. Belaidi, F. Lebon, P. Girard, G. Leveque, and S. Pagano. Finite element simulations of the resolution in electrostatic force microscopy. *Appl. Phys. A*, 66:S239, 1998. [cited at p. 84]

[135] S. Sadewasser, Ph. Carl, Th. Glatzel, and M. Ch. Lux-Steiner. Influence of uncompensated electrostatic force on height measurements in non-contact atomic force microscopy. *Nanotechnology*, 15:s14, 2004. [cited at p. 84]

[136] H. M. Lieberstein. Mathematical research center report. 1959. [cited at p. 85]

Publications

Papers

1. O. Pfeiffer, E. Gnecco, **L. Zimmerli**, S. Maier, E. Meyer, L. Nony, R. Bennewitz, F. Diederich, H. Fang, and D. Bonifazi, 'Force microscopy on insulators: imaging of organic molecules', J. Phys. Conf. Ser. 19 (2005) 166

2. **L. Zimmerli**, S. Maier, Th. Glatzel, E. Gnecco, O. Pfeiffer,F. Diederich, L. Fendt and E. Meyer,'Formation of molecular wires on nanostructured KBr' J. Phys.: Conf. Ser. 61 (2007) 1357-1360

3. S. Maier, L. Fendt, Th. Glatzel, O. Pfeiffer, **L. Zimmerli**, F. Diederich and E. Meyer, 'Engineering molecular porphyrin wires at insulating surfaces', in preparation

Oral Presentations

1. L. Zimmerli, L. Nony, E. Gnecco, A. Baratoff, A. Alkauskas, R. Bennewitz, O. Pfeiffer, S. Maier, A. Wetzel, E. Meyer and C. Gerber: *Trapping and self-assembly of polar molecules in nanometer-sized pits on an insulator.* Seventh International Conference on Non-contact Atomic Force Microscopy
   12-15 September 2004, Seattle, USA

2. L. Zimmerli, L. Nony, E. Gnecco, A. Baratoff, A. Alkauskas, R. Bennewitz, O. Pfeiffer, S. Maier, A. Wetzel, E. Meyer and C. Gerber: *Trapping and self-assembly of polar molecules in nanometer-*

sized pits on an insulator. BioNano Workshop, January 2005, Lenzerheide

3. L. Zimmerli, L. Nony, E. Gnecco, A. Baratoff, A. Alkauskas, R. Bennewitz, O. Pfeiffer, S. Maier, A. Wetzel, E. Meyer and C. Gerber *Ordered molecular assemblies confined on a nanostructured insulator: an atomic force microscopy investigation.* 13.12.2004, Kolloquium, Basel, Switzerland

4. L. Zimmerli, O. Pfeiffer, S. Maier, L. Fendt, Th Glatzel, F. Diederich and E. Meyer: *NC- AFM of molecules on insulators.* NCCR Meeting, April 2006, Basel, Switzerland

5. L. Zimmerli, O. Pfeiffer, S. Maier, L. Fendt, Th Glatzel, F. Diederich and E. Meyer: *Formation of Molecular Wires on nanostructured KBr.* 9th International Conference on Non-Contact Atomic Force Microscopy, Juli 16- 20 2006, Kobe, Japan

6. L. Zimmerli, O. Pfeiffer, S. Maier, L. Fendt, Th Glatzel, F. Diederich and E. Meyer: *Formation of Molecular Wires on nanostructured KBr.* International Conference on Nanoscience and Technology, Juli 30- August 4 2006, Basel, Switzerland

Poster Presentations

1. L. Zimmerli, O. Pfeiffer, R. Bennewitz, A. Baratoff and E. Meyer
   Conservative and dissipative forces close to organic molecules.
   8th International Conference on Non-Contact Atomic Force Microscopy
   15. to 18. August 2005, Bad Essen, Germany.

2. L. Zimmerli, O. Pfeiffer, R. Bennewitz, A. Baratoff and E. Meyer
   Conservative and dissipative forces close to organic molecules.
   DPG Conference
   March 26 - 31 2006, Dresden, Germany.

3. L. Zimmerli, S. Maier, O. Pfeiffer, Th. Glatzel, L.-A. Fendt , F. Diederich and E. Meyer
   Formation of molecular wires on nanostrucutured insulators.
   NCCR Meeting, March 2007, Basel, Switzerland.

Acknowledgements

My PhD has been a challenging, interesting and entertaining time. And therefore i'd like to thank all the people who helped me in any way to accomplish this work.

First of all, I am grateful to Prof. Dr. E. Meyer for giving me the opportunity to do my PhD work in his group. I also want to thank him and Prof. Dr. H.-J. Güntherodt for accepting to referee this work.

Special thanks belong to Dr. Thilo Glatzel who was more than a PhD supervisor to me. To a great extent his scientifical motivation and his social competence kept the Nanolino and also my thesis running. It was a great pleasure to work with him in the lab. I wish him all the best in his scientific career and i really look forward to continue working with him.

I'd like to thank R. Huber and Dr. A. Kiebele for keeping company with me during countless lunchbreaks with interesting scientific and non-scientific discussions. Additionally i am grateful to Dr. T. Gyalog and Dr. M. Guggisberg for letting me contribute several times on their projects. I will miss the gravitation experiments on the 'Silver Star'.

It was always a great pleasure to work in the friendly and familiar atmosphere created by the present and past members of the group. My thanks go to: Dr. O. Pfeiffer, Dr. S. Maier, Dr. E. Gnecco, Dr. L. Nony, Prof. Dr. A. Baratoff, Dr. B. Such, Dr. A. Socoliuc, Dr. A. Wetzel, Dr. M. Schönenberger, A. Rao, J. Gessler and Ch. Held.

Working with high-tech material needs people to develop and improve it. Therefore my thanks also go to the member of the electronical and mechanical workshop. S. Martin, H. Breitenstein, S. Jakob, Dr. h.c. H.-R. Hidber, A. Tonin, R. Maffiolini, M. Steinacher, W. Erni and particularly S. Messmer deserve special mention.

I'd like to thank G. Weaver, A. Kalt and B. Kammermann for the great work they do in mastering all the administrative bureaucracy for us.

Finally, I want to thank my family. Their continuous support and love during this thesis was really appreciated. I also want to thank my girlfriend Annicka. During the last year she was my biggest support, giving me a great family life, played guilty conscience when i wasn't that motivated and made sure that i was able to fully concentrate on my work.

Curriculum Vitae

von Lars A. Zimmerli, geboren am 15.12.1977

Ausbildung

seit 12.2003	Doktorand am Institut für Physik, **Universität Basel**
10.1998 - 6.2003	Studium der Physik an der **Universität Basel** Abschluss: Diplom in Experimentalphysik
8.1994 - 12.1997	**Gymnasium Liestal, BL**, Matura Typus C (Naturwissenschaften)

Berufserfahrung

9.2006 - 12.2006	**Bank Coop AG,** Erstellung einer Datenbankanwendung zur Auswertung des bankeigenen Werschtrifteninventars.
4.2004 - 6.2005	**Physica pro Medicis,** fachliche und technische Mithilfe bei der Entwicklung eines Webbasierten Physikpraktikums für Medizinstudenten.
7.1999 - 9.2006	**Valora AG,** Entwicklung diverser Datenbankapplikationen zur optimierung der Logistikprozesse.

Folgenden Dozentinnen und Dozenten verdanke ich meine Ausbildung:
C. Bandle, R. Bennewitz, C. Bruder, H. Burkhart, A. Bussmann-Holder, H.-J. Hug, D. Masser, E. Meyer, H.-J. Güntherodt, M. Hegner, G.-R. Plattner, I. Sick, C.Schönenberger, L. Tauscher, F.-K. Thielemann, D. Trautmann